



Delft University of Technology

From Radar to Reality. Associating persistent scatterers to corresponding objects

Yang, M.

DOI

[10.4233/uuid:1e3cedbf-acf7-412f-9927-25ad5f5f1de3](https://doi.org/10.4233/uuid:1e3cedbf-acf7-412f-9927-25ad5f5f1de3)

Publication date

2020

Document Version

Final published version

Citation (APA)

Yang, M. (2020). *From Radar to Reality. Associating persistent scatterers to corresponding objects*. [Dissertation (TU Delft), Delft University of Technology]. <https://doi.org/10.4233/uuid:1e3cedbf-acf7-412f-9927-25ad5f5f1de3>

Important note

To cite this publication, please use the final published version (if applicable). Please check the document version above.

Copyright

Other than for strictly personal use, it is not permitted to download, forward or distribute the text or part of it, without the consent of the author(s) and/or copyright holder(s), unless the work is under an open content license such as Creative Commons.

Takedown policy

Please contact us and provide details if you believe this document breaches copyrights. We will remove access to the work immediately and investigate your claim.

From Radar to Reality Associating Persistent Scatterers to Corresponding Objects

Mengshi Yang



From Radar to Reality

Associating persistent scatterers to corresponding objects

Mengshi YANG

From Radar to Reality

Associating persistent scatterers to corresponding objects

Proefschrift

ter verkrijging van de graad van doctor
aan de Technische Universiteit Delft,
op gezag van de Rector Magnificus prof. dr. ir. T.H.J.J. van der Hagen,
voorzitter van het College voor Promoties,
in het openbaar te verdedigen op woensdag 2 september 2020 om 12:30 uur

door

Mengshi YANG

Bachelor of Science in Geomatics Engineering, Central South University
geboren te Xishuangbanna, Yunnan, China.

Dit proefschrift is goedgekeurd door de promotoren.

Samenstelling promotiecommissie:

Rector Magnificus,	voorzitter
Prof. dr. ir. R.F. Hanssen	Technische Universiteit Delft, promotor
Prof. dr. M. Liao	Wuhan University, promotor
Dr. E.J. López-Dekker	Technische Universiteit Delft, copromotor

Onafhankelijke leden:

Prof. dr. J.J. Mallorquí	Universitat Politècnica de Catalunya, Spain
Prof. dr. C. Barbier	Université de Liège, Belgium
Prof. dr.-Ing. Habil. R. Klees	Technische Universiteit Delft
Prof. ir. P. Hoogeboom	Technische Universiteit Delft



Mengshi YANG

Department of Geoscience and Remote Sensing, Delft University of Technology
State Key Laboratory of information Engineering in Surveying, Mapping and Remote Sensing, Wuhan University

Keywords: satellite radar interferometry, persistent scatterers, time series InSAR technique, sub-pixel correction, precise point positioning, corner reflectors, digital surface model, ray-tracing, multiple scattering

ISBN 978-94-6384-128-3

Copyright © 2020 by Mengshi YANG

All rights reserved. No part of the material protected by this copyright notice may be reproduced or utilized in any form or by any means, electronic or mechanical, including photocopying, recording or by any information storage and retrieval system, without the prior permission of the author.

Type set by the author with the L^AT_EX Documentation System
Printed by Ridderprint, The Netherlands

An electronic version of this dissertation is available at
<http://repository.tudelft.nl/>.

Contents

Summary	ix
Samenvatting	xi
Summary in Chinese	xiii
Nomenclature	xv
1 Introduction	1
1.1 Motivation	1
1.2 Background	1
1.3 Problem statement	4
1.4 Research objectives	7
1.5 Outline and research methodology	7
2 Time-series InSAR and InSAR scatterers	11
2.1 Synthetic aperture radar image	11
2.1.1 Amplitude	12
2.1.2 Phase	13
2.2 SAR interferometry	14
2.2.1 Observable.	15
2.2.2 Processing procedure	18
2.2.3 Limitations.	20
2.3 SAR interferometric time series analysis	20
2.3.1 Baseline configuration	21
2.3.2 Coherent scatterers	23
2.3.3 Mathematical models	26
2.3.4 Processing procedure	27
2.3.5 Potential improvements	27
2.4 Summary	29
3 Sub-pixel persistent scatterer interferometry	31
3.1 Introduction	31
3.2 Sub-pixel phase and its influence on PSI results.	32
3.2.1 Sub-pixel position phase.	32
3.2.2 Influence on geolocation accuracy.	35
3.2.3 Influence on displacement estimation	38
3.3 Methodology	39
3.3.1 Dominant scatterer localization	40
3.3.2 Sub-pixel correction processing chain	40

3.4	Experiment setting	41
3.5	Displacements Estimation	42
3.6	Geolocation precision.	47
3.7	Necessity	49
3.8	Conclusions.	50
4	Precise point positioning aided by corner reflectors and surface models	51
4.1	Introduction	51
4.2	Point scatterer geolocation	53
4.2.1	Positioning error sources.	55
4.2.2	Positioning quality.	57
4.3	GCP-assisted InSAR precise point positioning	57
4.3.1	Single-epoch CR	58
4.3.2	Multi-epoch CR	60
4.4	DSM-assisted InSAR precise point positioning	62
4.5	Experiment setup	64
4.5.1	SAR data	64
4.5.2	Artificial reflectors	64
4.5.3	DSM data	67
4.6	Results	67
4.6.1	TerraSAR-X results	68
4.6.2	Sentinel-1 results	72
4.6.3	DSM product evaluation.	76
4.7	Comparison of correction methods	77
4.8	Conclusions.	78
5	Understanding persistent scatterers with ray-tracing	81
5.1	Introduction	81
5.2	The RaySAR simulator	83
5.2.1	Point scatterer simulation with RaySAR	85
5.2.2	Definition of a 3D scene for RaySAR	86
5.3	Influence of Level-of-Detail models on simulation	88
5.3.1	The definition of LOD	89
5.3.2	Simulation with varying LOD models	89
5.4	Linking persistent scatterers to an urban model	93
5.4.1	Methodology.	93
5.4.2	Simulation assessment.	94
5.4.3	Work-flow	95
5.5	Experiments	96
5.5.1	Test site and data.	96
5.5.2	PSI results	97
5.6	Linking results: TerraSAR-X	98
5.6.1	Simulated point scatterer	98
5.6.2	Linking of PS and SPS	100
5.6.3	Target matching validation.	103

5.7 Displacement signal for multiple bounce signals	105
5.7.1 Setting up of a simulated displacement event	107
5.7.2 Simulated displacements interpretation	107
5.8 Conclusions.	110
6 Conclusions and recommendations	111
6.1 Conclusions.	111
6.2 Main contributions	115
6.3 Recommendations	118
Appendix A	119
Bibliography	121
Acknowledgement	135
About the Author	139

Summary

Multi-epoch Synthetic Aperture Radar Interferometry (InSAR) is widely used to estimate displacements of selected scatterers from phase observations. However, their interpretation needs a connection to objects in the real world. To associate InSAR scatterers to their corresponding geo-objects, it is necessary to (i) accurately estimate the phase center of radar scatterers in radar coordinates, (ii) precisely position the scatterers in 3D geographic coordinates, and (iii) satisfy the constraint that these positions need to be physically realistic. This study addresses these three requirements.

The effective phase center of a scatterer is not situated at the nominal position of the pixel. As a result, scatterers are evaluated at the wrong position and the reference phase calculated at that location will be biased. We evaluate the influence of this sub-pixel position on the geolocation of the scatterer and its deformation quality for various satellite platforms. A method to locate the phase center of the dominant scatterer is developed and is applied to a stack of TerraSAR-X, Radarsat-2, and Sentinel-1 images. The sub-pixel correction shows to be significant for improving the geolocation, up to a few meters—especially for planar (horizontal) precision. It is only of limited influence for the displacement estimation and more relevant in the case of large orbital baselines.

Even after sub-pixel correction, the position of scatterers in an earth-centered, earth-fixed geodetic datum is often in order of a few meters, which is not always sufficient to physically link the scatterer to a geo-object. We evaluate four approaches for correcting this positioning bias, i.e., (i) an advanced geophysical correction, (ii) the single-epoch deployment of a corner reflector (CR), (iii) a multi-epoch deployment of a CR, and (iv) a correction using a high-precision digital surface model (DSM). The positioning performance of these approaches is analyzed from the aspects of practicability, reliability, and precision with TerraSAR-X and Sentinel-1 data. We show that while the multi-epoch CR approach achieves the best positioning results, the DSM-assisted correction is able to obtain comparable results if a high precision DSM is available, better than DTED-4.

The position of the estimated geometric phase center may differ from the position of the physical phase center. We use ray-tracing to predict the position of point scatterers using generic 3D models, and match them with the detected point scatterers from a stack of TerraSAR-X images. We find that the majority of detected scatterers appears to be positioned at their correct physical location. Moreover, many point scatterers correspond to multiple scattering mechanisms—more than half of the identified scatterers correspond to double- or triple-bounce scatterers. The mismatch between the geometrically estimated position and the signal source occurs mainly for multiple scattering; fourfold and more. This shows that the bounce levels of the scatterers are a relevant attribute to understand and interpret the displacements of persistent scatterers.

In general, we conclude that sub-pixel correction and positioning bias correction should be included in default InSAR data processing, and that the majority of detected scatterers are positioned at physically realistic locations.

Samenvatting

Tijdseries van interferometrische SAR beelden worden gebruikt om de verplaatsing te schatten van toevallige radar reflectoren. Echter, om dit goed te kunnen duiden, dienen deze reflectoren gekoppeld te worden aan objecten op het aardoppervlak. Om deze koppeling te realiseren, is het noodzakelijk om (i) de ligging van het fasecentrum van de reflectoren in het radarbeeld binnen het pixel te schatten, (ii) de precieze 3D positie van alle reflectoren in een geodetisch referentiesysteem te vinden, en (iii) te zorgen dat de geschatte posities ook fysisch realistisch zijn. Deze drie voorwaarden worden in deze studie onderzocht.

Het effectieve fasecentrum van een reflector bevindt zich niet op de nominale (hoek-) positie van een pixel. Hierdoor worden deze reflectoren geëvalueerd op een verkeerde positie, waardoor de referentiefase ook wordt berekend op een verkeerde positie. De invloed van deze fout op de geolokalisering van de reflector en op de kwaliteit van de geschatte verplaatsings is onderzocht voor verschillende satellietssystemen. Een methode is ontwikkeld om het fasecentrum van de dominante reflectie binnen een resolutiecel te lokaliseren, een deze is vervolgens toegepast op TerraSAR-X, Radarsat-2, en Sentinel-1 beelden. Deze sub-pixel correctie blijkt significant te zijn voor de geolocalisering, met een verbetering van enkele meters, voornamelijk in het horizontale vlak. Voor de schatting van deformaties (verplaatsingen) is de correctie maar van beperkte invloed. In het algemeen is de correctie meer relevant voor satellietbanen die verder uit elkaar liggen.

Zelfs wanneer de sub-pixel correctie wordt toegepast, dan is de 3D positie van de toevallige reflectoren nog steeds in de orde van een aantal meters, hetgeen vaak onvoldoende is om de reflector te koppelen aan een fysiek object. We analyseren vier mogelijkheden om deze positiebias op te lossen: een geavanceerde geofysische correctie, het installeren van een hoekreflector voor slechts één acquisitie, het installeren van een hoekreflector gedurende een hele tijdserie, en een correctie die gebruik maakt van een digitaal hoogtemodel. De prestaties van al deze methoden zijn geëvalueerd op praktische uitvoerbaarheid, betrouwbaarheid en precisie, voor zowel TerraSAR-X als Sentinel-1 data. Hieruit blijkt dat terwijl het toepassen van een hoekreflector over een gehele tijdserie het beste resultaat levert, de methode die gebruik maakt van het hoogtemodel vergelijkbare resultaten levert, zolang dit model maar van het niveau DTED-4 of beter is.

De geschatte geometrische positie van het fasecentrum van een natuurlijke reflector hoeft niet gelijk te zijn aan de fysisch-realistische positie van de reflectie. Door gebruik te maken van *ray tracing* hebben we de verwachte fysische positie bepaald, m.b.v. generieke 3D modellen, en deze vergeleken met gedetecteerde reflecties (*persistent scatterers*) van een serie TerraSAR-X beelden. Hieruit blijkt dat de meerderheid van de gevonden reflecties zich bevindt op een correcte (fysisch realistische) positie. Bovendien blijkt dat meer dan de helft van de gevonden reflecties bestaan uit twee- of drievoudige reflecties. Wanneer reflecties bestaan uit meer dan drievoudige reflecties, dan worden deze

meestal niet werkelijk in de data gevonden. Hieruit volgt dat het aantal malen dat een signaal weerkaatst voordat het weer door de satelliet ontvangen wordt een belangrijk attribuut is bij de interpretatie van persistent scatterers.

Uit bovenstaande analyses kan worden geconcludeerd dat de sub-pixel correctie en de 3D positie-bias correctie standaard moet worden inbegrepen in de InSAR dataverwerking, en dat het merendeel van de gedetecteerde reflecties gepositioneerd worden op fysisch realistische locaties.

摘要

时间序列InSAR技术是针对传统InSAR技术中受时空去相干和大气相位屏障影响的问题提出的,通过提取在时间序列上具有稳定散射特性的高相干点,依据不同相位源的时空特性实现分离,获得在观测时间段内,经过地形、轨道以及大气误差改正的形变速率场,被认为是极具潜力的地表观测手段。然而,目前该方法测量结果的应用和解译仍然存在着诸多不足。

由于“InSAR散射点-地面目标-观测场景”之间的一一关联很难确定,限制InSAR结果在实际应用中进一步对观测结果的解译。具体来说引起关联不确定的原因主要有三方面:(1) InSAR散射点与地物目标对应关系不唯一。InSAR散射体其实是由分辨单元内所有散射信号相干叠加的结果,并非特指分辨单元内主导的强散射信号的地物目标。(2) InSAR散射体三维空间位置不准确。点目标是在二维SAR图像内的平面点,从二维图像平面到三维空间的是一个反演求解的过程,其定位精度通常在几米到几十米,相对于其毫米级形变测量精度来说,三维空间定位精度较差。(3) 没有充分考虑InSAR散射体物理散射机制。由于SAR特殊的成像机理以及复杂城市场景下电磁波的多次散射作用,计算的InSAR散射体的几何相位中心位置与实际的信号源目标不对应,因此相干散射体与地物之间的关联还需要考虑其散射机制的影响。本文针对这三个问题研究了如何建立InSAR散射体与地物目标之间的关联。

本文提出了亚像元永久散射体处理方法,建立时间序列InSAR散射体与单个地物目标的联系。传统永久散射体方法中假设InSAR散射体等同于其分辨单元内的主导信号,但是在建立函数模型时却没有考虑在分辨单元内主导信号亚像素相位贡献。本文分析了主导信号在分辨单元内的亚像素位置对时间序列处理结果的影响,提出以提取亚像素级的有效相位中心位置来建立时序处理的函数模型,避免了分辨单元内杂波信号的干扰,保证了InSAR散射体与其主导散射信号对应地物目标的一一对应关系,且能改善高程和点位估计的结果。该方法应用于TerraSAR-X, Radarsat-2, 和Sentinel-1数据集中,详细对比了亚像素级处理方法和常规时序处理在形变和位置估计上的差异。结果显示,亚像元永久散射体处理方法能为InSAR测量散射体与目标物之间建立关联,给出更准确的位置估计以及更可靠的形变计算结果,且有效排除相位噪声的干扰,提取了更多的相干散射点。

相干散射体精确的三维地理坐标是保障InSAR结果的能够有效解译和应用的重要信息。考虑到相干散射体定位过程中误差的来源和特性,本文提出了InSAR相干散射体的三维定位偏差改正模型。偏差改正模型假设在一定范围内,散射体的定位误差在雷达坐标系内的三个方向(距离向、方位向、高程向)上相互独立且表现出系统性或空间相关性的特点,通过改正三个方向的偏差量,获得所有InSAR散射体的精密定位结果。本文给出了两种定位偏差计算方法,即借助于角反射器和高精度数字地形模型的改正方法。在TerraSAR-X和Sentinel-1的实验结果中,与大地测量数据以及激光扫描数据的交叉验证了本文提出的改正方法的有效性。TerraSAR-X改正结果获得了厘米级的三维定位精度, Sentinel-1数据结果获得了大约四米的三维定位精度。相比于逐个计算地球物理因素进行改正方法而言,本文所提出的方法考虑了高程向偏差改正,给出了更精确的定位结果;同时相比于多视角数据融合求解三维

点位的方法而言，不要求多视角的数据集以及观测区域内能从不同视角探测到的匹配目标，更具有广泛适用性。

受电磁波在地物之间多次散射的影响，很难简单地通过散射体的定位来建立InSAR散射体与地物目标之间的关联，需要在精确三维定位的基础上结合散射机制的角度加以确定。因此，要建立InSAR散射体与地物之间的关联，需要从两方面考虑，一方面是几何定位精度，也就是上述两部分的主要研究内容；另一方面则是从SAR成像过程中的物理散射机制的角度来对散射体进行定位。基于城市三维模型，本文利用光线追踪的方法模拟了相干散射体的位置。通过研究发现大多数相干散射体的几何相位中心与其信号目标一致。同时，在实验的城市场景下，超过一半被识别的散射体是多次散射信号。此外，通过实验证明了，点目标散射机制分析也有利于估计的形变信号的解译。比如实验中，高阶多次散射点（大于三次）观测到的形变量与真实形变量的不同，且可能表现与真实形变方向相反。因此，在InSAR结果分析中，相干散射体的散射次数也是很重要的属性。

Nomenclature

List of acronyms

1D	One Dimensional
2D	Two Dimensional
3D	Three Dimensional
AHN	Actual Height Data of the Netherlands
APD	Atmospheric Path Delay
ASAR	Advanced Synthetic Aperture Radar
BRT	Basic Registration Topography
CR	Corner Reflector
CityGML	A prominent standard for the storage and exchange of 3D city models
DC	Doppler Centroid
DEM	Digital Elevation Model
DEOS	Delft Institute for Earth Observation and Space Systems
DePSI	Delft implementation of Persistent Scatterer Interferometry
DFT	Discrete Fourier Transform
DORIS	Delft Object-oriented Radar Interferometric Software
DTED	Digital Terrain Elevation Model
DSM	Digital Surface Model
DS	Distributed Scatterer
ECE	Ensemble Coherence Estimator
ECEF	Earth-Centered, Earth-Fixed reference system
EMCF	Extended Minimum Cost Flow
ENVISAT	Environmental Satellite
FFT	Fast Fourier Transform
FNR	False Negative Rate
FPR	False Positive Rate
GCP	Ground Control Point
GNSS	Global Navigation Satellite System
HRTI	High-Resolution Terrain Information
ICP	Iterative Closest Point method
InSAR	Synthetic Aperture Radar Interferometry
IPTA	Interferometric Point Target Analysis
ITRF	International Terrestrial Reference Frame
IW	Interferometric Wide
LiDAR	Light Detection And Ranging
LOD	Level of Detail
LOS	Line-Of-Sight
LSE	Least Squares Estimation
NAP	Amsterdam Ordnance Datum, ' <i>Normaal Amsterdams Peil</i> ' in Dutch

PDOP	3D Positioning Dilution of Precision
POV-Ray	Persistence of Vision Ray-tracer
POLSAR	Polarimetric SAR
PRF	Pulse Repetition Frequency
PT	Polar Tide Motion
PS	Persistent Scatterer
PSI	Persistent Scatterer Interferometry
PSP	Persistent Scatterer Pairs
Radar	Radio Detection And Ranging
RD	Dutch National Reference System, ' <i>Rijksdriehoeksstelsel</i> ' in Dutch
RCS	Radar Cross Section
RMSE	Root Mean Squared Error
RSR	Ranging Sampling Ratio
RaySAR	Ray-tracing SAR simulator
SAR	Synthetic Aperture Radar
SLC	Single Look Complex
SBAS	Small BAseline Subset
SNR	Signal to Noise Ratio
SP-PSI	PSI with sub-pixel correction
SPS	Simulation point scatterer
SRTM	Shuttle Radar Topography Mission
ST	Spot-light imaging mode
STC	Spatial-Temporal Consistency
STUN	Spatio-Temporal Unwrapping Network
SET	Solid Earth Tide
SCR	Signal to Clutter Ratio
SM	StripMap
SWST	Sampling Window Start Time
StaMPS	Stanford Method for Persistent Scatterers
Sentinel-1	Copernicus Programme satellite constellation conducted by the ESA
VCE	Variance Component Estimation
ToO	Targets-of-Opportunity
TerraSAR-X	German Radar Earth Observation Satellite
TEC	Total Electron Content
TRF	Terrestrial Reference System
TPR	True Positive Rate
TOP10NL	Digital Topographic Base File of the Land Registry, the Netherlands
VC	Variance-Covariance

List of symbols

cm	centimeter
dB	decibel
km	kilometer
m	meter
rad	radians
y	year

a	phase ambiguity; azimuth distance in SAR geometry
a_T	azimuth-distance of Target T
A	design matrix; amplitude
$\arg(\cdot)$	phase angle in $[-\pi \pi)$ of complex Z
α	baseline orientation
$a_{\text{shift},T}$	azimuth shift
$a_{\text{tect},T}$	tectonic plate movement impacts on azimuth measurement
$a_{\text{set},T}$	solid earth tides impacts on azimuth measurement
$a_{\text{ocean},T}$	ocean loading impacts on azimuth measurement
$a_{\text{pole},T}$	pole tide loading impacts on azimuth measurement
$a_{\text{atm},T}$	atmospheric loading impacts on azimuth measurement
b	number of bounces (trace level)
B	baseline [m]
B_{\perp}	perpendicular baseline
B_{\parallel}	Parallel baseline
B_T	temporal baseline
c	cross-range distance (elevation) of target
c_0	speed of light
$d_{\perp\text{LOS}}$	surface displacement in line of sight
D_e	surface deformation in east
D_n	surface deformation in north
D_u	surface deformation in up
D_A	amplitude dispersion index
$D_{\Delta A}$	amplitude difference dispersion
$\Delta\{\cdot\}$	difference function
$\exp\{\cdot\}$	exponential function
$E\{\cdot\}$	expectation
f_{DC}	Doppler centroid frequency
f	boolean indicating a specular reflection [0 or 1]
F_s	specular coefficient
F_r	roughness factors
F_d	diffuse coefficient
F_w	specularly reflected signal weight
H	height
I	intensity
i	number of points
$\text{Im}\{\cdot\}$	imaginary part
j	imaginary unit; number of points
l	line number in image
m	number of images; number of observations
μ	mean value
\mathbf{M}	confusion matrix
$\max\{\cdot\}$	maximum operator
n	number of unknowns
N	number of images
p	pixel number in image

\mathbf{Q}_{yy}	covariance matrix of observations
\mathbf{Q}_{enh}	positioning Variance-Covariance matrices in east, north, and up/height
\mathbf{Q}_{rac}	positioning Variance-Covariance matrices in azimuth, range, and elevation
$\mathbf{S}(\cdot)$	state vectors
$\mathbf{S}(a_T)$	state vectors of the satellite at the zero Doppler time of imaging target T
r	range distance distance between target and sensor
$\text{Re}\{\cdot\}$	real part
r_g	ground range
r_T	range distance of Target T
$t_{r,\text{sysm}}$	internal electronic delay impacts on range measurement
$r_{\text{pd},T}$	atmosphere path delay impacts on range measurement
$r_{\text{tect},T}$	tectonic plate movement impacts on range measurement
$r_{\text{set},T}$	solid earth tides impacts on range measurement
$r_{\text{ocean},T}$	ocean loading impacts on range measurement
$r_{\text{pole},T}$	pole tide impacts on range measurement
$r_{\text{atm},T}$	atmospheric loading impacts on the range measurement
T	target T
$v_{g/t}$	velocity of the satellite
$W\{\cdot\}$	wrapping operator
v	velocity
Z	complex number
$\{\cdot\}^{-1}$	inversion
$\{\cdot\}^T$	transposition
$\hat{\cdot}$	estimated value
γ	coherence; ellipsoid axis lengths
γ_{amb}	Imaging ambiguities correlation
γ_{dc}	Doppler centroid correlation
γ_{temp}	temporal correlation
γ_{base}	geometrical correlation
γ_{vol}	volume correlation
γ_{ther}	system thermal correlation
γ_{pro}	data processing correlation
γ_{ec}	Ensemble coherence or phase noise
γ_{tmp}	Spectral correlation along time between sub-looks
λ	radar wavelength
ψ	SLC phase
ψ_i^m	SLC phase of point i in SLC image m
ϕ^{ms}	interferometric phase between image m and s
$\phi_{i,j}^{ms}$	arc phase between point i and j in interferogram between image m and s
ϕ_i^{ms}	wrapped interferometric phase of point i in interferogram between image m and s
ϕ_{atmo}	atmospheric phase
ϕ_{defo}	deformation phase
ϕ_{noise}	phase noise
ϕ_{orb}	orbital phase
ϕ_{range}	range dependent phase
ϕ_{ref}	reference phase or flat earth phase
ϕ_{scat}	scattering phase
ϕ_{sub}	sub-pixel phase
ϕ_{topo}	topographic phase

$\phi_{i,\xi}$	sub-pixel phase in azimuth
$\phi_{i,\eta}$	sub-pixel phase in range
σ	standard deviation
θ	look angle
θ_{inc}	incidence angle
ξ_i	azimuth shifting of point i within the resolution cell
η_i	ground-range shifting of point i within the resolution cell
ϑ	squint angle

1

Introduction

1.1. Motivation

Multi-epoch InSAR is useful for estimating the displacement of radar scatterers. However, understanding and interpreting the estimated results requires a connection with the corresponding physical objects. In this study, this connection is built by adding attributes to these measured InSAR scatterers.

1.2. Background

By 2050, 68% of the world's population is expected to live in urban areas (Montgomery, 2008). Durability, sustainability, and resilience of the built environment is, therefore, a key condition of the whole society. Yet, buildings, roads and all forms of urban infrastructure are designed with a certain life expectancy, and age over time. Thus, health monitoring of building and civil engineering structures is becoming increasingly important. The detection and monitoring of structural deformation is one of the key indicators of structural health.

Fig. 1.1 shows some recent urban disasters that exhibited displacement signals before they occurred (Ketelaar et al., 2006; Chang and Hanssen, 2014; Wang et al., 2017; Milillo et al., 2019). It is desirable to detect such displacements at an early stage. Systematic monitoring of the displacement of geo-objects enables risk assessment and the detection of precursor signals. This could not only be useful to prevent impending disasters from happening, but it could also be used as a reference for urban construction planning.

With the advent and development of time series InSAR techniques (Ferretti et al., 2001; Berardino et al., 2002; Hooper et al., 2004; Kampes, 2005; Hooper, 2008; Adam et al., 2008; Ferretti et al., 2011; van Leijen, 2014; Crosetto et al., 2016; Samiei-Esfahany et al., 2016), the applications of InSAR for geo-information stepped into a new era. These methods are capable of estimating time series of displacements with millimeter-level precision by analyzing phase signals on selected coherent scatterers in a stack of SAR images. At the same time, the development of new SAR satellites has increased significantly,

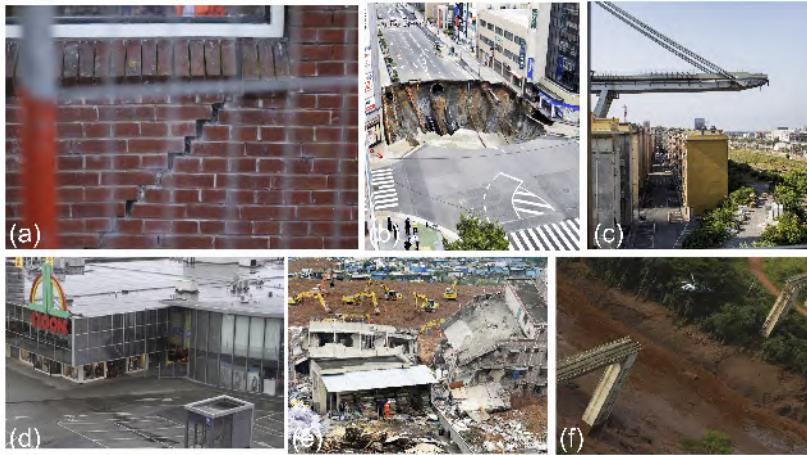


Figure 1.1: Urban disaster examples. (a) Cracks in the wall of a building in Groningen gas field, the Netherlands (Dutch News, 2016). (b) Huge street sinkhole due to the subway extension work in Japan (The Japan Times, 2016). (c) Morandi bridge collapse, Italy, 14 August 2018 (The New York Times, 2018). (d) The near-collapse of a part of a shopping mall in the city of Heerlen, the Netherlands due to upward migration of a cavity. (Chang and Hanssen, 2014). (e) The waster dump led to a disastrous landslide in the city of Shenzhen China 2015 (Wang et al., 2017). (f) Brumadinho dam collapse in south-eastern Brazil 2019 (BBC News, 2019).

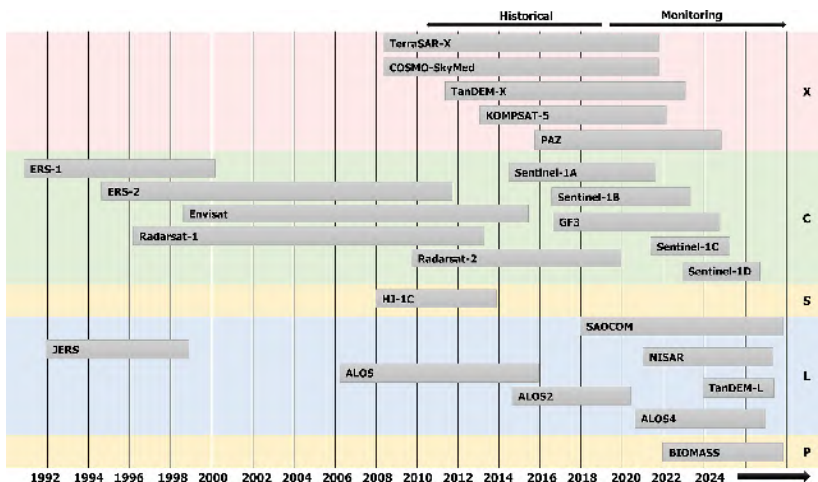


Figure 1.2: SAR Satellite Missions in the past, present, and future, demonstrating an increasing availability of data.

offering sufficient SAR data for time series analysis, see Fig. 1.2. Time series InSAR has become an operational tool for subsidence and infrastructure monitoring in urban areas, and numerous studies have verified its reliability (Fruneau and Sarti, 2000; Mouélic et al., 2002; Ding et al., 2004; Casu et al., 2005; Hanssen, 2005; Ferretti et al., 2007; Liu et al., 2008; Zhang et al., 2009; Jiang et al., 2011a; Chen et al., 2012; Hu et al., 2013; Chaussard et al., 2014; Liao and Wang, 2014; Ma et al., 2015; Crosetto et al., 2016; Qin et al., 2018).

Although this technology is widely used, the potential of time series InSAR has not been fully exploited. Time series InSAR estimates the displacements of selected persistent scatterers (PS). As PS can originate from any object within the built environment, the estimated displacements of PS correspond to different objects and represent different driving mechanisms. Moreover, signals representing different deformation mechanisms are likely to be superimposed.

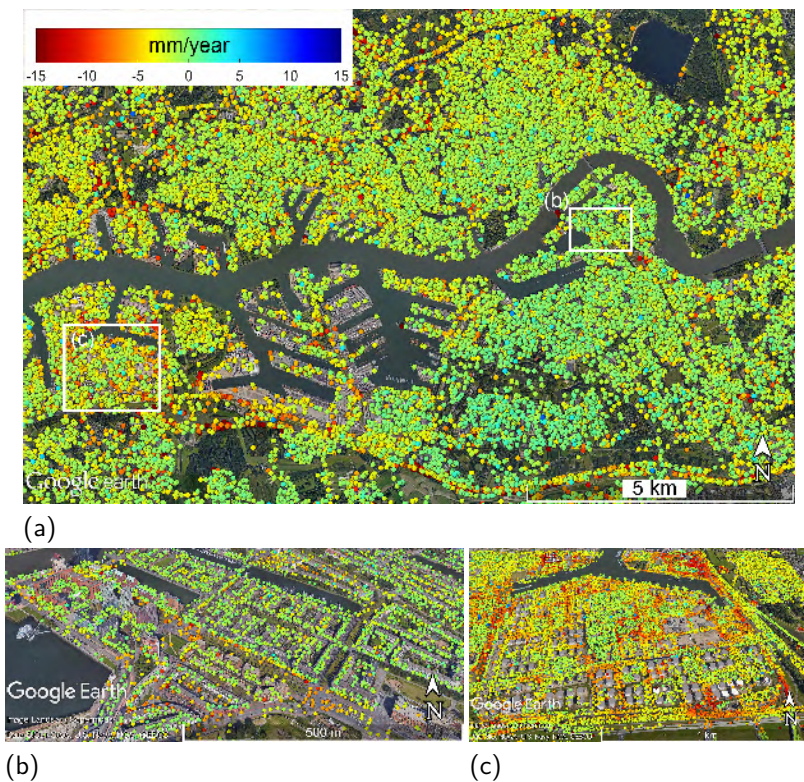


Figure 1.3: (a) Mean displacement velocity map between 2014 and 2017 in the city of Rotterdam, the Netherlands from 49 TerraSAR-X images, a typical result by Time series InSAR technique. The estimated mean deformation rate is color-coded. (b) and (c) Zoom in results in the rectangular boxes indicated in (a).

Fig. 1.3 shows the displacement velocity map over Rotterdam, the Netherlands. 49 TerraSAR-X images between 2014 and 2017 by time series InSAR were processed. Each point, i.e. InSAR scatterer, is chosen from a time-series of SAR acquisitions. These points

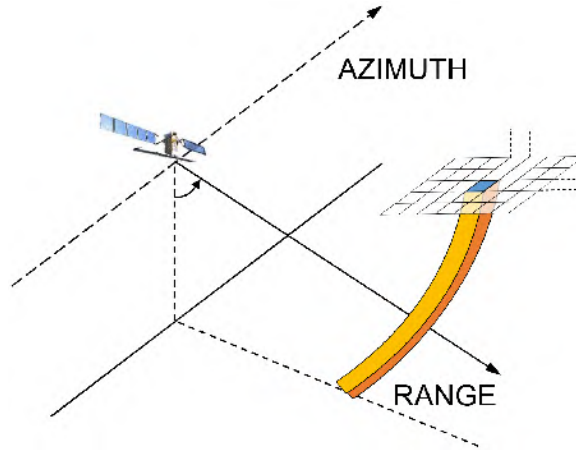


Figure 1.4: Diagram of a resolution cell in 3D space. All the scattering elements within this resolution cell will be coherently summed into one pixel in the SAR image.

provide millimeter-level estimates but they cannot be reliably related to real-world targets in the absence of precise geolocation of each point. Consequently, the evaluation of the deformation phenomenon behind the displacements is limited by the lack of a link to the real-world objects.

The relevance of establishing a one-to-one link between persistent scatterers and specific objects is most explicit when there are different driving mechanisms involved. For example, the observed displacements may be linked to a combination of structural instability and a process of deep layer compaction. While being in close proximity of each other, nearby PS may show completely different deformation signals (Dheenathayalan, 2019). In other cases, different parts of a building or infrastructure may deform differently (Zhu and Shahzad, 2014), which may be a precursor of a partial or full failure of the structure (Sousa and Bastos, 2013; Chang and Hanssen, 2014). In these complex scenarios, an improved linking of InSAR scatterers to physical objects would not only help to identify the local deformation of the object but also facilitate the overall interpretation of the deformation signals.

Establishing a one-to-one link between a PS and a specific object in a complex built environment is the research goal of this study.

1.3. Problem statement

Establishing the desired one-to-one link between a radar scatterer and a specific (part of a) geo-object is currently difficult due to three unresolved problems.

First, in the conventional PSI approach, results are calculated at *per pixel*, rather than *per dominant scatterer* within a resolution cell. As a dominant scatterer is located somewhere within the geometric bounds of a pixel, or resolution cell, this sub-pixel position needs to be accounted for, as it may affect both the position as well as the displacement estimates of the measurement point. Fig. 1.4 sketches a resolution cell in 3D space.

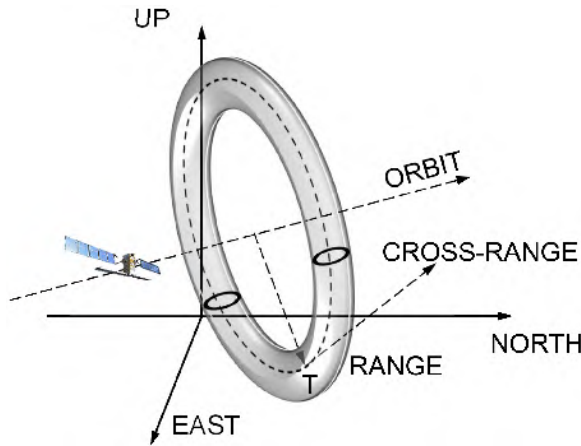


Figure 1.5: A point target T with range R in the zero-Doppler plane orthogonal to the velocity state of the satellite, forming a positioning tube around the satellite.

All the scattering elements within the resolution tube contribute to one pixel. Typically, a strong reflecting object whose signal dominates the pixel and stays coherent over the entire time-span is selected for time series processing. As the dominant scatterer will not be exactly located at the nominal position of the pixel, the position calculation will induce a bias in phase.

Therefore, we need to assess the influence of the sub-pixel position on the PSI estimates. Subsequently, we develop a method to locate the extract phase center of the dominant scattering object within the resolution tube and to mitigate the influences of residual scattering elements. The PSI results can then be improved with this sub-pixel correction.

Second, it is not only the sub-pixel position—within the SAR image—that affects the PSI estimates, but also the *'absolute' location* of the entire image in the three-dimensional world. The positioning precision and accuracy of PS in an earth-centered, earth-fixed geodetic frame is currently in the range of meters, particularly in the cross-range direction (Gernhardt et al., 2015; Dheenathayalan et al., 2016). Fig. 1.5 illustrates a target T and its positioning uncertainty torus.

The target T is located on a circle with a radius (range) R centered at the satellite. The measurements in range and azimuth are affected by additional time-variable positioning components that can range from centimeters to several meters. The torus describes the bias due to system-introduced delays or geophysical path delays. Precise point positioning is determining the optimal position in the torus by correcting the positioning bias as much as possible.

While several studies have focused on estimating the absolute position in an ECEF frame by performing geophysical and system corrections, see Gisinger et al. (2015); Dheenathayalan et al. (2016); Montazeri et al. (2018), it is less well documented how physical ground control points—such as corner reflectors and transponders—or existing elevation models can be used to correct for positioning biases. This is relevant, as it is a practical con-

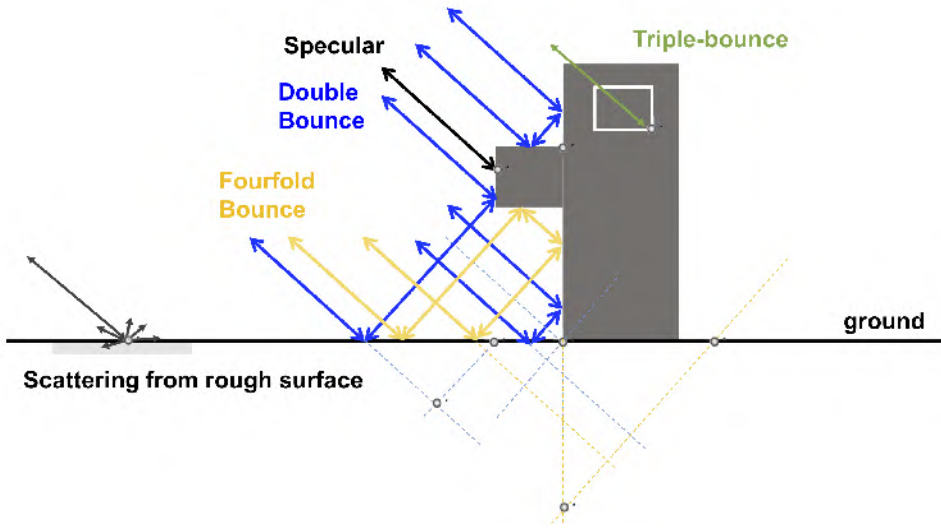


Figure 1.6: Backscatter signals from buildings and ground in an urban scenario.

sideration in many studies to decide whether it is worthwhile to install physical instrumentation in the area of interest or not.

Third, given precise geolocation, the position of point scatterers may be geometrically optimal. However, this geometric phase center position may not be *physically realistic*. In fact, the geometric position of the effective phase center may be 'floating' in free space or below the ground, while it is evident that radar reflections stem from real reflections on real physical objects, and should therefore be aligned with (the surface) of such an object. For example, for a perfect corner reflector, it is known that the effective scattering center can only be at the apex of the reflector, even though the best geometric position estimate may turn out to be in a different position. As a result, understanding the physical scattering mechanism may help in the realistic physical positioning of scatterers.

Fig. 1.6 is a conceptual sketch that illustrates various interactions between electromagnetic waves and an object on the ground. For a single trihedral scattering signal with orthogonal sides, e.g., a corner reflector, the phase center may be in its real physical position. However, this is significantly more complicated when it comes to multiple bounce signals.

Consequently, many observed signals may not be related only to a single object. Moreover, in a realistic urban scenario, the back-scattered signals are strongly dependent on the orientation, geometry, size and other characteristics of objects on the Earth's surface, as well as the parameters of the transmitted radar signals such as direction, wavelength, and polarization (Woodhouse, 2005). Thus, the multitudinous nature of scattering mechanisms in InSAR requires detailed analysis.

For instance, a five-fold bounce point scatterer from the observed object would be geolocated below ground and give an opposite displacement as the single bounce signal

from the object observed. The understanding of the physical mechanism would facilitate the interpretation of observed displacements.

In conclusion, the association of InSAR scatterers to real world objects involves (i) the sub-pixel location of the effective phase center of InSAR scatterers, (ii) the precise 3D geolocation by minimizing the positioning errors, and (iii) understanding of the complicated interactions between microwaves and objects in the complex urban environment.

1.4. Research objectives

Aiming to establish a one-to-one link of InSAR scatterers to real-world objects, the main research question of this thesis is:

How can we optimally associate InSAR scatterers to their corresponding geo-objects?

To answer this main question, three related research problems need to be considered.

1. How does the sub-pixel position of a dominant scatterer within the resolution cell affect the PSI estimates, in terms of geolocation and displacement?
2. How can we precisely and reliably geolocate InSAR scatterers by correcting for the positioning bias, which practical approaches are feasible, and when is it valuable to install physical ground control points in the area of interest?
3. Is the position of the geometric phase center the true physical source of the signal, and—if not—what effect does this have on the interpretation of the estimates?

In addressing these questions, this study consider them in the perspective of geodetic parameter estimation problems, from an engineering point of view. That is, we seek to find practical solutions and answers, which are generic for all types of satellite and SAR sensor systems, rather than focusing on demonstrating optimal results which can only be achieved for a specific satellite system. Ideally, our results should be directly translatable to operational geodetic decision making.

1.5. Outline and research methodology

We start this study in chapter 2 by providing a brief review of SAR interferometry, describing the characteristics of SAR measurements, InSAR observable, and time series InSAR analysis. Chapter 2 also serves as the technical background reference of this study. Special attention is given to the characteristics of InSAR point scatterers.

The three main chapter (3 – 5) cover the three main research problems described above. Fig. 1.7 is a schematic outline of this study, indicating these three chapters in the colored boxes.

In chapter 3, the influences of the sub-pixel correction on point positioning and deformation quality were analyzed. The relative position of a scatterer within a resolution cell causes an additional phase contribution in the observed phase, referred to as the sub-pixel phase, which needs to be accounted for in PSI processing. A detailed analysis of the sub-pixel phase component and its influences and propose a correction method has given as follows. The sub-pixel correction module is implemented in the delft implementation of persistent scatterer interferometry (DePSI) toolbox. Experiments are

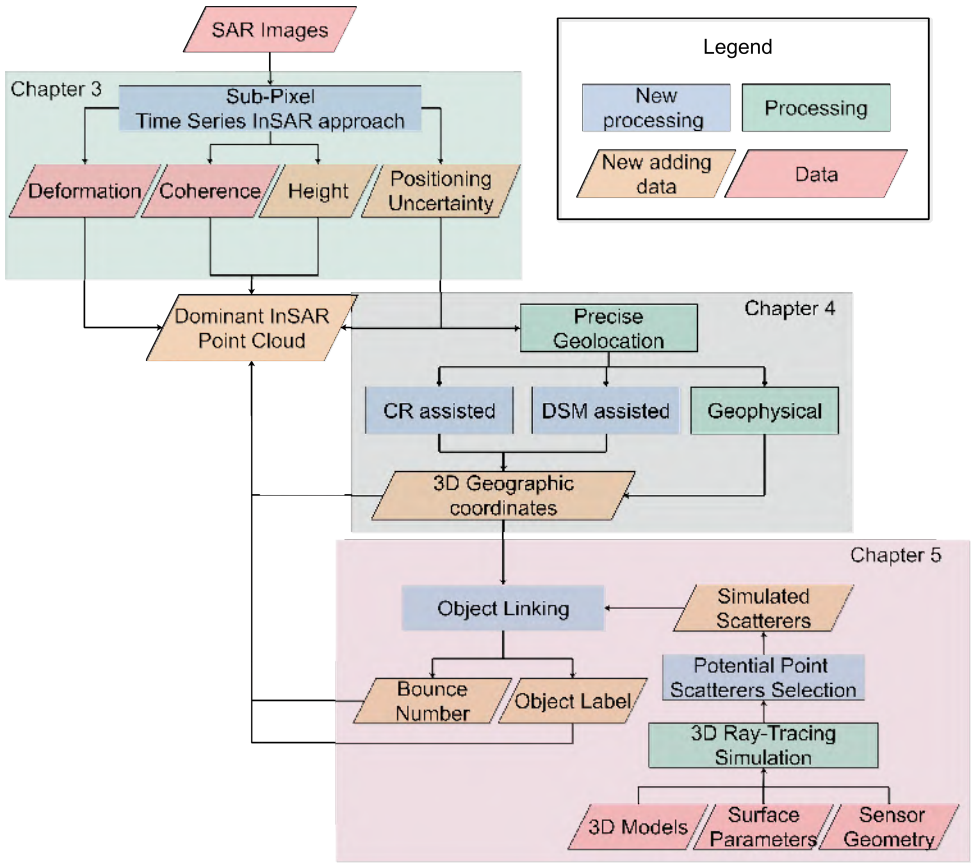


Figure 1.7: Simplified schematic summary of the attributes added and methodology developed in this thesis.

conducted using TerraSAR-X, Radarsat-2, and Sentinel-1 data stacks, which demonstrate the improvements in geolocations, elevations, and displacements by applying the sub-pixel correction. Chapter 3 was published in the *ISPRS Journal of Photogrammetry and Remote Sensing*, see Yang et al. (2020).

In chapter 4, we deal with the geolocation errors of InSAR scatterers. Here we present positioning correction methods based on using a single-epoch corner reflector (CR), multi-epoch CR, and high-precision LiDAR DSM. The value and necessity of using CR for different scenarios, concerning the required efforts, are compared with using a high-precision digital surface model (DSM) and advanced (geo)physical method. The applicability of the proposed methods was tested on TerraSAR-X and Sentinel-1 data stacks. The achieved positioning accuracy by the DSM-assisted approach is discussed with varying DTED levels considering the current open DSM data. We show that by employing the calculated offsets by CR-assisted or DSM-assisted approaches in the PS point cloud, geolocation errors can be mitigated as a post-processing step of PSI. Chapter 4 was published in the *ISPRS Journal of Photogrammetry and Remote Sensing*, see Yang

et al. (2019b).

Chapter 5 focuses on the understanding of physical scattering mechanisms with a Ray-tracing technique and develops a new approach to link persistent scatterers to real-world geo-objects through a 3D model, and addresses the importance of understanding the physical scattering mechanism of points on the interpretation of InSAR results. The chapter also discusses the level-of-detail required for the 3D model to obtain satisfactory results. Chapter 5 was published in the *IEEE Transactions on Geoscience and Remote Sensing*, see Yang et al. (2019a).

Conclusions, contributions, and recommendations of this study are reported in Chapter 6.

2

Time-series InSAR and InSAR scatterers

This chapter gives a technical review on SAR imaging, the InSAR technique and time series InSAR methods. The amplitude and phase components in a SAR image are presented in Section 2.1, with a discussion on the factors affecting these two observations. Section 2.2 describes the observable in the InSAR technique and gives a generic processing flow. The following Section 2.3 introduces the time series InSAR technique. The time series InSAR methods are classified based on baseline configuration, point selection criterion, and the deformation model. The potential improvements and limitations of the InSAR technique are also given in Section 2.3.

2.1. Synthetic aperture radar image

A synthetic aperture radar is an imaging radar that scans the Earth's surface with microwave radiation. Fig. 2.1 describes the configuration of a SAR system. The SAR antenna, carried by a moving aircraft or spacecraft platform, sequentially transmits electromagnetic waves and collects the back-scattered signals in a side-look viewing geometry. The direction of the moving platform is the azimuth direction, and the line of sight (LOS) is the slant range direction. The illuminated area of each beam in the ground is called the footprint. The swath describes the coverage area of SAR image in azimuth and ground range direction. The received echos form the so-called raw data, which need to be processed by the range and azimuth compression (Bennett and Cumming, 1979; Wu et al., 1981; Curlander and McDonough, 1991; Raney et al., 1994; Cumming and Wong, 2005a) to form a SAR image.

A SAR image is a digital representation of an illuminated area, which can also be seen as a two-dimensional pixel matrix. Each pixel denotes one complex number Z ,

$$Z = Ae^{j\psi}, \quad (2.1)$$

where j is the imaginary unit, $A \in \mathbb{R}^+$ is the amplitude, and $\psi \in [-\pi \pi)$ is the phase. All scattering elements within the corresponding resolution cell contribute to this complex

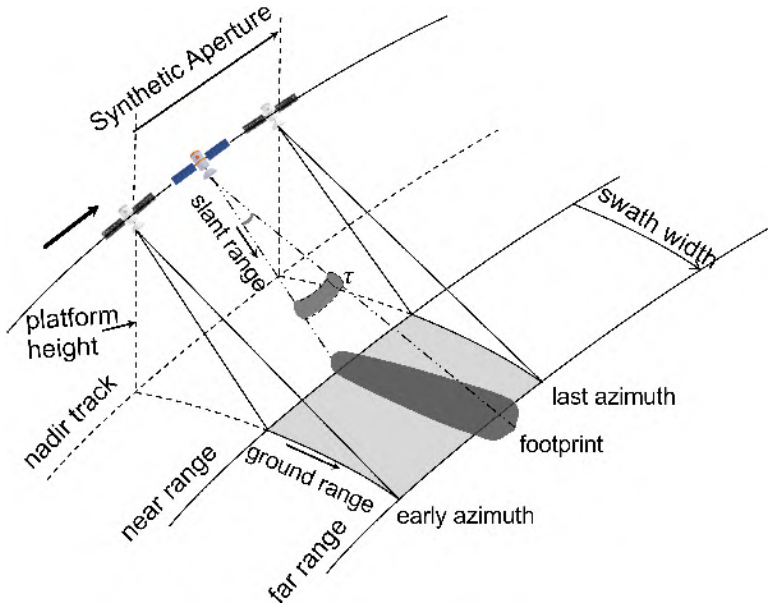


Figure 2.1: Scanning configuration for a right looking SAR, altered from Hanssen (2001).

number. In following sections, we describe the SAR measurement by explaining the amplitude and phase data.

2.1.1. Amplitude

The amplitude component of each pixel is given by

$$A = \sqrt{\text{Re}(Z)^2 + \text{Im}(Z)^2}, \quad (2.2)$$

where the $\text{Re}(Z)$ and $\text{Im}(Z)$ are the real and imaginary parts of Z . The amplitude is affected by

- the physical shape and size of the illuminated object,
- the orientation of the object with respect to the observation geometry,
- the surface roughness and composition of the illuminated area or volume,
- the environmental conditions (e.g., moisture),
- the frequency and polarization of the radar signal, and
- Dielectric properties of the target.

The amplitude is related to the detectability of a target, a target with strong amplitude is easier to detect than a target with weak amplitude. In general, urban areas show strong backscattering signals, while vegetation region and water give low intensities.

Fig. 2.2b gives an example of the amplitude of a SAR image. The data is acquired by TerraSAR-X satellite over the campus of TU Delft. Bright pixels are from the buildings and infrastructures, while the canal appears as dark areas.

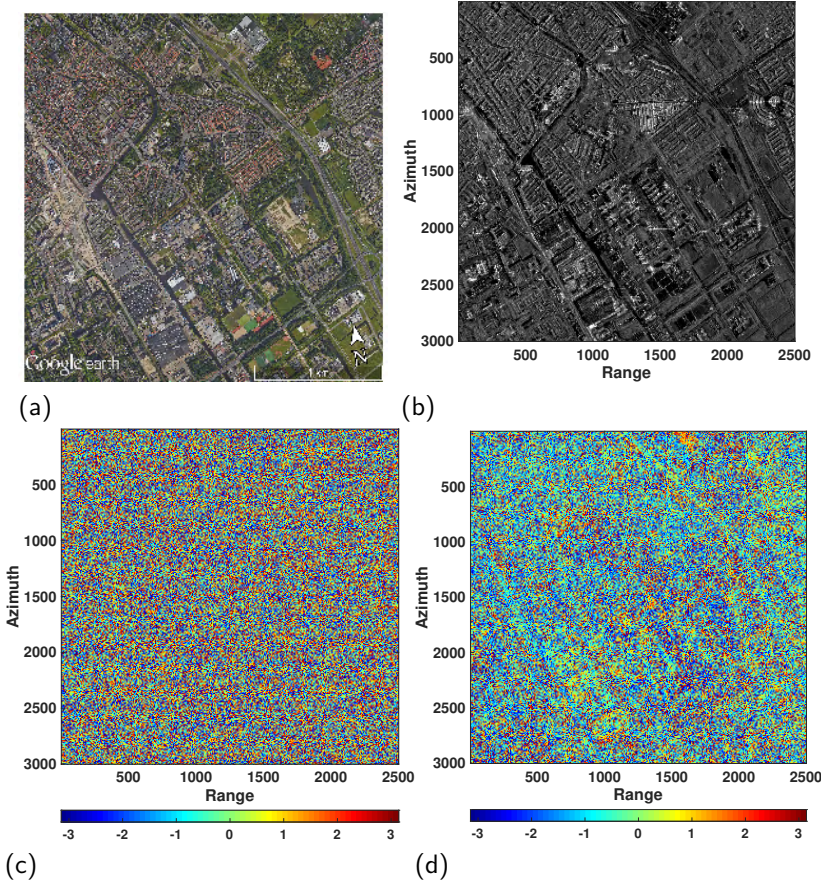


Figure 2.2: TU Delft Campus in (a) airborne optical image, (b) amplitude image from TerraSAR-X stripmap data, (c) phase image from TerraSAR-X Stripmap data, (d) interferometric phase image from a pair of TerraSAR-X Stripmap data.

2.1.2. Phase

The phase component of each pixel is given by

$$\psi = \arg(Z), \tag{2.3}$$

where $\arg(\cdot)$ returns the phase angle in $[-\pi \pi)$ of complex Z . The operation $\arg(\cdot)$ uses the four-quadrant inverse tangent function to compute the angle between the real and imaginary axis from the origin to the point $(\text{Re}(Z), \text{Im}(Z))$ in the complex plane, see Fig. 2.3.

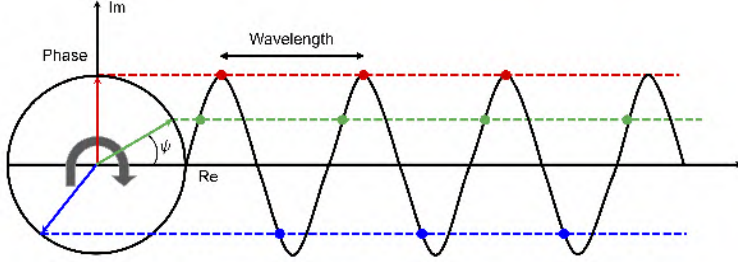


Figure 2.3: The measured phase in a SAR image is the fractional phase of the received radar signal.

The phase component is proportional to the length of the propagation path. The propagation path is the two-way travel distance (sensor - target - sensor). Fig. 2.3 describes the relation of observed phase and the two-way path with a sinusoidal signal. The observed phase is the travel distance divided by the wavelength as given in

$$\psi = W \left\{ 2\pi \frac{2r}{\lambda} \right\}, \quad (2.4)$$

where $W\{\cdot\}$ is modulo- 2π wrapping operator, r is the distance corresponding to the phase, and λ is the wavelength. The phases in a SAR image are wrapped ranging from $-\pi$ to π .

The phase measurement is affected by

- the two-way propagation path, including atmosphere-induced delays,
- the interaction between the waves and the scatterers within the resolution cell, and
- potential phase shifts induced by the processing.

Phase measurement from pixel to pixel in SAR image looks as a random value. Fig. 2.2c gives an example of phase image. The phase value is ranging from $-\pi$ to π in each pixel, and show no correlation among them.

2.2. SAR interferometry

The principle of SAR interferometry is to exploit the differential phase between two SAR images. Fig. 2.4 describes the concept of SAR interferometry. Two SAR images, master and slave, are acquired at slightly different viewing position or at a different time. The phase of each SAR image is proportional to the two-way travel distances, thus the phase differences between two SAR image can be usefully exploited to generate the topography, or the displacement during the acquisition interval.

An interferogram is generated by complex-conjugate multiplication of two coregistered SAR images. Each pixel in the interferogram I_{ms} is a complex number given by

$$I_{ms} = Z_m Z_s^* = A_m A_s e^{j(\psi^m - \psi^s)} = A_m A_s e^{j\phi^{ms}}, \quad (2.5)$$

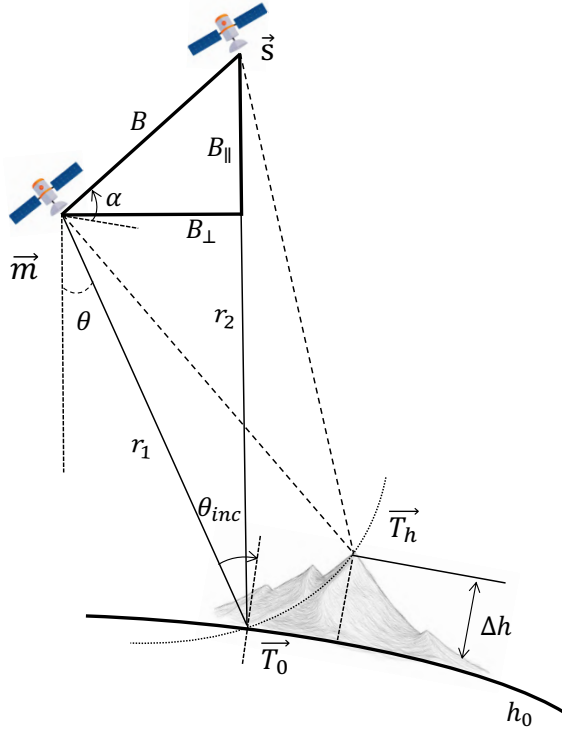


Figure 2.4: InSAR geometry for point \vec{T}_h with height Δh above the reference height h_0 , the flight direction is perpendicular to the view plane.

where Z_m and Z_s denote the complex value of a pixel in the master and slave image, A_m and A_s are the respective amplitudes, ψ^m and ψ^s are the respective phases, and ϕ^{ms} is the interferometric phase.

Fig. 2.2d gives an example of interferometric phase. As described in Section 2.1, the phases of one SAR image essentially give no information, while the phase differences between two SAR images enable measuring the path differences. The interferometric phase is proportional to the differences in travel distances due to viewing geometry or displacement. Fig. 2.5 illustrates how the path changes Δr can be accurately measured by the interferometric phase.

2.2.1. Observable

The observable in SAR interferometry is the interferometric phase, given by

$$\phi^{ms} = \arg(Z_m Z_s^*) = W\{\psi^m - \psi^s\} = W\{\phi_{range} + \phi_{atmo} + \phi_{scat} + \phi_{noise}\}, \quad (2.6)$$

where $W\{\cdot\}$ is the wrapping operator of the phase value in $[-\pi, \pi)$, and ψ^m and ψ^s are the phases in master and slave image. The interferometric phase, ϕ^{ms} , contains four components: the range dependent phase ϕ_{range} , the atmospheric phase ϕ_{atmo} , the scat-

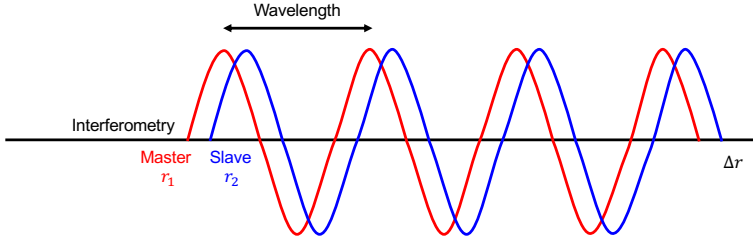


Figure 2.5: The interferometric phase is the phase difference between the master and slave image, and proportional to the distance difference between two travel paths.

tering phase ϕ_{scat} , and the noise phase ϕ_{noise} . Fig. 2.6 gives a further decomposition of the interferometric phase.

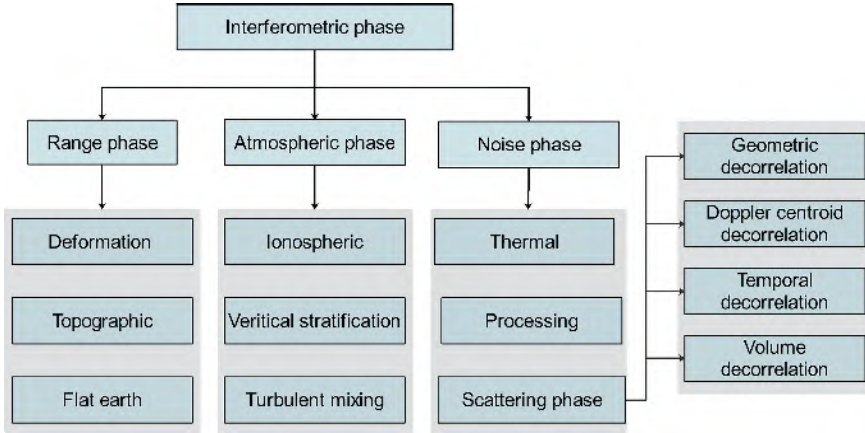


Figure 2.6: Decomposition of interferometric phase in different contributing factors.

The range-dependent phase relates to the differential range distance between master and slave image including topographic ϕ_{topo} (including object height), the flat earth phase ϕ_{ref} , and deformation ϕ_{defo} , and can be written as

$$\phi_{\text{range}} = \phi_{\text{topo}} + \phi_{\text{ref}} + \phi_{\text{defo}}. \quad (2.7)$$

The topographic and flat earth phases are dependent on the viewing geometry of the satellite. The flat earth phase is the phase contribution due to the reference earth surface (e.g., and ellipsoidal surface) and is also known as the reference phase. The topographic phase describes the topography above the reference surface, i.e., the topographic elevation and the elevation of the scatterer if it is situated on an object, e.g., a building. The topographic phase is defined as

$$\phi_{\text{topo}} = -\frac{4\pi}{\lambda} \frac{B_{\perp}}{r_1 \sin \theta_{\text{inc}}} \cdot \Delta h, \quad (2.8)$$

where λ is the wavelength, B_{\perp} is the perpendicular baseline between master and slave, r_1 is the range to the antenna, θ_{inc} is incidence angle, Δh is the height above the ellipsoid surface, see Fig. 2.4.

The reference phase is defined as

$$\phi_{\text{ref}} = -\frac{4\pi}{\lambda} B \sin(\theta - \alpha), \quad (2.9)$$

where B is the baseline between the master and slave, θ is look angle, and α is the baseline orientation.

The deformation phase corresponds to the cumulative displacement between two acquisitions, and is given as

$$\phi_{\text{defo}} = -\frac{4\pi}{\lambda} d_{\text{LOS}}, \quad (2.10)$$

where d_{LOS} is the projection of deformation in 3D space onto the line of sight (LOS). Supposing the deformation is $[D_e \ D_n \ D_u]$ in east, north and vertical direction in 3D space, the observed displacement in the LOS is

$$d_{\text{LOS}} = D_e \sin\theta_{\text{inc}} \cos\alpha_h - D_n \sin\theta_{\text{inc}} \sin\alpha_h - D_u \cos\theta_{\text{inc}}, \quad (2.11)$$

where α_h is the heading angle of the satellite. Consequently, a horizontal displacement in the eastern direction translates in an opposite displacement in the LOS direction for the ascending and descending viewing geometry, respectively.

The atmospheric phase is caused by the difference in the atmospheric delay between master and slave image. The atmospheric delays in the SAR image contain two parts: the ionospheric, and tropospheric phases. The ionospheric phase is wavelength-dependent (Zebker et al., 1997; Gray et al., 2000), and stems from the upper layer of the Earth's atmosphere, from about 80 to 600 km above sea level. The ionospheric delay is induced by the electron density variation along the path and can be estimated from the total electron content (TEC). Since the TEC shows a significant spatial correlation (Meyer et al., 2006), the ionospheric phase differences are smaller than the differential tropospheric phase over short distances. The tropospheric phase is a delay originating in the lower layer of the atmosphere, from 0 to 12 km above sea level, which can be decomposed into the hydrostatic and wet delay. The hydrostatic delay depends on the temperature and pressure which is relatively constant in spatial extent (Bevis et al., 1992). Thus, the differential atmospheric phase is only slightly affected by this term. The wet delay depends on the water vapor distribution (Bevis et al., 1992), and shows a larger spatial and temporal variation. For a short spatial scale (~ 50 km), the dominant differential atmospheric phase is due to the water vapor variation (Hanssen, 2001). The tropospheric delay is the biggest contributor to the differential atmospheric phase. According to Hanssen (2001), the tropospheric phase can be divided into two parts: vertical stratification and turbulent mixing.

The scattering phase is caused by temporal changes in the geometry or the position of scattering elements within the resolution cell between the master and the slave acquisition. As described in Section 2.1.2, the phase of each pixel affected by all scattering elements in the corresponding resolution cell. Therefore, the change in position or electrical characteristic of each scattering element results in the scattering phase. It can be viewed as a phase noise term.

The interferometric coherence γ is an indicator to evaluate the scattering changes. The coherence is the magnitude of the correlation coefficient between the master and the slave, ranging from 0 to 1. A coherence of 1 means that there are no changes between the two acquisitions. A coherence equals to 0 indicating total decorrelation between two acquisitions. Four decorrelation sources are defined: baseline, varying squint angle (Doppler), temporal, and volume decorrelation.

Baseline decorrelation refers to the effect due to the different incidence angles between the master and the slave acquisitions. A large incidence angle difference leads to a larger baseline decorrelation than with similar incidence angles between two acquisitions. The degree of geometrical decorrelation is denoted by γ_{base} . Similarly, the changes in the squint angle cause decorrelation in azimuth, resulting in the varying of the Doppler centroid, which is referred to as Doppler centroid decorrelation. The degree of Doppler centroid decorrelation is indicated by γ_{dc} . Temporal decorrelation is caused by variations within the corresponding resolution cell between two acquisitions. Vegetation cover in the area of interest will cause obvious temporal decorrelation effects due to the different periods of vegetation growth. The degree of temporal decorrelation is written as γ_{temp} . Finally, volume decorrelation results from the height distribution of the backscattering cross-section in an imaged space (Alberga, 2004), such as forests or buildings, and is represented by γ_{vol} .

The system temperature and the approximations in data processing also induce a phase noise. Combining all the above components, the coherence can be further defined as (Zebker and Villasenor, 1992)

$$\gamma = \gamma_{\text{base}} \cdot \gamma_{\text{temp}} \cdot \gamma_{\text{dc}} \cdot \gamma_{\text{vol}} \cdot \gamma_{\text{ther}} \cdot \gamma_{\text{pro}} \cdot \gamma_{\text{amb}}, \quad (2.12)$$

where γ_{ther} , γ_{pro} , and γ_{amb} are the decorrelation term due to system thermal noise, data processing, and imaging ambiguities due to the far away clutter, respectively.

2.2.2. Processing procedure

In this section, the processing procedure of SAR interferometry (InSAR) is briefly introduced. The InSAR method has been implemented in lots of data processing algorithms. Here we focus on the key steps that these all have in common. Fig. 2.7 is a flow diagram with these main processing steps. The final result of the InSAR method could be a topographic map or a displacement map, depending on the geometry and temporal separation of the SAR images. The processing is started using two single look complex (SLC) images. Note that the pre-processing on raw signals, i.e. the focusing, is not considered here.

First, the slave image is aligned and re-sampled to the master image grid. The coregistration deals with the geometrical misalignment and distortion resulting from having slightly different viewing geometries, such as the changes in incidence angle, antenna position, or different sampling rates. Two steps are typically included in the coregistration: coarse coregistration based on an a priori available DEM and orbit information, and fine coregistration based on amplitude or complex cross-correlation. The final coregistration result requires sub-pixel level accuracy. Oversampling is performed in order to avoid the aliasing effect (Hanssen, 2001) due to spectrum widening resulting from

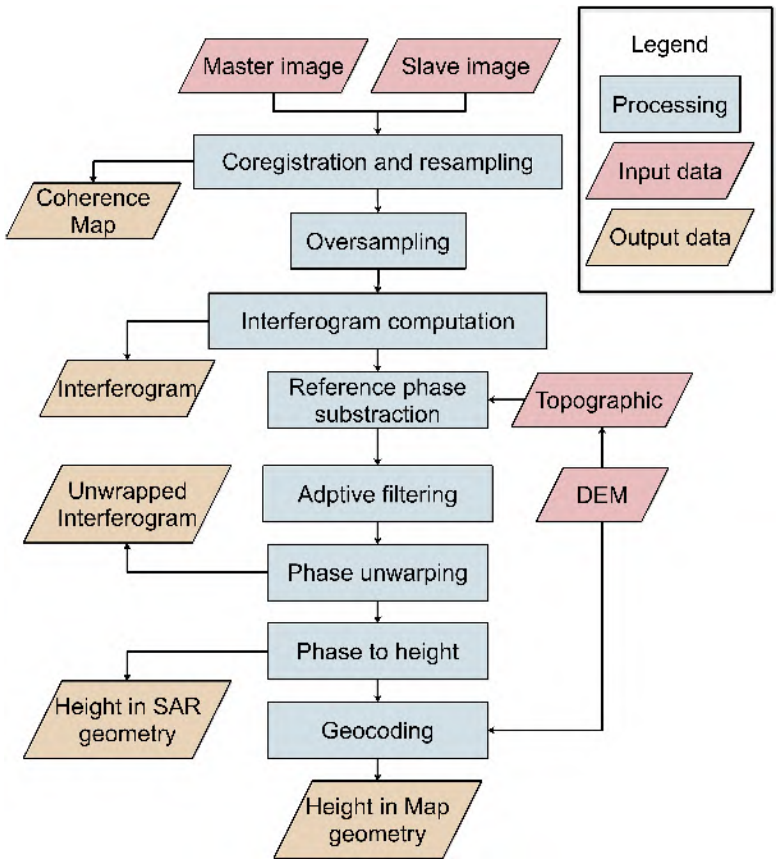


Figure 2.7: Generic processing flowchart of SAR interferometry.

interferometry. The interferogram is generated by complex conjugate multiplication of the master and the resampled slave image.

Then the contributions of the topography and the ‘flat earth’ phase terms are removed in order to reduce the phase variation. An external DEM is used for topographic phase calculation, and the interferograms are produced by subtracting the flat earth and topographic phase components from the original interferograms. Adaptive filtering based on local noise level (Lee et al., 1998) can eventually be performed to reduce phase noise.

Phase unwrapping is the most challenging step in InSAR processing. As introduced in Section 2.2.1, the interferometric phases are wrapped. The goal of the phase unwrapping is to estimate the integer cycle. Phase unwrapping is an inherently undetermined inverse problem. Algorithms were developed to find the most likely solution by making two assumptions (Hunt, 1979; Goldstein et al., 1988; Costantini, 1996; Bamler et al., 1998): (i) the gradients between the wrapped and unwrapped phase should be equal, and (ii) the phase differences between two neighboring points are less than π , or less

than a quarter of the physical wavelength, see Eq. (2.10). Obviously, these assumptions are not always conform reality.

The last two steps are the phase-to-height conversion and the geocoding procedure. The unwrapped phase is converted either to height or to displacements according to Eqs. (2.8) or (2.10). Geocoding refers to the procedure of converting the results in radar coordinates to map coordinates or a local coordinate system. It enables the application of InSAR results.

2.2.3. Limitations

Main limitations of the conventional repeat-pass InSAR technique are (i) the atmospheric inhomogeneities (Zebker et al., 1997; Hanssen, 2001; Jolivet et al., 2014; Li et al., 2019b), (ii) decorrelation due to scattering phase and noise phase (Zebker and Villasenor, 1992; Hanssen, 2001), (iii) phase ambiguity estimation (Ghiglia and Pritt, 1998).

2.3. SAR interferometric time series analysis

The advent of interferometric time-series analysis is a response to the limitations of InSAR, as addressed above. Time series InSAR techniques use a set of multiple SAR images, subsequently acquired over time, to estimate displacements of the Earth's surface or objects on it. Interferograms are generated following a rule of baseline configuration among the SAR images. Coherent points are selected for phase analysis. The deformation information is estimated along with the height under an assumption of deformation behavior.

The atmospheric phase is considered to be spatially correlated and temporally uncorrelated, the stacking methods (Zebker et al., 1997; Wright et al., 2001) are proposed for removing the atmospheric contribution by temporally averaging interferograms. Exploration of the coherent features in a long time series proved to be an effective method for deformation extraction (Usai and Hanssen, 1997). The framework of time series InSAR, named persistent scatterer interferometry (PSI), was first proposed by Ferretti et al. (2001). PSI explores a single master stack of interferograms and a group of coherent pixels, named persistent scatterers (PS). The PS pixels do not suffer from the decorrelation problem, enabling robust deformation estimation. Berardino et al. (2002) presented a small baseline subset technique (SBAS) that using multi-looked and unwrapped interferograms that formed with short baselines configuration for displacement estimation. PSI and SBAS are the most representative methods of two categories of time series techniques, for exploring the pixels with different types of scattering mechanisms and completed each other.

A number of stack processing approaches have been proposed with different baseline configurations, exploration of pixels with different scattering mechanisms, and adoption of different deformation model. The PSI and SBAS here are not referring to one particular method, but referring to a group of methods with similar characteristics. PSI approach denotes the analysis with PS pixels and single master configuration (Werner et al., 2003; Hooper et al., 2004; Kampes, 2005; Costantini et al., 2008; van Leijen and Hanssen, 2004; Lv et al., 2014), while SBAS approach specifies the processing with DS pixel and small baseline configuration (Mora et al., 2003; Schmidt and Bürgmann, 2003;

López-Quiroz et al., 2009; Pepe et al., 2011, 2015). There is also a hybrid method combining features of the two categories (Hooper, 2008; Hetland et al., 2012; Devanathéry et al., 2014; Goel and Adam, 2014). Considering the target decorrelation in estimation processing, current solution try is to extract all information in SAR stacks (Guarnieri and Tebaldini, 2008; Ferretti et al., 2011; Perissin and Wang, 2012; Fornaro et al., 2015; Samiei-Esfahany et al., 2016). Tab. 2.1 summarizes the characteristics of common time series analysis techniques.

2.3.1. Baseline configuration

Baseline configuration is the combination of multiple SAR images. The baseline can be a geometrical baseline (the position of two acquisitions), temporal baselines (time interval of two acquisitions), or Doppler baseline (the Doppler centroid frequency variation). Fig. 2.8 shows several examples of baseline configuration of 64 images with a time span of five years.

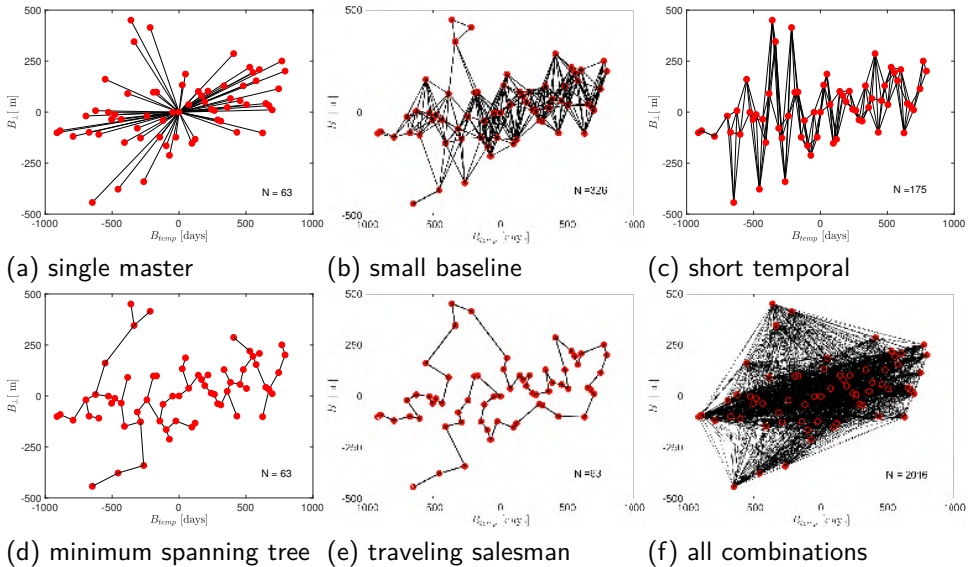


Figure 2.8: Examples of baseline configuration. (a) single master configuration, (b) short temporal and perpendicular baseline configuration, (c) short temporal combination of SAR images delivers a cascade interferograms as Fig. 2.8c shown, which permits larger and irregular deformation in time. Figs. 2.8d and e show the minimum spanning tree (Perissin, 2008) and traveling salesman (van Leijen and Hanssen, 2004) configuration that link all available images. Fig. 2.8f provides the all possible combination among the acquired images.

Fig. 2.8a shows a single master configuration where all images are referenced to a single master image, which is a common configuration in the PSI method. Fig. 2.8b illustrates the small baseline configuration where all the baselines between interferogram pairs are shorter than the set threshold. Short temporal combination of SAR images delivers a cascade interferograms as Fig. 2.8c shown, which permits larger and irregular deformation in time. Figs. 2.8d and e show the minimum spanning tree (Perissin, 2008) and traveling salesman (van Leijen and Hanssen, 2004) configuration that link all available images. Fig. 2.8f provides the all possible combination among the acquired images.

Table 2.1: Characteristics of main time series InSAR techniques.

Method		Configuration	Point Selection	Deformation model
PSI	(Ferretti et al., 2001)	single master	amplitude dispersion	linear in time
SBAS	(Berardino et al., 2002)	small baselines	coherence	spatial smoothness
PSI	(Mora et al., 2003)	small baselines	coherence	linear and Non-Linear in time
PSI	(Schmidt and Bürgmann, 2003)	small baselines	coherence	spatio-temporal smoothness
IPTA	(Werner et al., 2003)	single master	amplitude & phase diversity	linear in time
STAMPS	(Hooper et al., 2004)	single master	amplitude & phase criterion	spatial smoothness
PSI	(Crosetto et al., 2005)	small baseline	coherence	stepwise linear in time
STUN	(Kampes, 2006)	single master	amplitude dispersion & SCR	multiple deformation types
STAMPS+	(Hooper, 2008)	small baselines	amplitude & phase criterion	spatial smoothness
PSP	(Costantini et al., 2008)	single master	arc-pair PS selection	linear in time
SBAS	(López-Quiroz et al., 2009)	small baselines	coherence	spatial smoothness
SqueeSAR	(Ferretti et al., 2011)	all combinations	covariance matrix	deformation in time
EMCF-SBAS	(Pepe et al., 2011, 2015)	small baseline	Phase criterion	spatial smoothness
Quasi-PS	(Perissin and Wang, 2012)	target-dependent	partially coherent target	linear in time
MInTS	(Hetland et al., 2012)	small baselines	coherence	deformation in time
DePSI	(van Leijen, 2014)	single master	amplitude dispersion	multiple deformation types
DSI	(Goel and Adam, 2014)	small baselines	statistical homogeneity test	linear in time
JS-TSInSAR	(Lv et al., 2014)	single master	statistical homogeneity test	linear in time
Cousin PS	(Devanathéry et al., 2014)	small baselines	amplitude dispersion	spatial smoothness
CEASAR	(Fornaro et al., 2015)	all combinations	covariance matrix	deformation in time
DS-TSInSAR	(Samiei-Esfahany et al., 2016)	all combinations	covariance matrix	multiple deformation types

The choice of baseline configuration depends on the data stacks, the study area, and the deformation signal. In the case of long-term linear deformation in an urban area and the used data stack obtained from a satellite with a well-controlled orbit and short revisit period, the single master and small baseline configuration are both good choices. The small temporal configuration may have the risk of error propagation. In case of landslide monitoring in vegetation region, the short perpendicular and/or temporal baseline configuration (Li et al., 2019a) ensures coherence.

2.3.2. Coherent scatterers

Two kinds of pixels with different scattering mechanisms are employed in time series analysis, point scatterers and distributed scatterers (DS) (Hu et al., 2019). A reflecting object whose signal dominates the pixel and keeps coherent over the entire time is called Persistent Scatterer. Persistent scatterers are easily found in an urban scene.

DS pixels contain a group of small scattering objects, and the changing of the small scattering elements would introduce decorrelation. The appropriate baseline configuration may minimize the decorrelation. Multi-look processing effectively reduces the noise but it does not apply to PS pixels. Usually, the PS pixels show a different scattering signal with the surroundings, thereby the multi-look processing would disturb the measurement of PS pixels. Methods based on DS pixel are commonly used in non-urban areas.

Fig. 2.9 illustrates the comparison between PS and DS pixels. Figs. 2.9a and 2.9b show the scattering elements within the resolution cell. PS pixel contains one strong reflector, while DS pixel contains a group of small reflectors. A hundred simulations are made while the location of scattering elements are changed randomly. The phasors and phase components of 100 simulations are given in Figs. 2.9c-f. The measurement of PS pixel is dominant by the largest reflector with a small deviation due to the clutter. The phase of PS pixel in each simulation is around the ϕ_{ps} , while the phase of DS pixel is ranging from $-\pi$ to π .

Selection criteria for coherent points are based on amplitude or coherence. Here we summarize some frequently-used indicators.

- Normalized amplitude dispersion D_A . It is calculated as

$$D_A = \frac{\sigma_A}{\mu_A}, \quad (2.13)$$

where σ_A is the standard deviation of the amplitude over time, and μ_A is the mean amplitude value over time for a pixel. The normalized amplitude dispersion is an index for phase variability (Ferretti et al., 2001)—a low D_A suggests a stable amplitude value which is dominated by one strong scattering object within the resolution cell. In case of a high signal to noise ratio, D_A is approximately equal to σ_ψ .

- Amplitude threshold. Pixels with the value larger than A_t in at least N_t images are chosen as PS (Adam et al., 2004). The A_t and N_t are dependent upon the number of acquisitions N and the sensor characteristics.

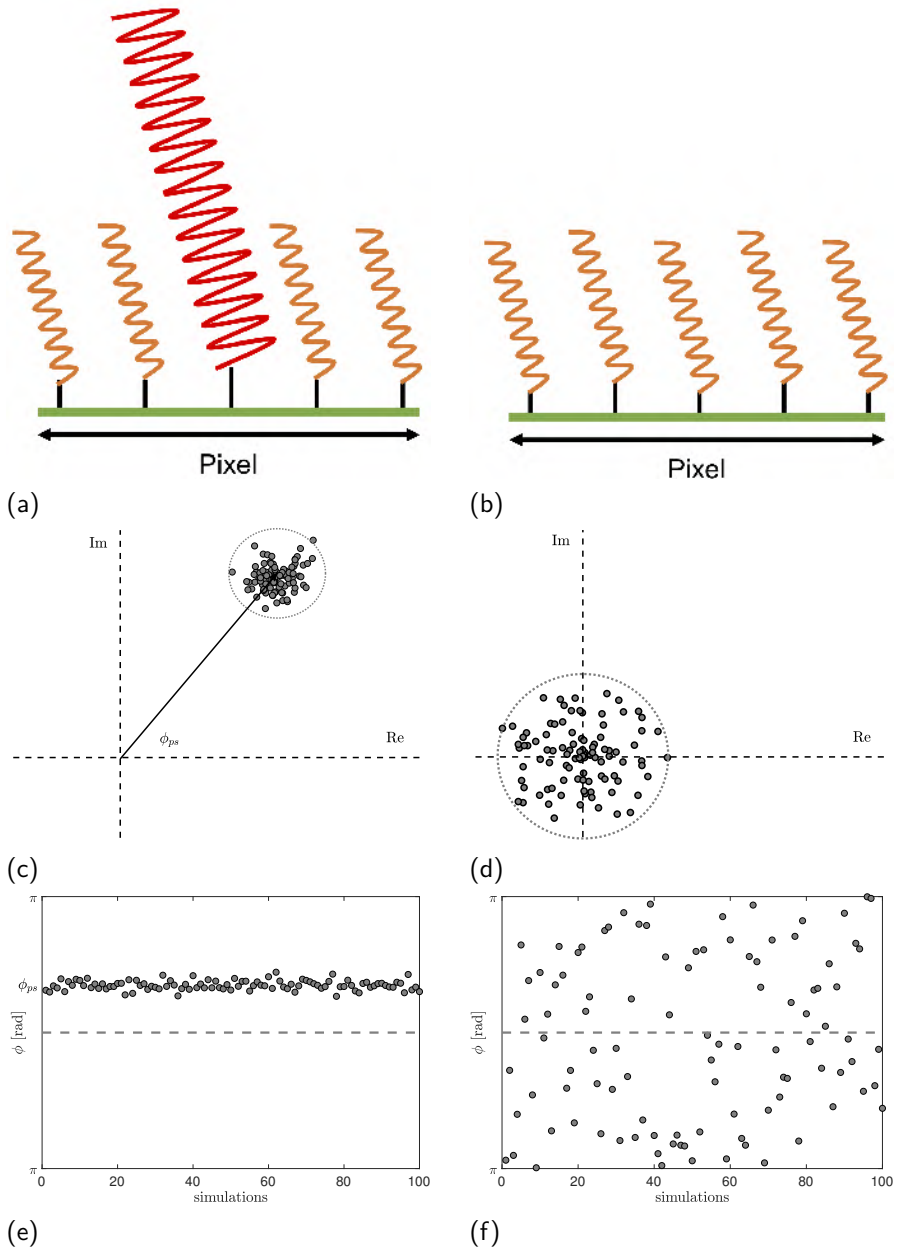


Figure 2.9: Point scatterer and distributed scatterer. (a) and (b) display the resolution cells of point scatterer and distribute scatterer. (c) and (d) illustrate the phasors of 100 simulations of point scatterer and distribute scatterer. In each simulation, the locations of scattering elements are changed randomly. (e) and (f) show the phase behavior of 100 simulations.

- Signal to Clutter Ratio SCR. It is calculated as

$$\text{SCR} = \frac{A_s^2}{A_c^2}, \quad (2.14)$$

where A_s is the amplitude of the central pixel (the signal), A_c is the amplitude of the surrounding neighboring pixels (the clutter). The SCR is also an indicator for phase variability (Adam et al., 2004), σ_ψ is approximately equal to $(\sqrt{2} \cdot \text{SCR})^{-1}$. In urban areas, the clutter is frequently overestimated.

- Coherence γ . It is estimated as

$$\hat{\gamma} = \frac{\sum_{i=1}^l Z_{i,m} \cdot Z_{i,s}^*}{\sqrt{\sum_{i=1}^m |Z_{i,m}| \cdot \sum_{i=1}^m |Z_{i,s}|}}, \quad (2.15)$$

where l is number of surrounding pixels. Spatial coherence $\hat{\gamma}$ (Touzi et al., 1999) is estimated based on a window and a commonly used evaluator for the DS pixels.

- Amplitude difference dispersion $D_{\Delta A}$. It is calculated as

$$D_{\Delta A} = \frac{\sigma_{\Delta A}}{\mu_A}, \quad (2.16)$$

where $\sigma_{\Delta A}$ is the standard deviation of the amplitude difference. The $D_{\Delta A}$ is pixel level calculation, which is better for selecting DS pixel in SLC level (Hooper, 2008).

- Ensemble coherence or phase noise $\hat{\gamma}_{\text{ec}}$. It is estimated as

$$\hat{\gamma}_{\text{ec}} = \frac{1}{N} \left| \sum_{k=1}^N \exp[j(\phi_{i,k} - \phi_{i,k}^{\text{sc}} - \phi_{i,k}^\theta)] \right|, \quad (2.17)$$

where N is number of acquisitions, $\phi_{i,k}$ is the interferometric phase of pixel i in k image, $\phi_{i,k}^{\text{sc}}$ is the estimate for spatially-correlated terms, and $\phi_{i,k}^\theta$ is spatially-uncorrelated look angle error term. Hooper et al. (2004) proposed $\hat{\gamma}_{\text{ec}}$ for evaluating the phase noise of each pixel. The $\hat{\gamma}_{\text{ec}}$ is a posterior indicator, thus the pixel selection and phase estimation could be done an iteration way.

- Spectral correlation along time between sub-looks (Iglesias et al., 2012) $\hat{\gamma}_{\text{tmp}}$. It is estimated as

$$\hat{\gamma}_{\text{tmp}} = \frac{\sum_{l=1}^N Z_{1,i,l} \cdot Z_{2,i,l}^*}{\sqrt{\sum_{l=1}^N |Z_{1,i,l}| \cdot \sum_{l=1}^N |Z_{2,i,l}|}}, \quad (2.18)$$

where N is number of acquisitions, Z_1 and Z_2 are the complex values from pixel i at first and second sub-looks. $\hat{\gamma}_{\text{tmp}}$ only uses the spectral properties of pixels and does not require the amplitude calibration. Temporal entropy of sub-looks can be used in when at least two sublooks are available, which is more sensitive with high coherence areas.

2.3.3. Mathematical models

The mathematical model of time-series InSAR analysis includes two parts: the function model and the stochastic model. The observations are the phase component of each point of the SAR images. Supposing there are two points i and j in two images m and s , the corresponding observation vector is

$$\omega = \left[\psi_i^m \quad \psi_j^m \quad \psi_i^s \quad \psi_j^s \right]^T. \quad (2.19)$$

The double difference phase observation per arc between the two points is

$$\phi_{ij}^{ms} = W\{\phi_i^{ms} - \phi_j^{ms}\} = -2\pi a + \Delta\phi_{ij,\text{defo}} + \Delta\phi_{ij,\text{topo}} + \Delta\phi_{ij,\text{atmo}} + \Delta\phi_{\text{noise}^*}, \quad (2.20)$$

where $\Delta\phi_{ij,\text{topo}}$ is the topographic phase due to the height difference between point i and point j and given by

$$\Delta\phi_{ij,\text{topo}} = -\frac{4\pi}{\lambda} \left(\frac{B_{\perp}}{r_i \sin\theta_{\text{inc},i}} h_i - \frac{B_{\perp}}{r_j \sin\theta_{\text{inc},j}} h_j \right). \quad (2.21)$$

Assuming $h_i = 0$, the height difference h_{ij} can be estimated. Thus, the height estimation of each point is related to one selected reference point. The height bias in the reference point would cause a shift in each point.

The displacement components $d(B_T^{ms})$ is modeled by a function of the B_T^{ms} between image m and s ,

$$\Delta\phi_{ij,\text{defo}} = -\frac{4\pi}{\lambda} d(B_T^{ms}). \quad (2.22)$$

The most common model is the linear (steady-state) deformation model, given by

$$d(B_T^{ms}) = B_T^{ms} \cdot v. \quad (2.23)$$

The estimated velocity v is likewise relative to the reference point. Usually, a stable point with highest coherence value is selected as the reference point. The linear model could be further extended by including a periodic model (Kampes and Adam, 2006),

$$d(B_T^{ms}) = B_T^{ms} \cdot v + A \sin(2\pi(B_T^{ms} - t_0)) + A \sin(2\pi t_0), \quad (2.24)$$

where A is the amplitude and t_0 is the initial value at $B_T^{ms} = 0$. Multiple deformation models are possible, the appropriate deformation model can be determined by hypothesis testing (Chang and Hanssen, 2016).

The atmospheric variation between points i and j in m and s image is given by

$$\Delta\phi_{ij,\text{atmo}} = \phi_{i,\text{atmo}}^{ms} - \phi_{j,\text{atmo}}^{ms}. \quad (2.25)$$

The noise term and decorrelation term are summarized in $\Delta\phi_{\text{noise}^*}$. Noise and atmospheric components are eliminated by spatio-temporal filter based on the assumption that noise term is both uncorrelated in space and time, and the atmospheric term is uncorrelated in time as long as the temporal baseline is longer than one day, but correlated in space. The estimated vector of each point is $[h_j \ v \ \phi_{j,\text{atmo}} \ a]$ with linear deformation model, or $[h_j \ t_0 \ A \ \phi_{j,\text{atmo}} \ a]$ with linear and periodic model.

The covariance matrix of the observations ω is

$$D\{\omega\} = \begin{bmatrix} \sigma_{\psi_i^m}^2 & \sigma_{\psi_i^m, \psi_j^m}^2 & \sigma_{\psi_i^m, \psi_i^s}^2 & \sigma_{\psi_i^m, \psi_j^s}^2 \\ \sigma_{\psi_i^m, \psi_j^m}^2 & \sigma_{\psi_j^m}^2 & \sigma_{\psi_j^m, \psi_i^s}^2 & \sigma_{\psi_j^m, \psi_j^s}^2 \\ \sigma_{\psi_i^m, \psi_i^s}^2 & \sigma_{\psi_j^m, \psi_i^s}^2 & \sigma_{\psi_i^s}^2 & \sigma_{\psi_i^s, \psi_j^s}^2 \\ \sigma_{\psi_i^m, \psi_j^s}^2 & \sigma_{\psi_j^m, \psi_j^s}^2 & \sigma_{\psi_i^s, \psi_j^s}^2 & \sigma_{\psi_j^s}^2 \end{bmatrix}, \quad (2.26)$$

where $\sigma_{\psi_i^m}^2$, $\sigma_{\psi_j^m}^2$, $\sigma_{\psi_i^s}^2$, and $\sigma_{\psi_j^s}^2$ are the variances of the phase observations in SAR images, consisting of noise, decorrelation, atmospheric, orbital, and unmodeled displacement terms. $\sigma_{\psi_i^m, \psi_j^m}^2$, $\sigma_{\psi_i^s, \psi_j^s}^2$ are the co-variances between two points at the same SAR images and are function of the distance between two points. $\sigma_{\psi_i^m, \psi_i^s}^2$, $\sigma_{\psi_j^m, \psi_j^s}^2$ are the co-variances between same points at the two SAR images and are correlation with coherence. $\sigma_{\psi_i^m, \psi_j^s}^2$, $\sigma_{\psi_j^m, \psi_i^s}^2$ the co-variances between two points at the two SAR images due to spatio-temporal correlation in unmodeled deformation.

2.3.4. Processing procedure

In this section, the processing procedure of time series InSAR is briefly introduced. Time series InSAR method is well-implemented technique, here a generic process flow is given. Fig. 2.10 is a flow diagram illustrating PSI processing.

The input of PSI is a stack of SAR images acquired for an area of interest. Interferogram stacks are generated following a baseline configuration. PS candidates are selected according to some criterion and then used to form a network of interconnected PS. The steps of point selection, network construction, phase unwrapping, and atmosphere estimation may be executed iteratively by selecting more PS pixels based on the first order estimation (van Leijen and Hanssen, 2004), or these steps could be executed iteratively by evaluating phase noise for re-selecting pixels (Hooper, 2008). The final result consists of height, displacement, and atmospheric phase screen estimation. Topography and displacement results are geolocated into map coordinates. DS-pixel based approaches have similar process flow. The study area and target deformation are the preconditions for the choice of PS-based or DS-based approach. In this research, the InSAR scatterers refer to PS or the pixels with point scattering mechanism.

2.3.5. Potential improvements

- **Functional model.** InSAR processing attempts to remove all phase contributions that can be predicted, such as the phase contribution due to the ellipsoidal shape of the Earth and the topographic phase (Hanssen, 2001). These phase terms are range and azimuth dependent and are typically calculated for the nominal center position of each pixel. Obviously, for point-like targets, the position of a dominant scatterer does generally not coincide with the central location of a particular pixel. As a result, the phase of those targets receives a biased correction, named as sub-pixel phase (Kampes, 2006). The sub-pixel phase term should be considered in the functional model of time series, which is discussed in chapter 3.

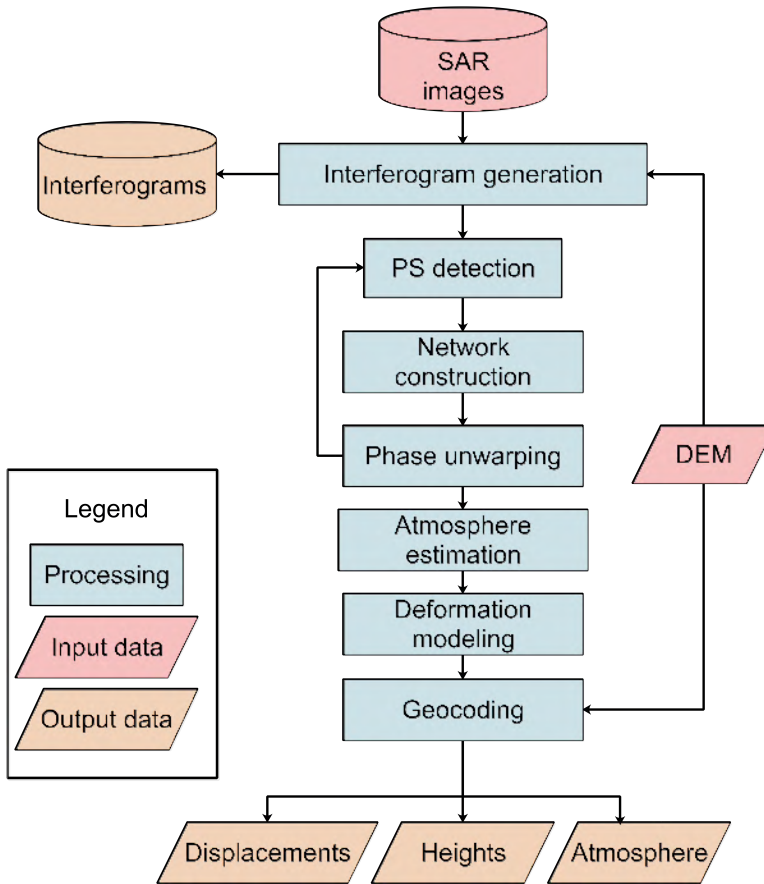


Figure 2.10: Generic processing flowchart of time series SAR interferometry analysis.

- Deformation model.** Since the displacement behavior is characterized by a linear model over time, when a pixel undergoes a complicated displacement, the displacement signal will be lost because of the predefined model. A significance test of multiple kinematic time series models has been proposed for choosing an optimal model (Chang and Hanssen, 2016). Moreover, an essential limitation is the data acquisition cycle of T . A sudden jump and resumed displacement between two acquisitions is undetected. Furthermore, the displacement phase larger than π between two acquisitions exceeds the maximum detected value. Thus, the maximum detected velocity v_{\max} in a linear model is $\frac{\lambda/4}{T/365.5}$ (Kampes, 2005; Jiang et al., 2011b).
- Coherent point selection.** The spatial sampling density of time series analysis is the density of selected point scatterers. Dense observational data can better describe the deformation phenomena. Currently, hybrid time series analysis tries to extract the displacements of both PS and DS pixels (Hooper, 2008; Samiei-Esfahany

et al., 2016).

- **Spatio-temporal filtering of the atmospheric phase component.** If the displacement is not correlated in time, the temporal high-pass filter would lead to a unmodeled displacement into the atmospheric signal. Meanwhile, the atmospheric signal that is temporally correlated would lead to the displacement signal. The performance of a temporal filter is worse at the start and end images. Hanssen (2001) suggested using the stochastic model to deal with the atmospheric signal.
- **Precise point positioning.** Detailed monitoring of a single target object in the built environment requires the precise point positioning of each point scatterer. The positioning precision of PS in a 3D datum is in the range of meters, particularly in the cross-range direction (Gernhardt et al., 2015; Dheenathayalan et al., 2016). This hampers the interpretation of InSAR results, particularly in a complex urban environment, as the PS is typically not exactly positioned on the object that is causing the reflection. To explore the full potential of PSI, PS point positioning must be optimized, which is the research goal of chapter 4 in this thesis.
- **Physical scattering mechanism understanding of InSAR scatterer.** Even with the precise point positioning, the measured point scatterers lack the direct link to the object in the real world. The point scatterers are not the benchmarks that are pre-defined prior to the measurements. These points are unlike the benchmarks in the leveling and GNSS. Understanding the scattering mechanism of InSAR scatterer facilitates the application of time series technique, which is our research goal of chapter 5.

2.4. Summary

In this chapter, we reviewed the data characteristics of SAR data providing a description of amplitude and phase data in SAR images. We introduced InSAR and time series InSAR techniques from the aspect of the observable, key processing steps in the algorithm, a general processing chain, and discussed some of the limitations. We summarized the traits of the main time series methods with baseline configuration, point selection criterion, and the deformation model. Although this technique has been widely used, there are some potential improvements for further optimization of this technique. The following chapters deal with the sub-pixel phase component in the functional model, the accuracy of 3D point positioning, and the physical understanding of point scatterers.

3

Sub-pixel persistent scatterer interferometry

In chapter 1, we have indicated that a dominant scatterer is located somewhere within the geometric bounds of a pixel, or a resolution cell. This sub-pixel position needs to be accounted for, as it may affect both the position as well as the displacement estimates of the measurement point. We assess the influence of the sub-pixel position on PSI positioning and displacement estimates, and evaluate the conditions under which a sub-pixel correction needs to be applied.

Section 3.1 gives the background of sub-pixel correction in InSAR processing. In Section 3.2, we investigate the effect of the sub-pixel phase on PSI results. PSI with sub-pixel correction has been implemented for evaluating its influences in Section 3.3. The analysis has been tested on stacks of TerraSAR-X, Radarsat-2, and Sentinel-1 images, see Section 3.4. The influence of sub-pixel correction was demonstrated by comparing the displacement and topography results by SP-PSI to the results by PSI in secs. 3.5 and 3.6. We discuss the necessity of sub-pixel correction in Section 3.7. Section 3.8 provides the conclusions of this chapter.

3.1. Introduction

Synthetic aperture radar interferometry (InSAR), in particular the family of techniques developed to analyze interferometric time series (stacks), has evolved into a geodetic tool for mapping the topography or displacement of the Earth's surface or objects on it. One of the most successful approaches is persistent scatterer interferometry (PSI), in which the phase of pixels corresponding to coherent scatterers over time is exploited (Ferretti et al., 2001; Crosetto et al., 2016). InSAR processing typically attempts to remove all phase contributions that can be predicted, such as the phase contribution due to the ellipsoidal shape of the Earth and the topographic phase (Hanssen, 2001). These phase

This chapter has been published in *ISPRS Journal of Photogrammetry and Remote Sensing* ((Yang et al., 2020).)

terms are range and azimuth dependent and are typically calculated for the nominal center position of each pixel. Yet, for point-like targets, the position of a dominant scatterer does not necessarily coincide with the center position of the pixel. As a result, the phase of those targets receives a biased correction.

In this study, the phase contribution due to the sub-pixel position of a dominant scatterer is referred to as the sub-pixel phase. Clearly, the better we can perform the phase correction, the more accurate the estimated parameters will be. Correcting the sub-pixel phase has been suggested by Kampes (2006). Hooper (2006) showed that the phase due to the range position of a dominant scatterer is especially important for height estimation when only a few (<12) interferograms are available. Using corner reflectors, Marinkovic et al. (2004, 2008) reported errors of 3.8 and 0.7 mm in displacement phase observations for ERS-2 and Envisat, respectively. However, currently there is no systematic analysis of the generic impact and significance of the sub-pixel position on the final PSI results, specifically considering the consequences for the precision of PS localization and the quality of the estimated displacements.

We assess the influence of the sub-pixel position on PSI positioning and displacement estimates, and evaluate the conditions under which a sub-pixel correction needs to be applied. A method is presented to find the exact phase center of the dominant scattering object within the resolution cell and to mitigate the influence of residual scattering elements. The impact of sub-pixel correction is discussed by comparing the results of PSI with and without sub-pixel correction.

3.2. Sub-pixel phase and its influence on PSI results

The observed phase ϕ_i^{ms} of pixel i in an interferogram from SAR images m and s is composed of:

$$\phi_i^{ms} = -2\pi a + \phi_{i,\text{ref}} + \phi_{i,\text{topo}} + \phi_{i,\text{disp}} + \phi_{i,\text{atmo}} + \phi_{i,\text{noise}}, \quad (3.1)$$

where a is the integer phase ambiguity, $\phi_{i,\text{ref}}$ is the reference phase corresponding to the ellipsoid, $\phi_{i,\text{topo}}$ is the topographic phase, $\phi_{i,\text{disp}}$ is the displacement phase, $\phi_{i,\text{atmo}}$ is the atmospheric phase, and $\phi_{i,\text{noise}}$ is the noise term.

The reference phase is calculated with an ellipsoid model and the topographic phase is calculated with an external DEM. Typically, both components are evaluated at the early-azimuth, near range corner of the pixel. However, the effective phase center can be situated at any arbitrary position ξ_i in azimuth and η_i in ground-range from the corner (l_i, p_i) , see Fig. 3.1. Thus, the components $\phi_{i,\text{topo}}^{l_i,p_i}$ and $\phi_{i,\text{ref}}^{l_i,p_i}$ omit the contribution due to the sub-pixel position within the pixel, resulting in a phase bias $\phi_{i,\text{sub}}$,

$$\phi_i^{ms} - \phi_{i,\text{ref}}^{l_i,p_i} - \phi_{i,\text{topo}}^{l_i,p_i} = -2\pi a + \phi_{i,\text{disp}} + \phi_{i,\text{atmo}} + \phi_{i,\text{noise}} + \phi_{i,\text{sub}}. \quad (3.2)$$

3.2.1. Sub-pixel position phase

The sub-pixel phase is due to the uncompensated reference and topographic phase. The sub-pixel phase can be written as

$$\phi_{i,\text{sub}} = \phi_{i,\xi} + \phi_{i,\eta} + \phi_{i,\Delta h_i}, \quad (3.3)$$

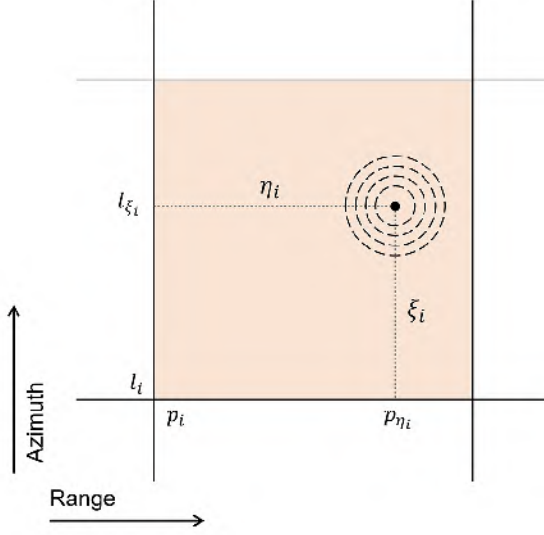


Figure 3.1: The effective scattering center within a image pixel is shifted ξ_i in azimuth and η_i in range from the near-range, early azimuth corner (l_i, p_i) .

where $\phi_{i,\xi}$ and $\phi_{i,\eta}$ are the uncompensated reference phases dependent on the azimuth ξ_i and ground-range η_i sub-pixel position, and $\phi_{i,\Delta h_i}$ is the uncompensated DEM phase due to the elevation difference Δh_i between (l_{ξ_i}, p_{η_i}) and (l_i, p_i) . These terms will be discussed subsequently.

Azimuth. Using the far-field approximation (Zebker and Goldstein, 1986; Hanssen, 2001), the azimuth phase term is given as (Kampes, 2006)

$$\phi_{i,\xi} = \frac{-4\pi}{\lambda} \cdot (\sin \vartheta^m - \sin \vartheta^s) \cdot \xi_i, \quad (3.4)$$

where λ is the wavelength, and ϑ^m and ϑ^s are the squint angles of the master and slave image, respectively. Fig. 3.2a illustrates the geometry for the additional phase due to the azimuth sub-pixel position ξ_i . Given the relation between the squint angle and the Doppler centroid frequency (Bamler and Schättler, 1993),

$$f_{DC} = \frac{-2v}{\lambda} \cdot \sin \vartheta, \quad (3.5)$$

where f_{DC} is the Doppler centroid frequency and v is the velocity of the satellite, Eq. (3.4) can be rewritten as (Kampes, 2006)

$$\phi_{i,\xi} = \frac{2\pi}{v} \cdot (f_{DC}^m - f_{DC}^s) \cdot \xi_i. \quad (3.6)$$

Hence, the azimuth sub-pixel phase term is related to the difference in the Doppler centroid frequencies. If there were a linear drift in the Doppler centroid, this signal would cause an apparent constant displacement rate. Fig 3.2b shows the azimuth phase

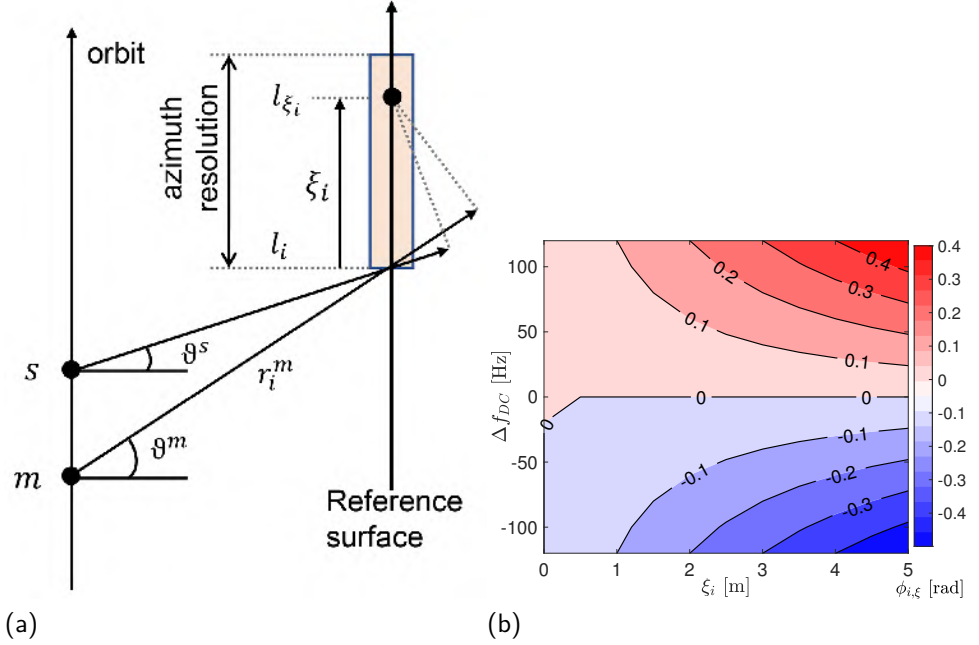


Figure 3.2: (a) Phase term due to the azimuth sub-pixel position ξ_i . The signal path length changes because of the variation in squint angle θ , resulting in a phase term $\phi_{i,\xi}$. Adapted from Marinkovic et al. (2004). (b) Sub-pixel phase term in azimuth as a function of the dominant scatterer location and Δf_{DC} in case of Radarsat-2.

term as a function of scatterer sub-pixel position in azimuth and differences in Doppler centroid values $\Delta f_{DC} = f_{DC}^m - f_{DC}^s$, in case of Radarsat-2 ($\lambda = 5.6$ cm, $\theta = 35^\circ$, $v = 7550$ m/s). The horizontal axis shows the sub-pixel position in azimuth within a resolution cell ξ_i . The vertical axis shows the differences in Doppler centroid values Δf_{DC} . The azimuth sub-pixel phase term is calculated with ξ_i and Δf_{DC} as Eq. (3.6), and indicated with the color. The phase term is proportional to increasing values of ξ_i and Δf_{DC} . If $\xi_i = 4.9$ m, the sub-pixel phase shift is 4 mrad/Hz ($0.2^\circ/\text{Hz}$) per Hz Doppler centroid difference.

Range. The ground-range sub-pixel phase term is (Kampes, 2006)

$$\phi_{i,\eta} = \frac{-4\pi}{\lambda} \cdot (\sin\theta^m - \sin\theta^s) \cdot \eta_i, \quad (3.7)$$

where θ^m and θ^s are the incidence angles of master and slave. The phase term can be rewritten using $\theta^m - \theta^s \approx B_\perp / r_i^m$ as

$$\phi_{i,\eta} = \frac{4\pi}{\lambda} \cdot \frac{B_\perp}{r_i^m} \cdot \cos\theta^m \cdot \eta_i, \quad (3.8)$$

where B_\perp is the perpendicular baseline between master and slave, and r_i^m is the range to the master antenna.

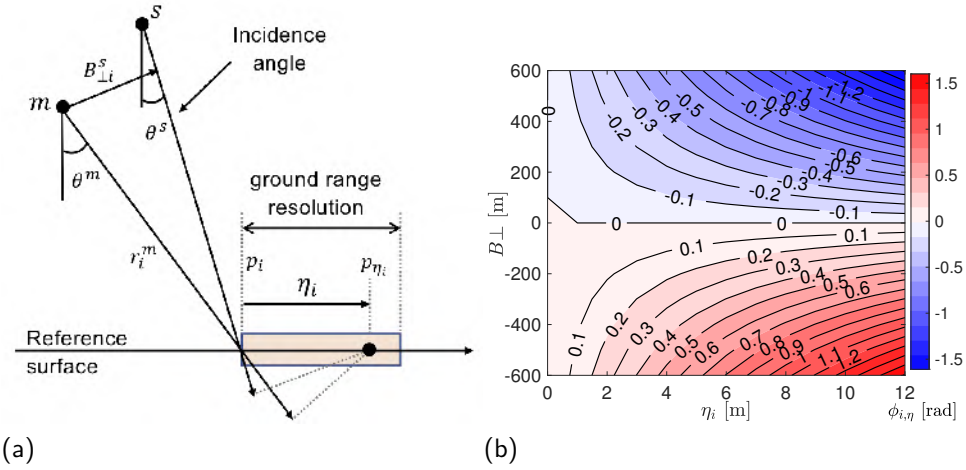


Figure 3.3: (a) Phase term due to the ground-range sub-pixel position η_i . The signal path length changes because of the variation in incidence angle θ , resulting in a phase term $\phi_{i,\eta}$. Adapted from Marinkovic et al. (2004). (b) Sub-pixel phase term in range as a function of the dominant scatterer location and B_{\perp} in case of Radarsat-2.

The ground-range sub-pixel phase term is equal to the reference phase variation due to the incidence angle under the far field approximation, see Appendix A. Fig. 3.3a shows the phase term due to the ground-range sub-pixel position. Fig. 3.3b gives the range phase in case of Radarsat-2 data as a function of scatterer position and perpendicular baseline. The horizontal axis is the sub-pixel position in ground range within a resolution cell η_i . The vertical axis is the perpendicular baseline values of B_{\perp} . The phase term is calculated with η_i and B_{\perp} as Eq. (3.8), and plotted in color. The phase term is proportional to increasing values of η_i and B_{\perp} . If $\eta_i = 11.8$ m, a B_{\perp} of 100 m will cause -0.26 rad (-15°) phase shift.

Elevation. The residual height term is

$$\phi_{i,\Delta h_i} = \frac{-4\pi}{\lambda} \cdot \frac{B_{\perp}}{r_i^m \sin \theta^m} \cdot \Delta h_i. \tag{3.9}$$

This term depends on the difference Δh_i between the DEM-height for the early-azimuth, near-range pixel corner and the DEM-height for the position of the scatterer. However, as standard PSI processing already includes the estimation of ‘DEM-errors’, relative to the reference DEM, the influence of the sub-pixel height is already compensated.

3.2.2. Influence on geolocation accuracy

In the slant-range and azimuth radar coordinate system, the location of a scatterer can be anywhere within the pixel. Thus, the maximum deviation (or absolute error) of a scatterer is equal to the pixel size, both in range and azimuth direction. For Sentinel-1 IW data with an incidence angle of 37 degrees, e.g., the geolocation error can be up to 4 m in ground-range and 14 m in azimuth.

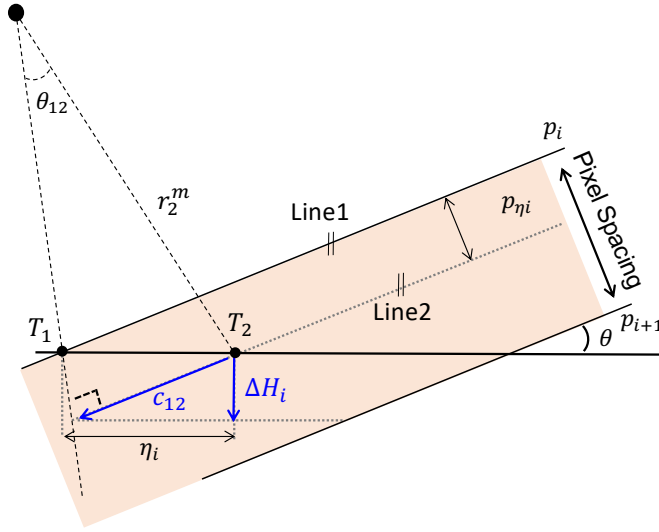


Figure 3.4: The uncompensated reference phase at the near-range side of the pixel T_1 causes a height error ΔH_i .

However, in the zero-Doppler plane, the geolocation error is not only dependent on the sub-pixel position η_i in the ground-range but also on the vertical position within the range bin. The vertical position is described by the height difference relative to a reference height and is estimated from phase observation. The position of a target is determined by combining range distance and phase using Range-Doppler-Ellipsoid/DEM equations (Schreier, 1993).

As described in Section 3.2.1, InSAR removes the phase components that can be predicted. Fig. 3.4 shows a range bin in the zero-Doppler plane, where a height error is caused by uncompensated reference phase. A point target within this range bin would be aligned to the near-range side of the pixel, i.e., line 1. If the height of the target is zero, the point is located at T_1 . Estimating the sub-pixel position by oversampling the data yields a slant-range shift of p_{η_i} . This implies that line 1 is translated to line 2, which changes the horizontal position to T_2 . Thus, the reference phase component should be evaluated at position T_2 . If the reference phase is calculated at the near-range side of the pixel (T_1) then part of the reference phase is not removed, i.e., the reference phase difference between the two positions.

The residual reference phase is (Hanssen, 2001)

$$\Delta\phi_{12,\text{ref}} = \frac{4\pi}{\lambda} \cdot B_{\perp} \cdot \theta_{12}, \quad (3.10)$$

where θ_{12} is the incidence angle difference between position T_1 and T_2 . The reference phase is linearly dependent on the perpendicular baseline B_{\perp} . In PSI analysis, this phase component would typically be adsorbed by the topographic phase estimation. Hence,

the residual reference phase results in a height error

$$\Delta H_i = -\sin\theta^m r_i^m \theta_{12}. \quad (3.11)$$

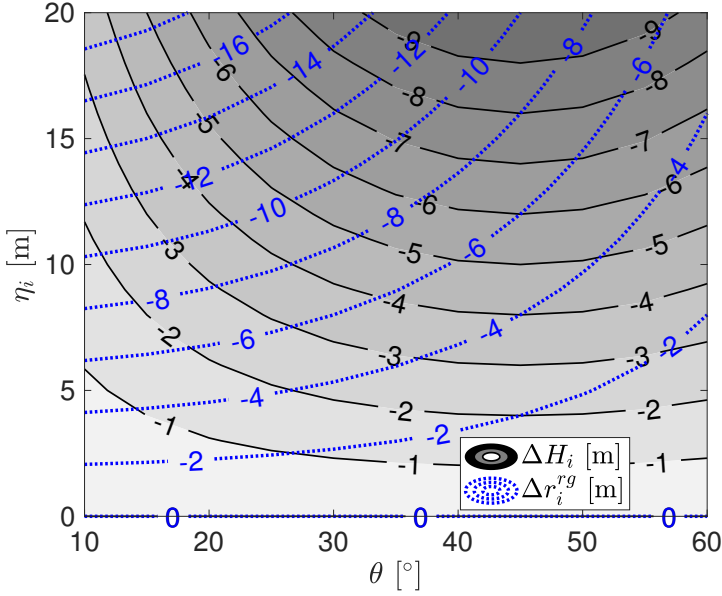


Figure 3.5: Height error ΔH_i and ground range error Δr_i^{rg} as function of range sub-pixel position η_i and incidence angle θ , in the case of Radarsat-2 data.

Since the cross-range distance c_{12} between T_1 and T_2 is

$$c_{12} \approx r_i^m \theta_{12} = \eta_i \cos\theta^m, \quad (3.12)$$

see Fig. 3.4, the height error thus be then written as (van Leijen, 2014)

$$\Delta H_i = -\eta_i \sin\theta_m \cos\theta^m. \quad (3.13)$$

Fig. 3.5 illustrates this height error ΔH_i as a function of the sub-pixel location and the incidence angle, in the case of Radarsat-2 data. For a ground range spacing of about 21 m, and a local incidence angle of 34° , this will cause a height error of -9.8 m.

The relation between the horizontal shift (ground range distance) and the height error is (van Leijen, 2014)

$$\Delta r_i^{\text{rg}} = \frac{\Delta H_i^{(2)}}{\tan\theta^m}. \quad (3.14)$$

Combining (3.13) and (3.14), the subsequent error in ground-range is given by

$$\Delta r_i^{\text{rg}} = -\cos^2\theta^m \eta_i. \quad (3.15)$$

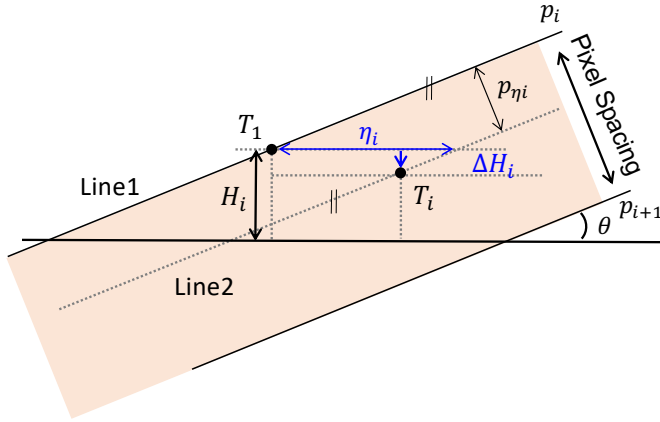


Figure 3.6: Influence of the sub-pixel position of a dominant scatterer in the zero-Doppler plane on geolocalisation. Without sub-pixel correction, the true position, T_i , is georeferenced to position T_1 . Applying sub-pixel correction, the location shifts to position T_i .

We visualized the ground-range error as a function of the incidence angle and the sub-pixel location in Fig. 3.5. The errors decrease for increasing incidence angles in a side looking system, similar to the effect of foreshortening.

Therefore, without sub-pixel correction, the geolocation error is a combination of the sub-pixel position p_{η_i} and the ΔH_i due to the residual reference phase. In Fig. 3.6, depicting a range bin in the zero-Doppler plane, a point target at T_i would by default be considered to be located at the near-range side of the pixel along the line 1. Considering the ellipsoid as a reference, the scatterer would be positioned at location T_1 with height H_i . After correcting the sub-pixel position p_{η_i} and the ΔH_i due to the residual reference phase, the location shifts to position T_i .

3.2.3. Influence on displacement estimation

Several deformation models can be used for estimating deformation in PSI processing. The simplest one is the steady-state (constant velocity) linear displacement model (Ferretti et al., 2001; Crosetto et al., 2016). Assuming a steady-state model, any temporal drift in Δf_{DC} , in combination with an azimuth sub-pixel position, can be misinterpreted as a bias in the displacement velocity estimate. Range sub-pixel positions in combination with any distribution of perpendicular baselines will result in a height estimation error.

In most cases, in particular when the time-series are long enough, the Doppler offsets seem to be independent of time. Thus, even without the sub-pixel correction, the corresponding phase term is not likely to affect the final displacement velocity estimates. However, if a temporal drift in Δf_{DC} cannot be excluded, applying the correction would improve the displacement velocity estimate.

Aside from correcting systematic phase terms, sub-pixel processing will generally result in an improved amplitude estimation, hence a better signal-to-clutter ratio, as values are closer to the true position of the dominant target.

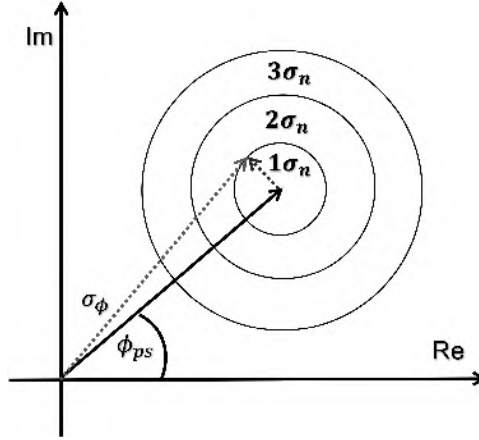


Figure 3.7: A phasor for a PS pixel, the phase of dominant object is ϕ_{ps} with a standard deviation of σ_n , resulting $\sigma_{\phi,i}$.

The contribution of clutter could be described by the phase standard deviation $\sigma_{\phi,i}$. It is noise part of deformation estimation, a relation between the $\sigma_{\phi,i}$ and Signal to Clutter SCR and is (Dheenathayalan et al., 2017)

$$\sigma_{\phi} \approx \sqrt{\frac{2}{2SCR - \sqrt{3}/\pi}}. \quad (3.16)$$

Thus, the phase error by clutter can be converted to the estimated displacement in LOS direction:

$$\sigma_{d_i}^{LOS} = \frac{\lambda}{4\pi} \sigma_{\phi,i}. \quad (3.17)$$

As stated in the begin of Section 3.2.1, the goal of PSI is separating the deformation signal, see Eq. (3.1). Thus, correcting the azimuth sub-pixel phase contribution and eliminating the phase contribution of clutter could suppress the noise term in phase isolation.

A non-zero sub-pixel position, in combination with DEM errors and time-dependent variation in the perpendicular baseline or Doppler centroid frequency will affect the observed phase values. Consequently, it is difficult to estimate the sub-pixel phase component directly from the observed phase. As an alternative, we can estimate the sub-pixel position of the dominant scatterer from the amplitude data, and subsequently apply the corresponding phase correction.

3.3. Methodology

As it is not feasible to estimate the sub-pixel phase term directly from the phase observations, we localize the position of the dominant scatterer based on amplitude information and subsequently correct the phase term related to the sub-pixel position in the interferometric phase. This processing method is referred to as sub-pixel PSI (SP-PSI).

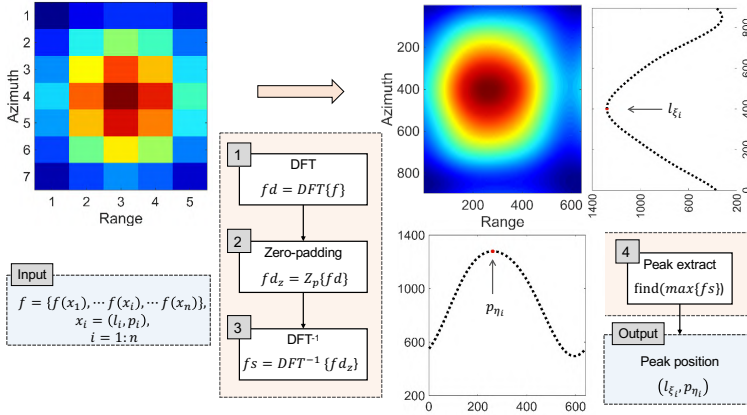


Figure 3.8: Position of the dominant scatterer detected based on amplitude information by FFT oversampling. Left: original amplitude image. Right: the oversampled image. The effective scattering center is found at the local maximum.

3.3.1. Dominant scatterer localization

Here we estimate the sub-pixel location straightforwardly by up-sampling the single-look-complex data in a small region around each scatterer and determining the position of the intensity-peak. This upsampling can be done in several ways (Keys, 1981; Parker et al., 1983; Quegan, 1990; Hanssen and Bamler, 1999; Perissin, 2006; Shi et al., 2015; Zhang and López-Dekker, 2019). In our case we use a sinc-interpolation (Cumming and Wong, 2005b; Gonzalez and Woods, 2007) which is implemented efficiently in the frequency domain. This implies a Discrete Fourier Transform (DFT) of the block, a zero padding operation, and an inverse DFT. Fig. 3.8 visualizes the procedure. The input is the data block around pixel (l_i, p_i) . The effective scattering phase center (l_{ξ_i}, p_{η_i}) is detected by finding the maximum peak of the interpolated signal.

The variance of estimated peak position i in azimuth $\sigma_{l,i}^2$ and range $\sigma_{p,i}^2$ direction is given by (Bamler and Eineder, 2005)

$$\sigma_{l,i}^2 = \sigma_{p,i}^2 = \frac{3}{2 \cdot \pi^2 \cdot \text{SCR}_i}, \quad (3.18)$$

where SCR is the signal-to-clutter ratio of a point. Eq. (3.18) is the Cramér-Rao bound for a change of the peak due to clutter (Stein, 1981; Bamler and Eineder, 2005), under the assumption of a homogeneous area and circularly Gaussian clutter. After determining the sub-pixel position of the dominant scatterer, the corresponding reference phases are computed and compensated.

3.3.2. Sub-pixel correction processing chain

To analyze the influence of the sub-pixel correction, a sub-pixel correction module is designed and embedded in the Delft Persistent Scatterer Interferometry (DePSI) toolbox (Kampes, 2006; van Leijen, 2014), see Fig. 3.9. It includes localizing the sub-pixel position of the scattering center and correcting the corresponding phase terms ϕ_i^{ms} .

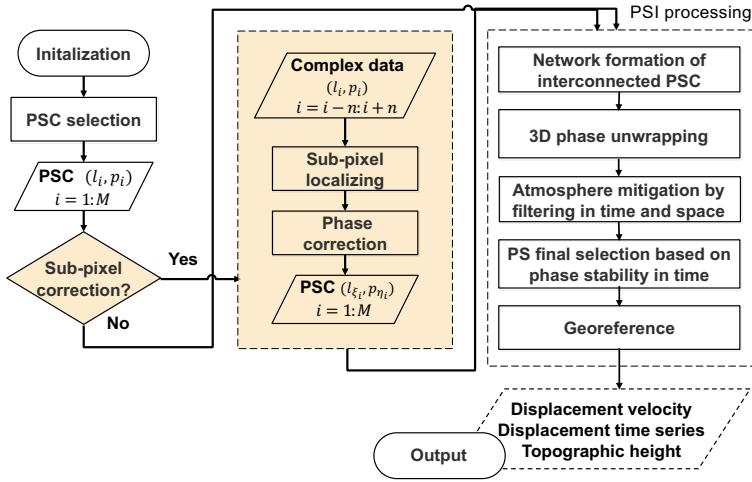


Figure 3.9: Processing chart of PSI with dominant scatterer localisation. The dominant scatterer module is implemented on DePSI. The processing flow of the other modules of DePSI is simplified here.

PS Candidates (PSC) are selected based on their normalized amplitude dispersion. The sub-pixel correction is performed for each selected PSC (l_i, p_i) , where $i = 1 : M$, and M is the number of PSCs. For each PSC, we use an $n \times n$ complex data block centered at the PSC position and estimate the peak position and the corrected phase ϕ_i^{ms} . After determining the sub-pixel position, (3.3) is applied to determine the phase correction term, which is subtracted from the phase of the original PSC.

After the sub-pixel correction a standard PSI processing flow is applied, including network construction, spatio-temporal (3D) phase unwrapping, atmospheric phase mitigation, final PS selection, and geo-coding. The results presented were obtained using DePSI (Kampes, 2006; van Leijen, 2014). In-depth discussions of PSI processing can be found in Ferretti et al. (2001); Hooper (2006); Kampes (2006); van Leijen (2014); Crosetto et al. (2016).

The steps of network construction, phase unwrapping, and atmosphere mitigation were executed iteratively after PS selection. The PS were re-selected based on the deviation of the unwrapped phase time-series of each PS from a pre-defined deformation model. When the standard deviation of the residual phase of the PS exceeds a certain threshold, the PS is discarded because the corresponding estimation is assumed to be unreliable. It is worth pointing out that this procedure will also eliminate high quality PS that do not follow the selected model (Chang and Hanssen, 2016). As this is not a SP-PSI specific issue, the comparison of performances remains valid. Here, we set the number of iterations to five.

3.4. Experiment setting

In order to analyze the influence of sub-pixel correction on PSI results, we analyzed three data stacks with different resolutions, acquired by TerraSAR-X, Radarsat-2, and Sentinel-

1. For our analysis we consider an area around Delft, the Netherlands.

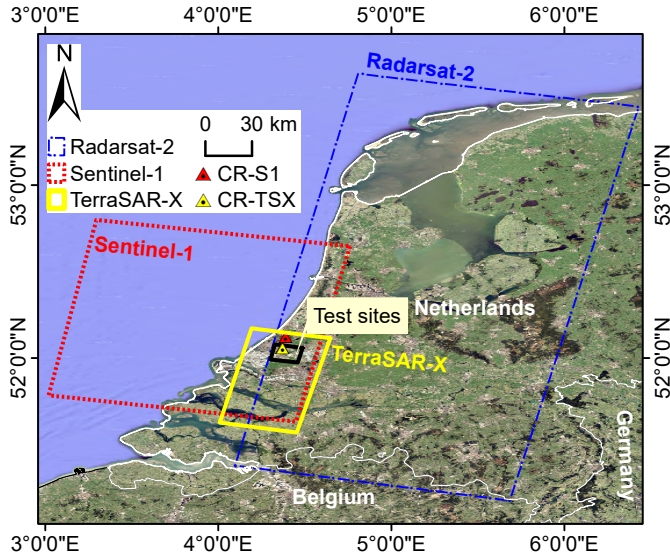


Figure 3.10: The coverage of TerraSAR-X, Radarsat-2, and Sentinel-1 data. Triangles indicate the location of corner reflectors installed for TerraSAR-X and Sentinel-1.

Fig. 3.10 shows the location of the test area, the bounding polygons of the data stacks, and the location of the installed reflectors. The relevant parameters of the data stacks are provided in Tab. 3.1. The perpendicular baselines and Doppler centroid differences have a considerably larger spread in the Radarsat-2 case. Meanwhile, there is a relatively long time series of Radarsat-2 data, covering about five years.

Seven reflectors, CR1–CR7, were installed at the Ypenburg test site between August 2012 and March 2014 with an orientation optimized for the TerraSAR-X acquisitions. Fig. 3.11a shows those reflectors in the mean intensity image of 46 TerraSAR-X images. We use CR4–7 in our analysis to avoid the impact of the mutual side-lobes of the first three.

For our analysis of the Sentinel-1 stack, we used two reflectors installed at the Wasseenaar test site since November 2017, see Fig. 3.11b. Differential GNSS and tachymetry are used to precisely determine the apex positions of these CRs. These positions are determined with a precision of 1 cm (1σ) in the horizontal dimensions (east and north), and 2 cm in the vertical direction.

3.5. Displacements Estimation

Fig. 3.12a shows the estimated displacement velocities for the PS identified in the TerraSAR-X data stack by SP-PSI, i.e., PSI with sub-pixel correction. Fig. 3.12b shows the velocity differences between PSI and SP-PSI. Similarly, the estimated velocities and the velocity differences of Radarsat-2 and Sentinel-1 data stacks are given in Figs. 3.13 and 3.14, respectively.

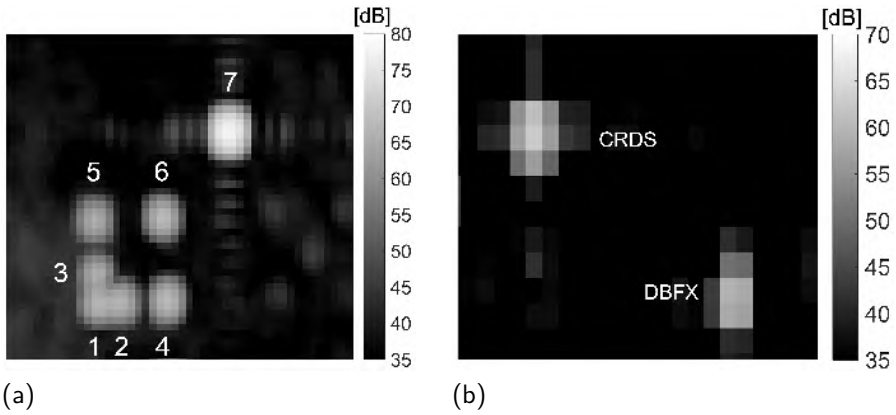


Figure 3.11: (a) Mean intensity image from 46 TerraSAR-X images covering the seven corner reflectors, (b) Mean intensity image from 40 Sentinel-1 images covering the two reflectors.

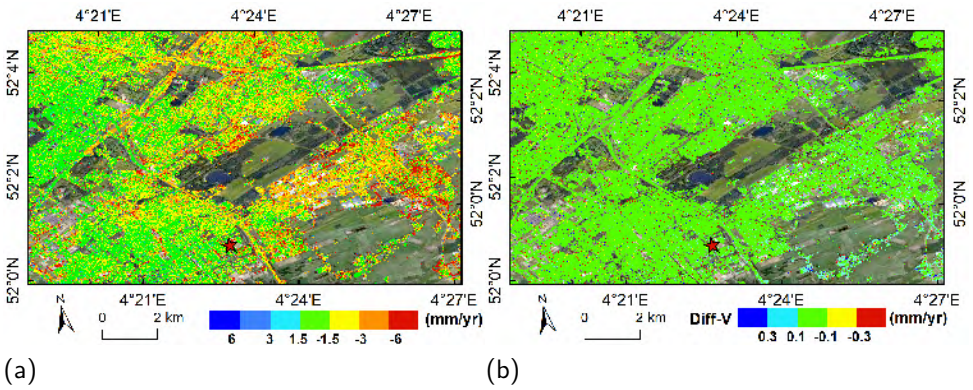


Figure 3.12: (a) Estimated linear velocities by SP-PSI for the TerraSAR-X stack. The reference point is indicated by the red star. (b) Differences in the estimated velocity between PSI with sub-pixel correction and PSI.

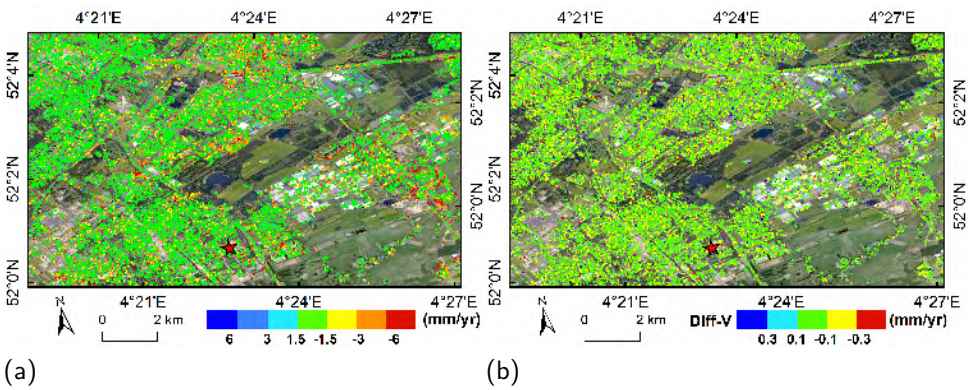


Figure 3.13: (a) Estimated linear velocities by SP-PSI for the Radarsat-2 stack. The reference point is indicated by the red star. (b) Differences in the estimated velocity between PSI with sub-pixel correction and PSI.

Table 3.1: TerraSAR-X, Radarsat-2, and Sentinel-1 SAR data characteristics

Mission/Parameter	TerraSAR-X	Radarsat-2	Sentinel-1
Track	T048	T202	T110
Band	X	C	C
Start Date	2012.08.11	2010.06.20	2017.11.08
End Date	2014.03.06	2015.02.18	2018.07.18
Number of images	46	64	40
B_{\perp} [min/max] [m]	-382/142	-576/317.7	-88.4/117.7
Δf_{DC} [min/max] [Hz]	-78.9/70.8	-103.2/122.8	-17.7/73.3
Acquisition mode	Stripmap	Standard	IW
Pass direction	Descending	Descending	Descending
Polarization	HH	HH	VV
Incidence angle [°]	22.3 – 25.6	30.6 – 37.1	35.7 – 41.7
Heading [°]	192.2	191	190
Range sampling [m]	0.9	11.8	2.3
Azimuth sampling [m]	1.7	4.9	13.8
Range Bandw. [MHz]	150	11.6	56.5
Azimuth Bandw. [Hz]	2765	900	327

Very similar displacement signals are observed in the three stacks, despite the fact that the stacks cover different time spans. This indicates that the majority of the points follow a constant displacement (subsidence) velocity sustained in time.

The velocity differences between PSI and SP-PSI at most points vary between -0.3 and $+0.3$ mm/y. The velocity differences are spatially random and their magnitude are very small, with the TerraSAR-X results having the smallest difference. The mean and standard deviation of the velocity differences are 0.0 ± 0.1 , -0.1 ± 0.1 , and 0.1 ± 0.2 mm/y for TerraSAR-X, Radarsat-2, and Sentinel-1, respectively.

Fig. 3.15 shows the histograms of the differences in estimated velocities. Compared to TerraSAR-X and Radarsat-2, a larger spread of velocity differences was observed in the case of Sentinel-1, which can be explained by the shorter time series of Sentinel-1, which results in more influence of noise.

Table 3.2: Quality indicators of TerraSAR-X, Radarsat-2, and Sentinel-1 data-stacks results by PSI and PS-PSI.

		NP	σ_D [mm]	STC [mm]
			mean	mean
TSX	PSI	288,287	0.27	1.81
	SP-PSI	290,768	0.26	1.80
RS2	PSI	51,041	0.53	3.70
	SP-PSI	51,436	0.53	3.67
S1	PSI	52,261	2.68	2.69
	SP-PSI	54,819	2.54	2.68

To further evaluate the results by PSI and SP-PSI, three indicators were used, see

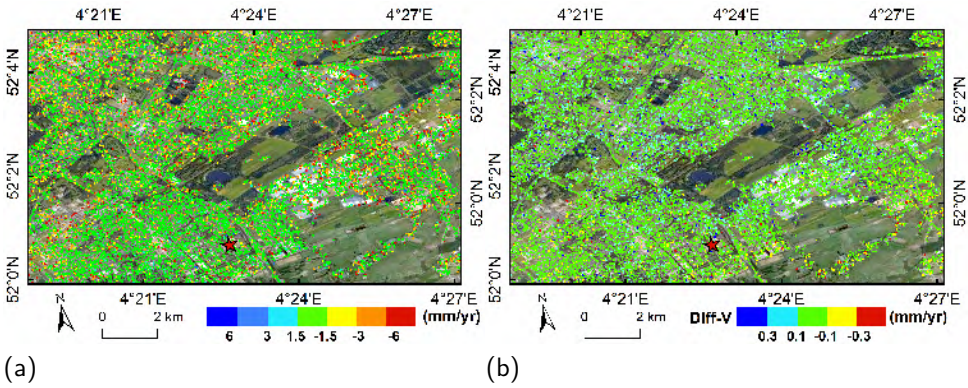


Figure 3.14: (a) Estimated linear velocities by SP-PSI for the Sentinel-1 stack. The reference point is indicate by the red star. (b) Differences in the estimated velocity between SP-PSI and PSI.

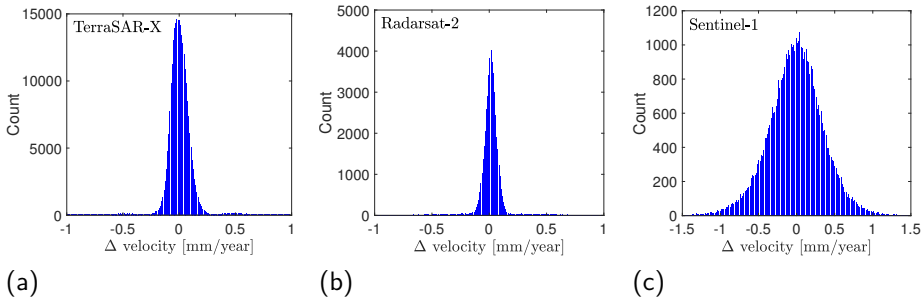


Figure 3.15: Histogram of differences in the estimated velocity between SP-PSI and PSI with (a) 46 TerraSAR-X images, (b) 64 Radarsat-2 images, and (c) 40 Sentinel-1 images.

Tab. 3.2: the number of accepted points (NP) after final selection; the standard deviation σ_D of the residuals between the displacement model and the displacement time series, and the Spatio-Temporal Consistency (STC), which expresses the minimum root mean square error of the double-differences between PS and various surrounding PS (van Leijen, 2014).

Tab. 3.2 reveals that the number of points improved by applying the sub-pixel correction, most notably for Sentinel-1, yielding 5% more points. All PS candidates were re-selected by evaluating the deviation of unwrapped time series from the deformation model, as introduced in Section 3.3. In this step, more points were preserved in the PSI results with sub-pixel correction. Applying sub-pixel correction relieves the phase terms related to Doppler offsets from the interferometric phase. The increasing number of points reflects the reduced phase noise with the sub-pixel correction. While the σ_D and STC improved slightly by applying the sub-pixel correction, all metrics show a consistent improvement after sub-pixel correction.

To clearly show the differences in time series displacement between PSI and SP-PSI results, we plotted displacement differences of 500 arbitrary PS per epoch in Fig. 3.16,

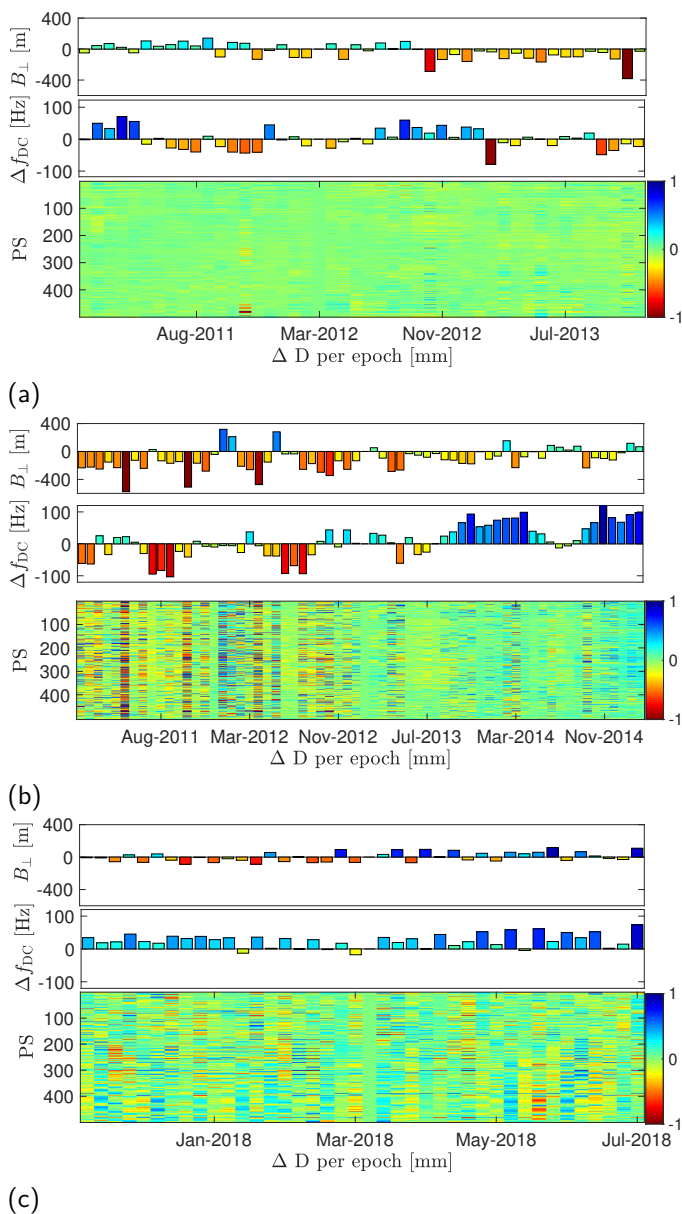


Figure 3.16: Differences between PSI and SP-PSI displacements (in mm) for 500 random scatterers, as a function of time, perpendicular baselines, and Doppler centroid differences. (a) 46 TerraSAR-X images, (b) 64 Radarsat-2 images, and (c) 40 Sentinel-1 images.

together with the perpendicular baselines and Doppler centroid differences of the three stacks. The differences in displacements per epoch ranged between -1 and 1 mm. For TerraSAR-X, almost no differences are observed between the results by PSI and SP-PSI. In the case of Radarsat-2, the largest differences were observed at epochs with a relatively long baseline. The displacement differences of Sentinel-1 are random showing no relation with the baselines or the Doppler offsets.

3.6. Geolocation precision

The PS point cloud was projected in the Dutch national reference system RD and vertical reference system NAP. The coordinate differences at all points measured by PSI and SP-PSI are summarized in Tab. 3.3.

Table 3.3: Coordinate differences (average and standard deviation) between PSI and SP-PSI [m] in the east (Δe), north (Δn), and up (Δu) direction of PS with TerraSAR-X, Radarsat-2, and Sentinel-1.

	TerraSAR-X	Radarsat-2	Sentinel-1
Δe	-0.42 ± 2.55	-1.56 ± 5.56	-0.86 ± 1.57
Δn	-0.11 ± 0.65	-0.48 ± 1.44	-3.12 ± 4.14
Δu	0.06 ± 1.18	-0.25 ± 3.92	-0.49 ± 0.59

As expected, the smallest average differences are observed for TerraSAR-X due to its fine resolution. The vertical differences correspond to the residual reference phase as discussed in Section 3.2.2, which is linear dependent on B_{\perp} . As the baseline of the Sentinel-1 stack is relatively shorter due to its constrained small orbital tube, the influence on the reference phase is small, and the standard deviation of vertical differences for Sentinel-1 are the smallest. Conversely, the largest differences were observed for Radarsat-2, which results in large shifts within the resolution cell and a larger height component due to the wide range of baselines.

The 3D positioning accuracy is further evaluated with the installed reflectors. The calculated positioning result by PSI is the relative measurement, as the cross-range distance of each PS in radar geometry is estimated from the interferometric pairs relative to a reference point (Yang et al., 2019b). Hence, the 3D point position of the reflectors calculated by PSI cannot be directly verified with the position measured by GNSS. The double-difference coordinates were used for the evaluation to avoid deviations from the reference point. The verification results show the relative positioning accuracy of PSI and the accuracy of distance measurements.

Using CR6 as the reference, we calculated the double-difference coordinates measured by PSI, SP-PSI, and GPS. Fig. 3.17 graphically compares the locations of CR4, CR5, and CR7 relative to CR6, by SP-PSI, and PSI, to the apex locations estimated by GNSS. The root mean square error (RMSE) of the double-differences coordinates relative to GNSS positions are given in Tab. 3.4.

There are distinct improvements in the cross-range direction, with a decreasing the RMSE of InSAR-GNSS from 4.00 m to 1.22 m with sub-pixel correction. As the TerraSAR-X data have a fine resolution, the improvement is small both in azimuth and range directions, about 0.2 m. In local coordinates, the improvement in cross-range not only con-

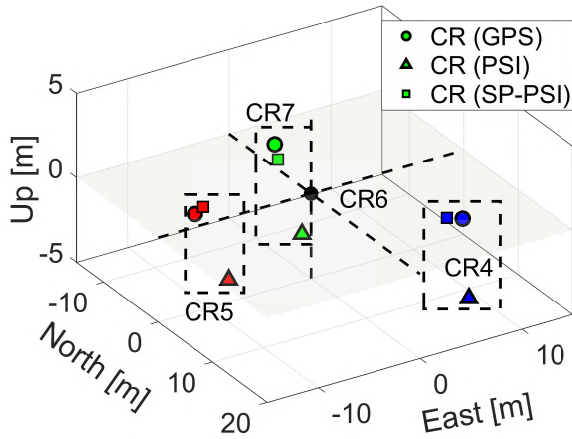


Figure 3.17: Location of CR4, CR5, and CR7 relative to CR6. The circles indicate the position of CR4, CR5, CR7 estimated by GNSS. The squares indicate the estimated position of the reflectors by SP-PSI with TerraSAR-X. The triangles indicate the estimated position of the reflectors by PSI.

Table 3.4: RMSE of double-difference coordinates by PSI and SP-PSI for TerraSAR-X with regard to GNSS measurement [m].

	PSI	SP-PSI		PSI	SP-PSI
Δa	1.84	1.60	Δe	3.80	1.04
Δr	0.50	0.35	Δn	2.27	1.46
Δc	4.00	1.22	Δu	1.63	0.50

verts to up-direction, but also to east and north directions. Fig. 3.17 demonstrates that the positions estimated by SP-PSI are closer to the actual (measured GNSS) locations.

The evaluation of PS measured by Sentinel-1 is given in Tab. 3.5. The RMSE in the azimuth direction has improved clearly due to the poorer azimuth resolution. This improvement propagates to the north direction. The improvement in cross-range is smaller than in the TerraSAR-X result, which is a result of the smaller range of cross-track baselines. Fig. 3.18 visualizes the location of DBFX concerning CRDS.

Table 3.5: RMSE in coordinate-differences of DBFX-CRDS in Sentinel-1 data stack by PSI and SP-PSI compared to GNSS measurement [m].

	PSI	SP-PSI		PSI	SP-PSI
Δa	7.48	3.60	Δe	7.81	5.40
Δr	1.78	1.20	Δn	6.14	2.63
Δc	4.30	3.43	Δu	2.57	2.04

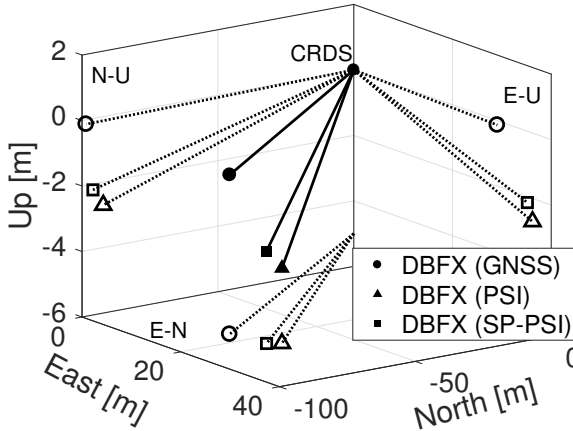


Figure 3.18: The location of DBFX with reference to CRDS. The dark dots indicates the apex position of DBFX measured by GNSS. The blue square indicates the estimated position of DBFX by sub-pixel PSI of sentinel-1 data stack. The red triangle indicates the estimated position of DBFX by PSI of sentinel-1 data stack. Points are projected into east-north, east-up, and north-up planes to illustrate their locations.

3.7. Necessity

This section provides a reference for assessing the necessity of sub-pixel correction. Sub-pixel correction is applicable to point-like targets, whose position is well defined. It is not relevant in the case of distributed scatterers. The sub-pixel correction is often neglected in PSI processing aimed at displacement applications. As presented in this study, the improvement in estimated velocities is marginal (the differences are smaller than 1 mm/y). Yet, the sub-pixel correction does enable more points to be selected.

For the positioning of the selected persistent scatterers, the improvement is significant and more relevant. The precise point positioning of individual scatterers needs the sub-pixel correction (Gernhardt et al., 2015; Yang et al., 2019b). Moreover, in applications relying on the precise positioning of individual scatterers sub-pixel correction should be applied. The consequences of sub-pixel correction are summarized in Tab. 3.6.

Table 3.6: Influence of sub-pixel position on PSI estimates.

	Sub-pixel position	
	azimuth	range
Displacement (per epoch)	No	No
Displacement velocity	iff Δf_{DC} drift	No
Height	No	Yes
Planar position	Yes	Yes

3.8. Conclusions

We show that the influence of the sub-pixel correction is significant for the geolocation of the scatterer (meter-level improvement), modest for the elevation estimation (centimeter-level improvement), and limited for the displacement estimation (submillimeter-level).

In theory, as long as baselines and Doppler offsets do not show a temporal trend, neglecting the sub-pixel correction should not impact the estimated velocities and displacements significantly. Conversely, any systematic trend in the baseline or the Doppler centroid will introduce a proportional trend in the displacement signal.

Working at the sub-pixel level results in a reduced phase noise, which in turn leads to an increased number of selected points. In the case of Sentinel-1, a 4% increase in the number of points was obtained. While this percentage is relatively small, it may amount to many thousands of extra points in the area of interest. Moreover, for specific deformation signals, having an improved spatial sampling of the area may change the likelihood of detection.

The main improvement resulting from sub-pixel PSI processing is the improved positioning of persistent scatterers. The largest differences were observed in the Radarsat-2 results, which is explained by the relatively low resolution and considerable baseline dispersion. GNSS measurements have validated the improvements using sub-pixel correction, which yields a maximum improvement for the TerraSAR-X result of 2.8 m in the east direction and for the Sentinel-1 result of about 4 m in the north direction.

Sub-pixel correction is essential for PSI applications where precise positioning is required, regardless of the data used. The effect of subpixel correction on deformation estimation is relatively limited and is most dominant for large orbital baselines and short time series. This correction applies to point-like targets, whose position is well defined, which is not relevant in the case of distributed scatterers.

4

Precise point positioning aided by corner reflectors and surface models

In chapter 3, we have demonstrated sub-pixel correction facilitating the accurate height and quality displacement estimation. However, affected by the system-related biases and unaccounted geophysical effects, the position of radar scatterers deviates from the true position, with errors ranging from centimeters to several meters. Correction of those errors is necessary for precise point positioning. The goal of this chapter is to improve the positioning precision of the InSAR point cloud.

The state of the art in geo-localization of InSAR scatterers is reviewed in Section 4.1. The following Section 4.2 presents the principles of scatterer geolocation and the corresponding geolocation error sources. The methods assisted by a corner reflector deployment were proposed in Section 4.3 and the approach assisted by a high-precision digital surface model was introduced in Section 4.4. These approaches were applied to TerraSAR-X and Sentinel-1 data, see the experimental configuration in Section 4.5 and the results in secs. 4.6.1 and 4.6.2. We discuss the influence of different types of DSMs on positioning precision in Section 4.6.3 A comparison of the corrections methods is given in Section 4.7 and conclusions are drawn in Section 4.8.

4.1. Introduction

PSI exploits coherent points—the persistent scatterers (PS) in time series of SAR images and estimates their differences in line-of-sight range over time. Together, these coherent points form a PS point cloud. Compared to the millimeter-level precision for the esti-

Parts of this chapter have been published in Proceedings of Living Planet Symposium 2016 ((Yang et al., 2016)) and *ISPRS Journal of Photogrammetry and Remote Sensing* ((Yang et al., 2019b).)

mated relative displacements, the positioning precision and accuracy of PS in a 3D datum is in the range of meters, particularly in the cross-range direction (Gernhardt et al., 2015; Dheenathayalan et al., 2016). This hampers the interpretation of the results, particularly in a complex urban environment, as the PS are typically not exactly positioned on the object that is causing the reflection. To explore the full potential of PSI, PS point positioning must be optimized.

Significant progress has been made in improving the 2D radar coordinate accuracy in an absolute sense, see Small et al. (2004); Schubert et al. (2010); Eineder et al. (2011); Cong et al. (2012); Schubert et al. (2015); Balss et al. (2018). These methods involve corrections of secondary positioning components including azimuth shifting, atmospheric path delay, plate motion, solid Earth tide, and polar motion, such methods can be collectively referred to as the geophysical method. Yet, while this improves the absolute range and azimuth position in *radar* coordinates, it does not yield an estimate for the cross-range position, which is essential for practical 3D *geographic* positioning.

Full 3D geometric fusion methods, see Gernhardt et al. (2012); Gisinger et al. (2015); Duque et al. (2016); Zhu et al. (2016); Montazeri et al. (2018), require the identification of physically identical scatterers visible in opposing imaging geometries, e.g., lamp posts, and are therefore strongly depending on such targets-of-opportunity (ToO). For medium/low-resolution SAR data, finding such ToO in opposite tracks is very difficult. Considering Sentinel-1 data, there are no reports yet in literature concerning the 3D positioning accuracy.

For (In)SAR, artificial ground control points (GCP) are typically corner reflectors (CR) or transponders. CRs are used for external radiometric calibration of SAR systems (van Zyl, 1990; Sarabandi and Chiu, 1996; Small et al., 2007; Shimada et al., 2009), deformation measurements in low coherence areas (Hanssen, 2001; Xia et al., 2002; Crosetto et al., 2016), accuracy assessment of InSAR measurements (Ferretti et al., 2007; Marinkovic et al., 2008; Garthwaite, 2017), and to calibrate sensor timing offsets (Small et al., 2004, 2007; Miranda et al., 2013).

CRs have a high and stable radar cross section (RCS), a well-defined scattering center (the apex), and are easily identified in the image. However, while precise geolocation with the aid of GCP is common in the field of photogrammetry, the value of 3D geolocation of entire PSI point clouds using GCP has not yet been discussed, to the authors' knowledge.

Ideally, the philosophy of remote sensing is to avoid installing GCP in the terrain, as it involves extra cost and effort for manufacturing, deployment, and maintenance. It requires physical access to the area, and it is very sensitive to disturbance. Moreover, it requires additional geodetic measurements to obtain ground truth in position and/or changes in position. Therefore, there is a strong incentive to find alternative methods to achieve the same objectives.

Here we assess the advantages of GCP, which alternatives are available, and how these compare to the use of installed GCP. Moreover, we review the strategy of deployment, i.e., what are the minimum requirements for the (i) number, (ii) the type, and (iii) the location of the GCP, (iv) the duration of deployment, (v) the conditions for the additional collocated geodetic measurements, (vi) the required effort in terms of cost and resources, and (vii) an evaluation with potential alternative approaches avoiding the GCP deployment,

such as using targets-of-opportunity.

A high-resolution Digital Surface Model (DSM) can also be counted as a target-of-opportunity, with thousands of virtual GCP, and may be a valid alternative for using artificial GCP.

4.2. Point scatterer geolocation

The geolocation process references a pixel in SAR geometry onto a geodetic datum. It describes the conversion of azimuth line and range pixel position of a scatterer in the 2D image to a 3D coordinate system (Schreier, 1993; Schwäbisch, 1995; Zhang et al., 2012). Given radar timing annotations, including the time of the first range sample, $t_{r,0}$, range sampling rate (RSR), first azimuth time, $t_{a,0}$, pulse repetition frequency (PRF) and the state vectors describing the trajectory of a satellite during the time of data acquisition, a point at position T on the Earth's surface can be located by solving the Range-Doppler-Ellipsoid/DEM equations (Schwäbisch, 1995).

Fig. 4.1 illustrates the positioning procedure from a scatterer T at (l_T, p_T) in the radar image to its corresponding position (x_T, y_T, z_T) in a 3D Terrestrial Reference Frame (TRF) realizing an Earth-Centered-Earth-Fixed (ECEF) reference system (Schreier, 1993; Schwäbisch, 1995).

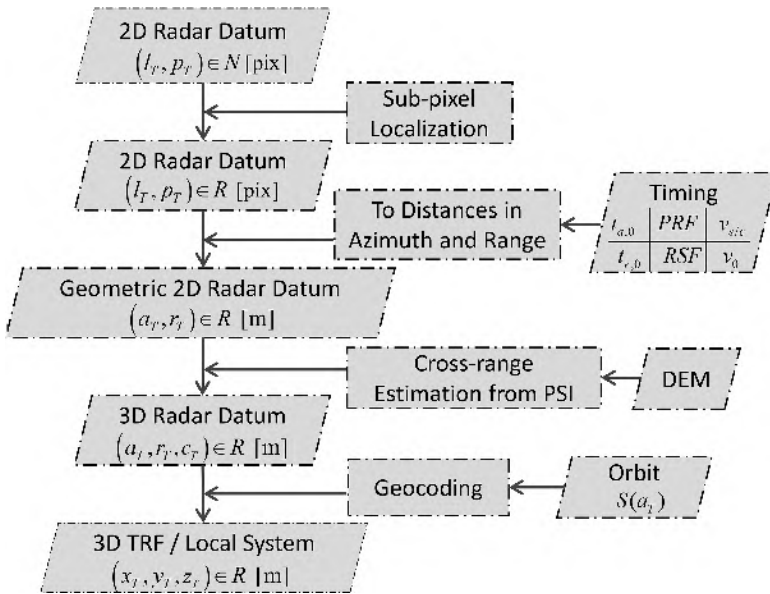


Figure 4.1: Methodology of point scatterer positioning from a 2D radar datum to a 3D Terrestrial Reference Frame (TRF)/local system.

The sub-pixel position of the effective phase center T within a resolution cell (l_T, p_T) is determined through sinc-interpolations. The variance of localization of a scatterer T

in azimuth $\sigma_{l_T}^2$ and range $\sigma_{p_T}^2$ direction is given by (Bamler and Eineder, 2005)

$$\sigma_{l_T}^2 = \sigma_{p_T}^2 = \frac{3}{2 \cdot \pi^2 \cdot \text{SCR}}, \quad (4.1)$$

where SCR is the Signal to Clutter Ratio of a point. Eq. (4.1) is the Cramer-Rao bound for a change of the peak due to clutter (Stein, 1981; Bamler and Eineder, 2005), under the assumption of homogeneous area and circularly Gaussian clutter.

The sub-pixel image position can be transformed to 2D geometric radar coordinates with the $t_{a,0}$, PRF, $t_{r,0}$, RSR, the velocity of spacecraft $v_{g/t}$, and the speed of light c_0 . The origin of the radar coordinate system is the phase center of the antenna. Azimuth distance a_T is expressed as

$$a_T = \int_{t_{a,0}}^{t_{a,0} + l_T \Delta t} v_{g/t}(t) dt \approx \bar{v}_{g/t} \cdot (t_{a,0} + l_T \Delta t), \quad (4.2)$$

where $\Delta t = \text{PRF}^{-1}$. Range-distance r_T is expressed as:

$$r_T = \frac{v_0}{2} \cdot (t_{r,0} + p_T \Delta \tau), \quad (4.3)$$

where $\Delta \tau = \text{RSR}^{-1}$.

The cross-range distance ('elevation') of a point is estimated from at least one interferometric SAR observation as

$$\hat{c}_T \approx c_0 + \frac{\lambda}{4\pi} \frac{r_T}{B_\perp} \hat{\phi}_T, \quad (4.4)$$

where λ is the wavelength, B_\perp is the perpendicular baseline of the interferometric pair, and $\hat{\phi}_T$ is the estimated unwrapped topographic phase relative to the reference point. c_0 is the cross-range (elevation) of a reference point, which is assumed to be known, see Section 4.3.2. Note that the assumption of a 'known' reference point position is rarely satisfied in practice.

The cross-range c_T together with azimuth a_T , and range r_T complements the 3D orthogonal radar coordinate system. The corresponding position of point scatterer T , with state vector $\mathbf{T} = [x_T, y_T, z_T]$ in a 3D TRF, is estimated using the Range-Doppler-Ellipsoid equations see Fig. 4.2.

For *range*, the geometric distance r_T from scatterer T to satellite $\mathbf{S}(t_a)$ is a function of the satellite state vectors and scatterer state vector,

$$\|\mathbf{S}(t_a) - \mathbf{T}\| - r_T^2 = 0, \quad (4.5)$$

where $\mathbf{S}(t_a)$ is the satellite state vectors at the zero Doppler time of imaging target $t_a = t_{a,0} + l_T \Delta t$.

For *Doppler*, the scatterer T is viewed perpendicular to the orbit, i.e.,

$$f_D(t_a) + \frac{2}{\lambda} \frac{(\mathbf{S}(t_a) - \mathbf{T})}{\|\mathbf{S}(t_a) - \mathbf{T}\|} \mathbf{V}(t_a) = 0, \quad (4.6)$$

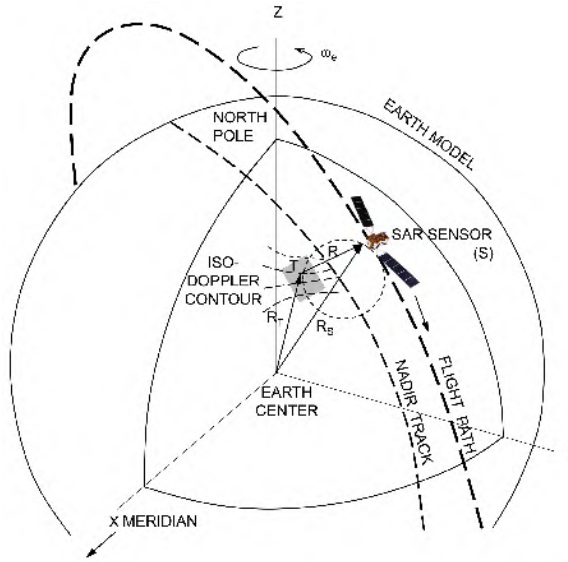


Figure 4.2: Earth model with an ECEF reference system, satellite and target positions. The geolocation procedure intersects R with the earth model surface and the appropriate iso-Doppler contour for scatterer T . Adapted from Olmsted (1993).

where $\mathbf{V}(t_a)$ is the velocity vector of the satellite at the instant of imaging target T , and $f_D(t_a)$ is the Doppler frequency of scatterer T at azimuth position a_T .

Finally, for the *ellipsoid*, T has a vertical elevation $H(c_T)$ above a reference ellipsoid with semi-major and semi-minor axis m and f , respectively, hence

$$\frac{x_T^2}{(m + H(c_T))^2} + \frac{y_T^2}{(m + H(c_T))^2} + \frac{z_T^2}{(f + H(c_T))^2} - 1 = 0. \quad (4.7)$$

$H(c_T)$ is calculated from the cross-range position:

$$H(c_T) = c_T \cdot \sin \theta_{\text{inc}, T}, \quad (4.8)$$

where $\theta_{\text{inc}, T}$ is the incidence angle at T . Optionally, the 3D TRF coordinates can be further transformed into a national/local coordinate system.

From Eqs. (4.5)–(4.7), the precise 3D geolocation relies on the precision of azimuth coordinate a_T , range coordinate r_T , the estimated cross-range \hat{c}_T , and the satellite orbit vectors.

4.2.1. Positioning error sources

The measurements in range and azimuth are affected by additional time-variable positioning components that can range from centimeters to several meters. Tab. 4.1 summarized the positioning errors. Due to the instrumental timing error $t_{a, \text{sysm}}$, azimuth shift $a_{\text{shift}, T}$, tectonic plate movement $a_{\text{tect}, T}$, solid earth tides (SET) $a_{\text{set}, T}$, ocean loading

$a_{\text{ocean},T}$, pole tides $a_{\text{pole},T}$, and atmospheric loading $a_{\text{atm},T}$, the azimuth measurements of Eq. (4.2) can be written as

$$a_T = v_{g/t} \cdot (t_{a,0} + l_T \Delta t + t_{a,\text{sysm}}) + a_{\text{shift},T} + a_{\text{tect},T} + a_{\text{set},T} + a_{\text{ocean},T} + a_{\text{pole},T} + a_{\text{atm},T}. \quad (4.9)$$

Table 4.1: Overview of positioning error components in azimuth and range observations (Dheenathayalan et al., 2016; Gisinger et al., 2017).

Positioning Components	azimuth	range	order of magnitude
Tropospheric delay	Nil	m	2.5 to 3.5 m
Ionospheric delay	Nil	cm	1 to 20 cm ^a
Solid earth tides	cm	dm	-20 to 20 cm
Azimuth shift	dm to cm	Nil	up to cm level
Ocean loading	mm	<cm	up to 10 cm
Ocean Pole tide loading	mm	mm	up to 2 mm
Atmospheric tidal loading	mm	mm	up to 2 mm
Atmospheric pressure loading	mm	<cm	up to 4 cm
Tectonics	dm	dm	up to dm level
pole tides	mm	mm	up to cm level

^a in case of X-band.

Similarly, the range in Eq. (4.3) can be expressed as:

$$r_T = \frac{v_0}{2} \cdot (t_{r,0} + p_T \Delta \tau + t_{r,\text{sysm}}) + r_{\text{apd},T} + r_{\text{tect},T} + r_{\text{set},T} + r_{\text{ocean},T} + r_{\text{pole},T} + r_{\text{atm},T}, \quad (4.10)$$

where $t_{r,\text{sysm}}$ is the internal system delay, and $r_{\text{apd},T}$, $r_{\text{tect},T}$, $r_{\text{set},T}$, $r_{\text{ocean},T}$, $r_{\text{pole},T}$, and $r_{\text{atm},T}$ are atmosphere path delay (APD), tectonic plate movement, SET, ocean loading, pole tides, and atmospheric loading impacts on the range measurement, respectively (Dheenathayalan et al., 2016). Combining the equations, the error terms in azimuth and range can be expressed as:

$$\Delta a_T = v_{g/t} \cdot t_{a,\text{sysm}} + a_{\text{shift},T} + a_{\text{tect},T} + a_{\text{set},T} + a_{\text{ocean},T} + a_{\text{pole},T} + a_{\text{atm},T}, \quad (4.11)$$

and

$$\Delta r_T = \frac{v_0}{2} t_{r,\text{sysm}} + r_{\text{apd},T} + r_{\text{tect},T} + r_{\text{set},T} + r_{\text{ocean},T} + r_{\text{pole},T} + r_{\text{atm},T}, \quad (4.12)$$

where Δa_T and Δr_T describe the contributions in azimuth and range that need to be accounted for. Moreover, the bias due to the reference elevation needs to be accounted for.

The elevation of scatterer T is relative to a reference point. This implies that the uncertainty of the reference elevation will introduce a bias to all PS points. This elevation offset Δc is constant for all PS and affects the geographic position both in the horizontal and vertical direction. The error contributions in azimuth, range, and elevation would transmit to 3D geolocations which have to account for reaching quality geo-localization.

4.2.2. Positioning quality

The 3D positioning quality of point scatterers can be described by the positioning variance-covariance (VC) matrix of the PS. Supposing the error in azimuth, range, and cross-range is independent, the co-variances equal to zero. For each PS, the positioning uncertainty in a 3D radar geometry is given by (Dheenathayalan et al., 2016)

$$\mathbf{Q}_{rac} = \begin{bmatrix} \sigma_a^2 & 0 & 0 \\ 0 & \sigma_r^2 & 0 \\ 0 & 0 & \sigma_c^2 \end{bmatrix}. \quad (4.13)$$

The diagonal component is variances σ_r^2 , σ_a^2 and σ_c^2 in range, azimuth and elevation directions.

According to Eq. (4.9), the variance of azimuth measurement is

$$\sigma_a^2 = \omega \cdot W \cdot \omega^T, \quad (4.14)$$

where $\omega = [t_{a,0}^0 + l_{\xi_T}^0 \Delta t^0 + t_{a,\text{sysm}}^0, v_{g/t}^0, v_{g/t}^0 \Delta t^0, v_{g/t}^0 l_{\xi_T}^0, v_{g/t}^0, 1, 1, 1, 1, 1, 1]$ and $W = [\sigma_{v_{g/t}}^2, \sigma_{t_{a,0}}^2, \sigma_{l_{\xi_T}}^2, \sigma_{\Delta t}^2, \sigma_{t_{a,\text{sysm}}}^2, \sigma_{a_{\text{shift},T}}^2, \sigma_{a_{\text{tect},T}}^2, \sigma_{a_{\text{set},T}}^2, \sigma_{a_{\text{ocean},T}}^2, \sigma_{a_{\text{pole},T}}^2, \sigma_{a_{\text{atm},T}}^2]$. According to Eq. (4.10), the variance of range measurement is

$$\sigma_r^2 = \beta \cdot U \cdot \beta^T, \quad (4.15)$$

where $\beta = [\frac{v_0}{2}, \frac{v_0}{2} \Delta \tau^0, \frac{v_0}{2} \eta_T^0, \frac{v_0}{2}, 1, 1, 1, 1, 1, 1]$ and $U = [\sigma_{tr,0}^2, \sigma_{p_{\eta_T}}^2, \sigma_{\Delta \tau}^2, \sigma_{t_{r,\text{sysm}}}^2, \sigma_{r_{\text{apd},T}}^2, \sigma_{r_{\text{tect},T}}^2, \sigma_{r_{\text{set},T}}^2, \sigma_{r_{\text{ocean},T}}^2, \sigma_{r_{\text{pole},T}}^2, \sigma_{r_{\text{atm},T}}^2]$.

An error ellipsoid is generated with the variances in the three directions. The variances σ_r^2 , σ_a^2 and σ_c^2 describe the three semi-axis lengths of the ellipsoid. The shape of a ellipsoid is derived from the ratio of its axis lengths, given by $(1/\gamma_1 / \gamma_2)$, where $\gamma_1 = \sigma_a \cdot \sigma_r^{-1}$ and $\gamma_2 = \sigma_c \cdot \sigma_r^{-1}$. The orientation of a ellipsoid depends on the local incidence angle of the radar beam at the PS.

The positioning quality could be described in map geometry with a rotation matrix,

$$\mathbf{Q}_T = \mathbf{B}_{3 \times 3} \cdot \mathbf{Q}_{rac} \cdot \mathbf{B}_{3 \times 3}^T, \quad (4.16)$$

where \mathbf{B} is the rotation matrix from radar geometry to a local reference frame. Fig. 4.3 draws a sample of a 3D error ellipsoid of a point, centered at the estimated positions. The viewing geometry is descending orbit. The orientation of ellipsoid is along the cross-range direction with length of γ_2 , perpendicular to the slant range direction. Generally, the variance in elevation direction is larger than in the other two directions, therefore the γ_2 is longer than γ_1 , resulting a prolate spheroid.

4.3. GCP-assisted InSAR precise point positioning

As discussed in the previous section, the geolocation positioning is affected by several biases. Fig. 4.4 illustrates that the range observation, R_{obs} , includes biases due to system-related unknowns and unaccounted geophysical effects, leading to the erroneous geolocation of the target T at position T' .

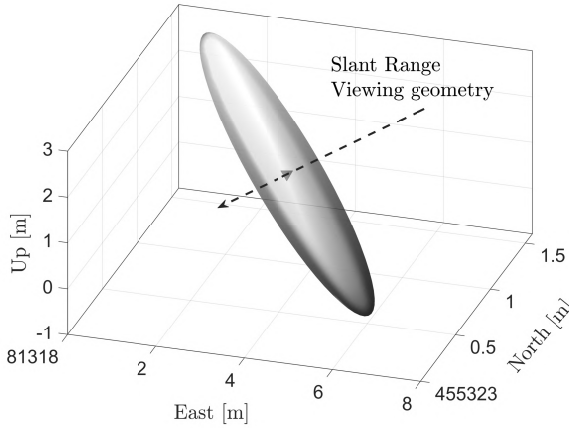


Figure 4.3: A 3D cigar-shaped error ellipsoid illustrates the position uncertainty of a point scatterer.

The estimated range can be expressed as:

$$R_{\text{obs}} = R_{\text{true}} + R_{\text{bias}} + R_{\text{noise}}, \quad (4.17)$$

where R_{noise} is the zero-mean random perturbation of the estimated position, and R_{bias} is the systematic term that we are aiming to correct. The bias term is caused by the delays associated with system-introduced or geophysical factors. The noise includes the contributions that are system-related, geophysical, and processing-related. Assuming that this bias is constant for a relatively small scene, the positions of the targets can be corrected for by using one or more GCPs. Reducing the bias is to move the error ellipsoid to the true position.

In the following section, we discuss two approaches to estimate the bias in azimuth, range, and cross-range using dedicated reflectors. The first approach minimizes the effort for installing a temporary ad-hoc corner reflector during only one SAR acquisition and collecting geodetic ground-truth positioning data. We refer to this approach as the *single-epoch* approach. The second approach requires more efforts and resources and involves a continuously maintained CR, referred to as the *multi-epoch* approach. Note that the benefit of using multiple CRs instead of a single CR is trivial, as it improves the precision of the calculated offsets with $1/\sqrt{N}$.

4.3.1. Single-epoch CR

In this method, a GCP, typically a CR, is deployed and its phase-center position is precisely measured for a single acquisition. In our case study, we determined the location of the apex of the CRs using a GNSS (Global Navigation Satellite System) measurement. Fig. 4.5 shows the concept of the single-epoch method.

The GNSS-derived 3D position $(x_{\text{cr}}, y_{\text{cr}}, z_{\text{cr}})$ is projected onto the 2D radar coordinates, $(a_{\text{cr,g}}, r_{\text{cr,g}})$. From the SAR intensity image we obtain an independent estimation of the radar coordinates of the target $(a_{\text{cr,s}}, r_{\text{cr,s}})$. The azimuth and range offsets are sub-

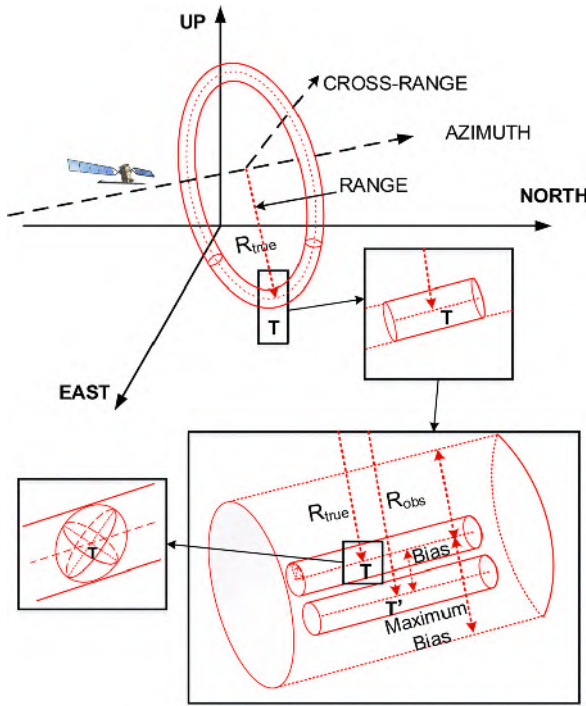


Figure 4.4: Positioning uncertainty cylinder of target T . R_{true} is the range distance to the true position of T , R_{obs} is the observed range distance to the measured position of T' , the distances from T to T' is bias, the maximum bias is radius of the cylinder, the noise term in azimuth, range, cross-range formed the uncertainty ellipsoid.

sequently estimated as

$$\Delta a = a_{cr,s} - a_{cr,g}, \text{ and} \tag{4.18}$$

$$\Delta r = r_{cr,s} - r_{cr,g}, \tag{4.19}$$

respectively. The estimated offsets are applied to the estimated radar coordinates of all the PS in the image.

In azimuth, the variance of the corrected offset is

$$\sigma_{\Delta a}^2 = \sigma_{a,s}^2 + \sigma_{a,g}^2, \tag{4.20}$$

where $\sigma_{a,s}^2$ is the variance of the error in the sub-pixel position estimation of the target in azimuth, as given by (4.1), and $\sigma_{a,g}^2$ is the corresponding variance of the GNSS measurement error. With $(\sigma_{e,g}^2, \sigma_{n,g}^2, \sigma_{u,g}^2)$ representing the variance of GNSS measurement in east, north and vertical direction, the resulting variance in azimuth direction is

$$\sigma_{a,g}^2 = \sin^2 \alpha \cdot \sigma_{e,g}^2 + \cos^2 \alpha \cdot \sigma_{n,g}^2, \tag{4.21}$$

where α is the heading angle between the flight direction and the north direction.

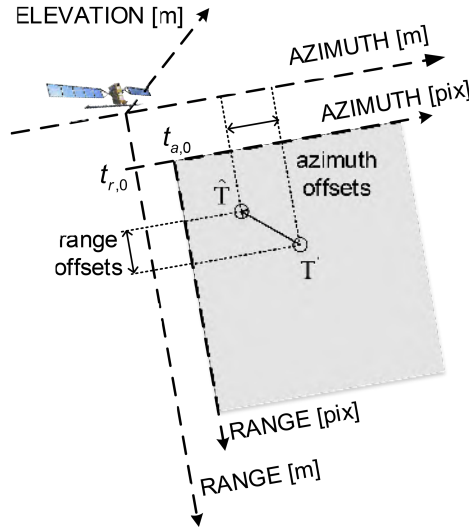


Figure 4.5: Single-epoch CR approach: all points in a radar image are corrected in azimuth-range plane based on the calculated offsets in azimuth and range respectively.

In range, the variance of the error of the corrected offset is:

$$\sigma_{\Delta r}^2 = \sigma_{r,s}^2 + \sigma_{r,g}^2, \quad (4.22)$$

where the second term is

$$\begin{aligned} \sigma_{r,g}^2 = & \sin^2 \theta \cdot (\cos^2 \alpha \cdot \sigma_{e,g}^2 + \sin^2 \alpha \cdot \sigma_{n,g}^2) \\ & + \cos^2 \theta \cdot \sigma_{u,g}, \end{aligned} \quad (4.23)$$

with θ the incidence angle with respect to a horizontal plane.

The main limitation of the single-epoch approach is that it only corrects for the range and azimuth offset, and not for cross-range (or elevation) offset. Consequently, while the method reduces two dimensions of the solution space, which is a positioning improvement, it still leaves the actual 3D geographic position under-determined.

4.3.2. Multi-epoch CR

Finding the 3D geographic positions of PS is possible by installing a reference target for a period spanning multiple epochs, and measuring its position via GNSS. That way, the range and azimuth offsets are estimated as described above, while interferometry can be used to estimate the cross-range positions of points relative to the reference target, and the absolute cross-range position is anchored via the corner reflector. Fig. 4.6 shows the concept of the multi-epoch method. The position of PS scatterers in the image (black symbols) is first corrected in the azimuth-range plane (gray). Then from the interferometric phase, the relative cross-range positions are computed (dashed). Finally, the known position of the CR reference point is used to determine the true geographic position of the point scatterers (hatched).

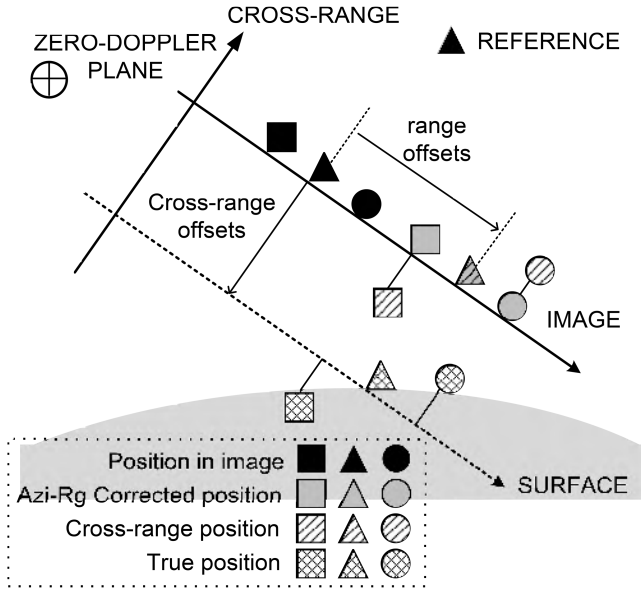


Figure 4.6: Multi-epoch approach: PS (black symbols) are first corrected for the offsets in the azimuth-range plane (gray symbols), and then differed in cross-range via interferometry (dashed) and finally fixed for the cross-range offset (hatched symbols). The solid triangle indicates the reference point (GCP) for cross-range offset estimation.

The geographic elevation (cross-range) position $c_{cr,g}$ of the CR is derived from the GNSS-measured height $H_{cr,g}$ using Eq. (4.8). The offsets in azimuth and range direction are calculated from Eqs. (4.18) and (4.19), respectively. The variances of the calculated azimuth and range offsets are improved by the square root of the number of epochs n .

Since the CR persists for a long time it can be recognized as a PS. As such, the CR can be used as c_0 value in Eq. (4.4), i.e., $c_0 = c_{cr,g}$. The $\sigma_{cr,g}^2$ is dependent on the precision of the GNSS measurement and given by

$$\sigma_{cr,g}^2 = \left(\sigma_{e,g}^2 \cos^2 \alpha + \sigma_{n,g}^2 \sin^2 \alpha \right) \cos^2 \theta + \sigma_{u,g}^2 \sin^2 \theta. \tag{4.24}$$

The relative cross-range differences between the PS point cloud and the reference point is determined using PS interferometry. The estimates of these relative differences will improve when more data will be used in the interferometric stack.

A stack of $n + 1$ acquisitions generates n independent pairs with different baselines $[B_{\perp,1}, \dots, B_{\perp,n}]^T$ and phase observations $[\phi_{T,1}, \dots, \phi_{T,n}]^T$ for target T , relative to the reference point. Using Eq. (4.4), the functional model with the initial range value of r_T^0

can be written as

$$y = E \left\{ \begin{bmatrix} \phi_{T,1} \\ \vdots \\ \phi_{T,n} \end{bmatrix} \right\} = \hat{G}_{n \times 1} \cdot c_T$$

$$= \begin{bmatrix} -\frac{4\pi B_{\perp,1}}{\lambda r_T^0} \\ \vdots \\ -\frac{4\pi B_{\perp,n}}{\lambda r_T^0} \end{bmatrix} \cdot c_T. \quad (4.25)$$

The estimated cross-range is

$$\hat{c}_T = (G^T Q_y^{-1} G)^{-1} G^T Q_y^{-1} y, \quad (4.26)$$

and the variance is

$$\sigma_{\hat{c}_T}^2 = (G^T Q_y^{-1} G)^{-1}. \quad (4.27)$$

The covariance matrix Q_y of time series phase observations is a diagonal matrix with entries

$$\left[\sigma_{\phi_{T,1}}^2, \dots, \sigma_{\phi_{T,n}}^2 \right]^T, \quad (4.28)$$

where σ_ϕ is the standard deviation of a single phase observation as described by (Dheenathayalan et al., 2017)

$$\sigma_\phi \approx \sqrt{\frac{2}{2\text{SCR} - \sqrt{3}/\pi}}. \quad (4.29)$$

Hereby, the precision of cross-range $\sigma_{\hat{c}_T}$ is

$$\sigma_{\hat{c}_T}^2 = \left(\frac{\lambda r_T^0}{4\pi} \right)^2 \cdot \left(\frac{B_{\perp,1}^2}{\sigma_{\phi_{T,1}}^2} + \dots + \frac{B_{\perp,n}^2}{\sigma_{\phi_{T,n}}^2} \right)^{-1}. \quad (4.30)$$

The precision of cross-range depends on the phase quality and the variability of the baseline. Longer baselines give a more precise cross-range estimation (Rocca, 2004) without requiring more data acquisitions.

Fig. 4.7 shows the cross-range precision of a target with SCR = 25 dB as a function of the number of epochs n . The perpendicular baselines B_\perp were random values with uniform distribution at a range between -100 m and 100 m, which is the orbital tube of Sentinel-1 (Geudtner et al., 2017). The precision increases with the epochs, from about 1.7 m with 25 epochs to better than 1 m with 74 epochs or more.

4.4. DSM-assisted InSAR precise point positioning

A LiDAR-based DSM may be used as a network of thousands of GCP. The prerequisite for the usage of a DSM for reference is that the LiDAR DSM and InSAR point cloud describe the same surface, or the penetration depth of LiDAR and SAR into the ground is equal. For (a) the typical X-, C-, and L-band radar data, and (b) the typical build environment (urban areas or infrastructure), there is no significant penetration of radar signals (Ulaby

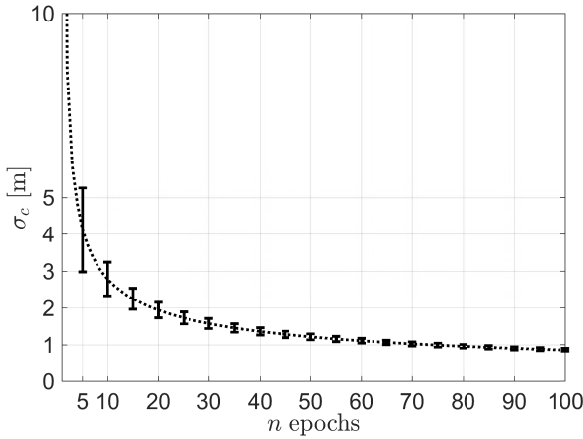


Figure 4.7: The standard deviation of estimated cross-range of a target with SCR 25 dB for Sentinel-1 as a function of the number of acquisitions n within an orbital tube with a radius of 100 m.

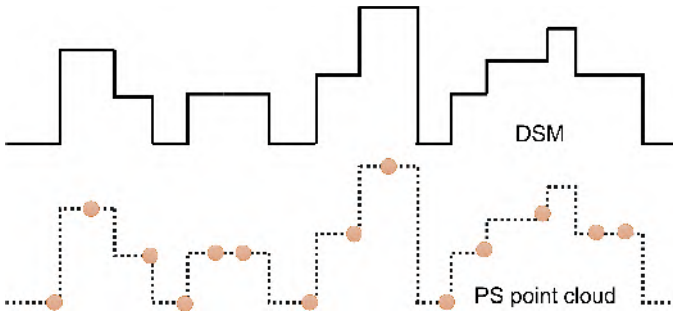


Figure 4.8: DSM-assisted approach: the concept of matching PS point cloud to a digital surface model (DSM). Both PS point cloud and DSM depict the Landscape in a test area with different spatial sampling densities. The optimal matching of these two data would give the correction offsets for the entire PS point cloud.

et al., 1986). To fix the Δa , Δr , and c_0 of PS, these PS need to be matched with corresponding points in the LiDAR point cloud. We use the Iterative Closest Point method (ICP) with the PS positioning ellipsoids (Hanssen et al., 2018; Yang et al., 2019a), which minimizes the differences between two point clouds in an iterative way and generates transformation parameters. Fig. 4.8 shows the concept of the multi-epoch method.

The point matching between the LiDAR point cloud and the PS is done in the SAR geometry. For this purpose, the LiDAR point cloud is radar-coded to the radar geometry using the orbit of the master image of the stack. A fine coregistration is performed using the iterative closest point (ICP) algorithm (Svirko et al., 2002; Chetverikov et al., 2005), which minimizes the sum of the weighted Euclidean distance between LiDAR point cloud and PS by least square estimation (LSE) in an iterative way. Each iteration of the 3D error ellipsoid based ICP includes two steps: matching pairs of LiDAR point cloud and PS based on the 3D error ellipsoid; and finding the transformation that minimizes the weighted mean squares distance between pairs of points. The transformation parameters esti-

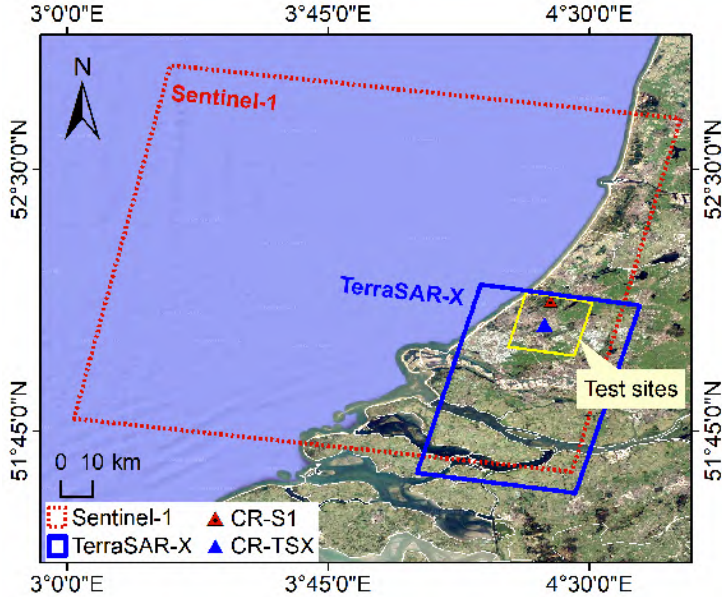


Figure 4.9: Coverage of TerraSAR-X and Sentinel-1 data and location of installed CRs.

mated by the ICP method yield the offsets in azimuth, range, and cross-range, that we seek to correct. The quality of the corrected position is dependent on the quality of the DSM model and the accuracy of point registration.

4.5. Experiment setup

4.5.1. SAR data

The test site was in Delft, the Netherlands. Two data-stacks were collected over this area. For each data stack, we processed at least 40 images. Fig. 4.9 shows the location of the test area, the bounding polygons of the TerraSAR-X and Sentinel-1 data stacks, and the location of installed reflectors. Tab. 4.2 provides relevant parameters of data analyzed. The PSI results from two data stacks are different in point density, target detect-ability due to data characteristics variation. Thus, we applied the proposed method to these two data stacks.





4.5.2. Artificial reflectors

An artificial radar reflector is a passive device that reflects the incoming electromagnetic signal directly back to the antenna. The trihedral reflector is the most common type used in calibration and deformation monitoring (Garthwaite et al., 2015). A trihedral reflector formed by three orthogonal planes and generate a triple bounce signal back to the sensor. A trihedral reflector performed well with alignment errors because its radar cross section (RCS) pattern has a 3 dB beam-width with approximately 40 degrees. Tab. 4.3 summarizes the typical trihedral and dihedral reflectors with their theoretical RCS.

Table 4.2: TerraSAR-X, and Sentinel-1 SAR Data characteristics

Satellite/Parameter	TerraSAR-X	Sentinel-1
Test site	Ypenburg	Wassenaar
Track	T048	T110
Band	X	C
Start Date	2012.08.11	2017.11.08
End Date	2014.03.06	2018.07.18
Number of images	46	40
B_{\perp} [min/max] [m]	-382/142	-88.4/117.7
Acquisition mode	SM	IW
Pass direction	Desc	Desc
Polarization	HH	VV
Incidence angle [°]	22.3 – 25.6	35.7 – 41.7
Heading [°]	192.22	190.12
Rang. sampling [m]	0.9	2.3
Azim. sampling [m]	1.7	13.8
Rang. Bandw. [MHz]	150	56.5
Azim. Bandw. [Hz]	2765	327

Table 4.3: Typical corner reflectors and their theoretical maximum RCS. a is the inner length of the target.

Target	Structure Diagram	Maximum RCS [dBm^2]
Triangular trihedral		$\frac{4\pi a^4}{3\lambda^2}$
Square trihedral		$\frac{12\pi a^4}{\lambda^2}$
Circular trihedral		$\frac{0.507\pi^3 a^4}{\lambda^2}$
Dihedral		$\frac{8\pi a^4}{\lambda^2}$

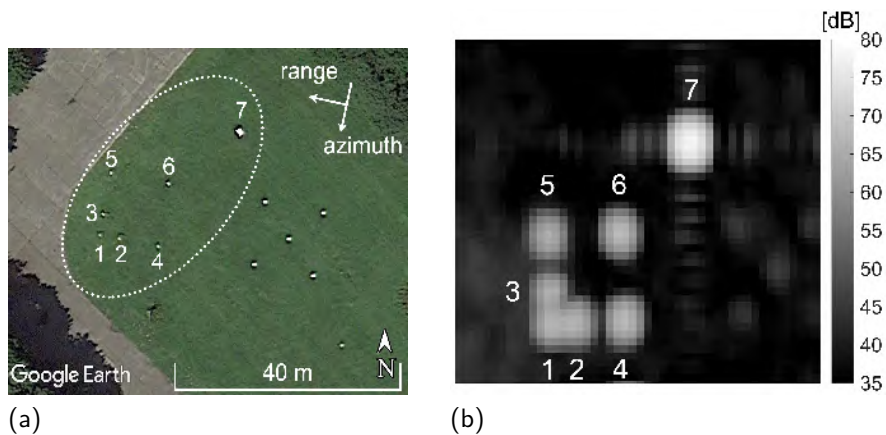


Figure 4.10: (a) Google Earth image of seven trihedral corner reflectors installed for the TerraSAR-X (T048), (b) Mean intensity image from 46 TerraSAR-X images covering the seven corner reflectors.

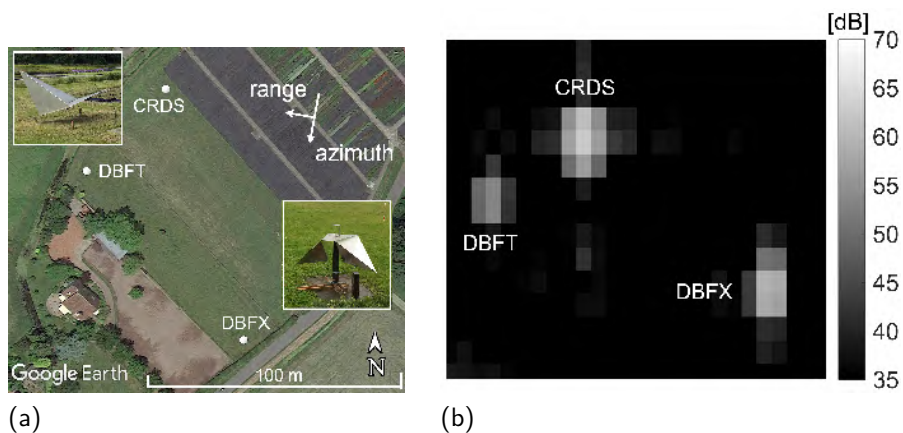


Figure 4.11: (a) Google Earth image of three CRs oriented for the Sentinel-1 stack (T110), (b) Mean intensity image from 40 Sentinel-1 images covering the three reflectors.

At the Ypenburg test site, we installed six small (45 cm sides) trihedrals, CR1–CR6, and one big (1 m sides) trihedral, CR7. The CRs remained on the field between August 2012 and March 2014 and were optimally oriented for the geometry of the TerraSAR-X acquisitions. Fig. 4.10a shows the positions of the CRs overlaid on a Google Earth image. The reflectors are clearly visible in the mean intensity image of 46 TerraSAR-X images, as shown in Fig. 4.10b.

For our analysis, we use CR4, CR5, CR6, and CR7 to avoid the impact of the mutual side-lobes of the first three. Differential GNSS and tachymetry are used to precisely measure the apex positions of these CRs. These positions are determined with a precision (1σ) of 1 cm in the horizontal (east and north), and 2 cm in the vertical.

In the Wassenaar site, we installed one square-based trihedral CR, and two Double Back-flip (DBF) CRs (Hanssen, 2017), from November 2017, oriented for the Sentinel-1 descending data, see Fig. 4.11a.

4.5.3. DSM data

In addition to the CRs, we utilise a DSM model, AHN ('*Actueel Hoogtebestand Nederland*' in Dutch), collected over the Netherlands by means of airborne laser altimetry with a posting of 50 cm (horizontally) for objects larger than 2×2 meters and a vertical offset uncertainty of 5 cm and a 5 cm stochastic error (Van der Zon, 2013; van Natijne et al., 2018). AHN is a multi-annual program, including AHN-1, AHN-2, AHN-3, providing both the raster data and the point clouds. We utilize the AHN-2 point cloud for DSM correction and the 0.5 m grid DSM for cross-comparison.

Fig. 4.12 shows a 1×1.25 km² patch of AHN-2 data corresponding to our test area. Height variation over the test site is a critical factor for point matching. In other words, it is difficult to do the matching in a flat area without any variation in height. The height variogram map in the test area is given in

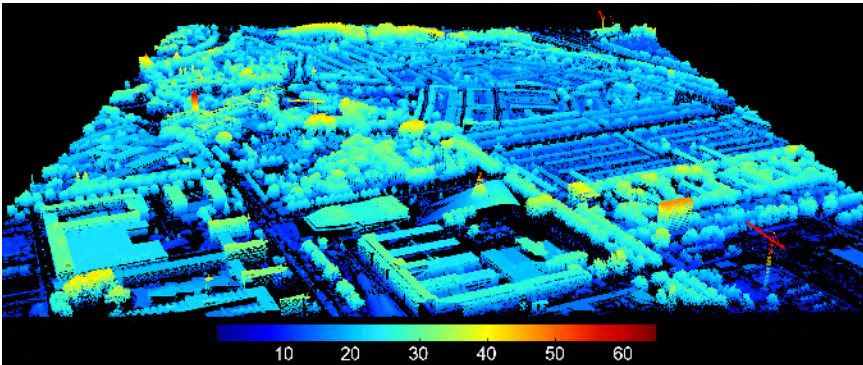


Figure 4.12: DSM model (AHN2,U37EN2) over Delft area, ranging from 0 to +65 m. The height is color-coded.

4.6. Results

In this section, we present and compare the correction results of TerraSAR-X and Sentinel-1 data stack using the proposed methods. The SAR data-stacks were processed with the

Delft implementation of persistent scatterer interferometry (DePSI) (van Leijen, 2014).

4.6.1. TerraSAR-X results

Fig. 4.13 shows the estimated elevations for the PS identified in the TerraSAR-X data stack. As usual, high PS densities are found along streets and man-made structures. White areas correspond to vegetated areas and water bodies, where no PS was selected. The point density is 2141 PS/km². The results were projected in the Dutch national reference system RD ('*Rijksdriehoeksstelsel*' in Dutch) and vertical reference system of the Amsterdam Ordnance Datum NAP ('*Normaal Amsterdams Peil*' in Dutch). The estimated heights are color-coded, from -10 to 40 m.

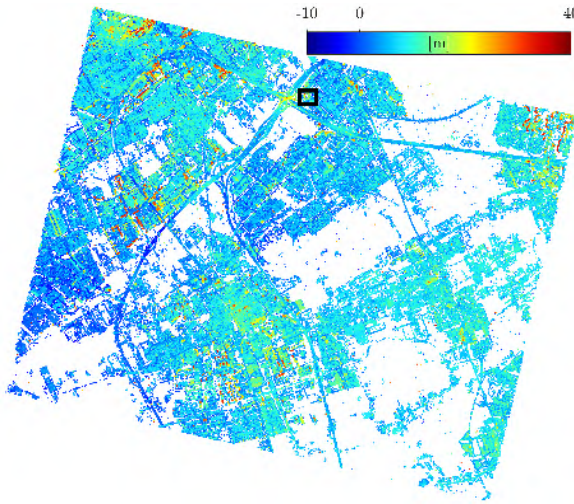


Figure 4.13: Geo-coded PSI point cloud for our test area generated from the TerraSAR-X data stack in RD coordinates. The x - and y - axes correspond to RD east and north, respectively. The estimated height is colour-coded in the NAP datum. The results in the Kyocera Stadium marked within a rectangular box were compared to the LiDAR point cloud in Fig. 4.15 and Fig. 4.16.

Tab. 4.4 gives the offsets of the estimated positions of the CRs after applying the different correction methods with respect to their measured positions. The uncertainty of the CR-assisted approaches is calculated using Eqs. (4.20), (4.22), and (4.24), while the uncertainty of the sub-pixel localization is calculated according to the position variances of a target in a stack of images. The performance of the DSM-assisted approach depends on the co-registration accuracy. It is calculated by dividing the LiDAR point cloud into several subsets, calculating the offsets respectively for each subset, and computing the variances of the resulting offsets. The offsets were converted into local coordinate system by assuming the cross-range offset is zero in single-epoch and geophysical approaches.

The offsets estimated using the different approaches are similar, and consistent with the offsets estimated by Dheenathayalan et al. (2016). The largest offset was observed in the cross-range direction, which corresponds to the reference cross-range value. The atmospheric path delay mainly causes range offsets. Obviously, changing the coordinate system to a local geophysical coordinate system introduces correlations between the dif-

Table 4.4: Calculated offsets in azimuth, range, and cross-range directions, and east, north, and up directions for the TerraSAR-X PSI point cloud.

Method	Δa [m]	Δr [m]	Δc_0 [m]
Single-epoch CR	0.52 ± 0.04	-2.25 ± 0.02	n/a
Multi-epoch CR	0.50 ± 0.01	-2.26 ± 0.02	20.40 ± 1.89
DSM	0.58 ± 0.04	-2.32 ± 0.04	19.01 ± 0.51
Geophysical ^a	0.57 ± 0.07	-2.28 ± 0.02	n/a

Method	Δe [m]	Δn [m]	Δu [m]
Single-epoch CR	-5.32 ± 0.03	1.74 ± 0.04	0
Multi-epoch CR	-12.82 ± 1.71	2.34 ± 0.37	8.32 ± 0.77
DSM	-11.42 ± 0.49	1.97 ± 0.14	7.75 ± 0.21
Geophysical ^a	-5.42 ± 0.03	1.80 ± 0.07	0

^a Correction includes azimuth shifting, path delay, solid earth tide, plate motion from Dheenathayalan et al. (2016).

ferent offsets. For example, a cross-range offset has components in both east and north directions.

The corrected positions were validated with the apex location measured with Differential GNSS and tachymetry for those CRs that were not used to estimate the corrections. The resulting Root Mean Square Errors (RMSE) in the radar coordinates (azimuth, range and cross-range), and local coordinates (east, north, and up) are reported in Tab. 4.5. Before the correction, the entire solution is tied to the height of a selected reference point. Similarly, we used the same height reference in the single-epoch approach and geophysical approach.

Table 4.5: Root Mean Square Errors of CRs in the radar coordinates (azimuth, range, and cross-range), and local coordinates (east, north, and up) for the TerraSAR-X point cloud. The geocoded position of PS before and after applying the corrections are compared with the apex location measured with GNSS in CRs. The post-correction methods include using single-epoch CR, multi-epoch CR, and DSM.

	a [m]	r [m]	c [m]	e [m]	n [m]	u [m]
Before Corrections	0.78	2.39	20.79	12.90	2.13	8.48
Single-epoch CR	0.31	0.18	20.79	7.59	0.46	8.48
Multi-epoch CR	0.32	0.17	1.01	0.67	0.36	0.41
DSM	0.28	0.13	2.01	1.60	0.31	0.81
Geophysical	0.28	0.16	20.79	7.54	0.41	8.48

As expected, both single-epoch CR calibration and geophysical corrections do not correct for absolute cross-track errors, which results in coupled vertical and mostly east-west errors. Using a CR at all epochs, the offsets in elevation were compensated, achieving a decimeter-level 3D positioning error. The DSM-assisted corrections are similar to the multi-epoch CR correction for azimuth and range, but the cross range RMSE is twice as large: 2 m instead of 1 m.

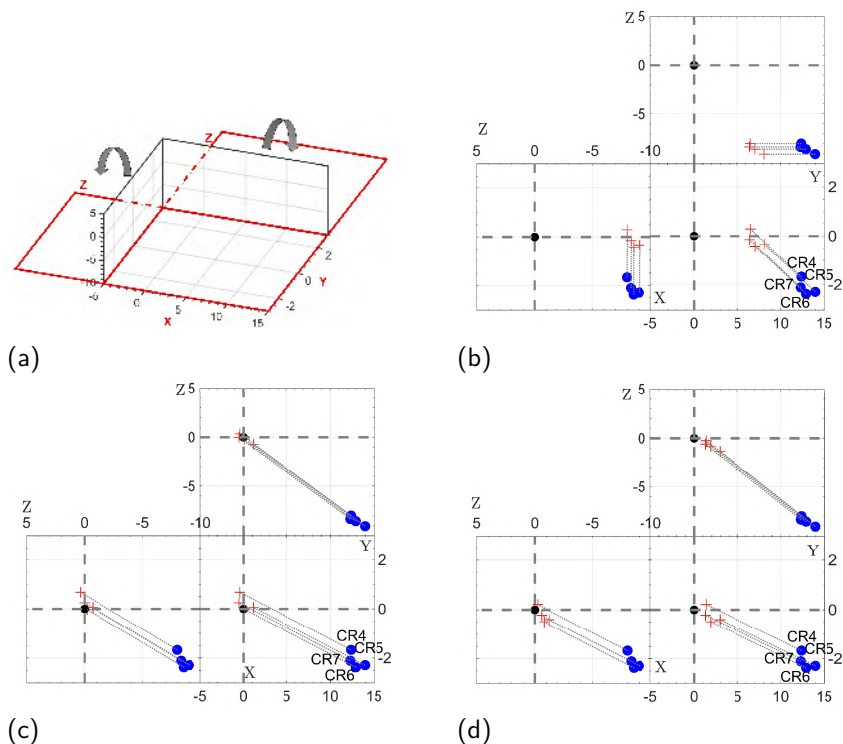


Figure 4.14: Position offsets relative to GNSS measurement in CR4, CR5, CR6, and CR7 before and after applying the corrections are visualized. (a) The diagram of the 3D coordinate system into a 2D plane graph. The corrected results with (b) a single-epoch CR, (c) a multi-epoch CR, and (d) an airborne DSM model. Blue points indicate the offsets relative to measured GNSS position before corrections, and red plus signs indicate the offsets after corrections. The projections in the three orthogonal planes show in X-Z, Y-Z, and X-Y show the corrections.

Fig. 4.14 visualizes the offsets between the corrected positions and GNSS-derived positions. The 3D coordinate system is flipped to horizontal. Thus the offsets could be clearly shown in a plane graph.

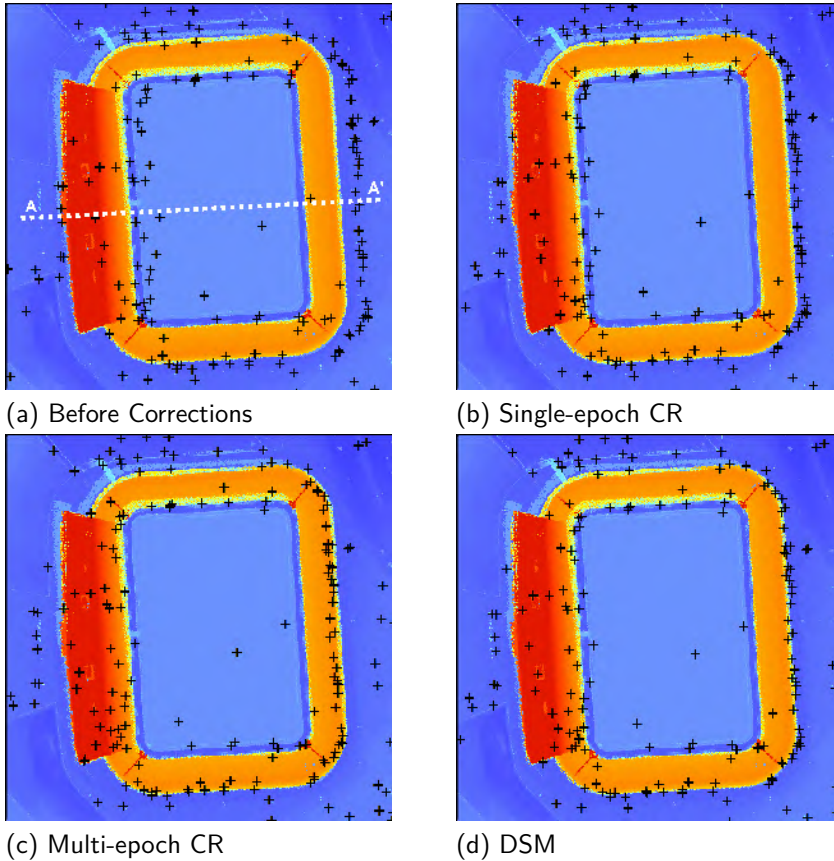


Figure 4.15: 2D horizontal accuracy analysis of the TerraSAR-X PS point cloud at the Kyocera stadium. PS point cloud (a) before corrections, and corrected with (b) a single-epoch CR, (c) a multi-epoch CR, and (d) an airborne DSM model, overlaid on the LiDAR data. The LiDAR data is color-coded as Fig. 4.13. The 1D vertical analysis of Fig. 4.16 is along the line of AA'.

As a test of the geolocation, we compare the PS point cloud before and after correction to the reference LiDAR-based DSM for a region indicated by the rectangle in Fig. 4.13, which corresponds to a sports stadium in The Hague. Fig. 4.15 provides a top-view of the color-coded DSM with the PS overlaid for the different methods. Before the corrections, there is a clear shift between the PS and the stadium. The alignment improves after single-epoch CR correction, and it seems to enhance further using the multi-epoch and DSM-assisted approaches. Fig. 4.16 shows a cross section of the stadium along the AA' line indicated in Fig. 4.16. The multi-epoch CR and DSM corrections bring the points to the right height level.

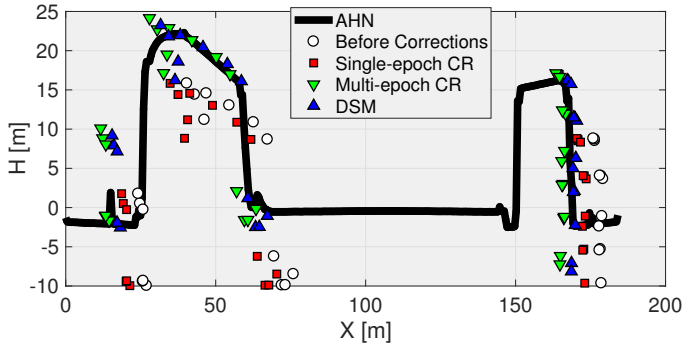


Figure 4.16: 1D vertical accuracy analysis of the TerraSAR-X PS point cloud over the Kyocera Stadium. PS point cloud before corrections, and point clouds corrected with a single-epoch CR, a multi-epoch CR, and an airborne DSM model, overlaid on the LiDAR data.

4

4.6.2. Sentinel-1 results

The topographic map of PSI results from Sentinel-1 is illustrated in Fig. 4.17, projected in the RD-NAP reference system. The colors represent the estimated heights, from -10 to 140 m. The point density is 707 PS/km².

Tab. 4.6 gives the offsets of the estimated positions of the CRs after applying the different correction methods. The largest offset was observed in the azimuth direction, followed by the elevation correction, and the range correction.

Table 4.6: Calculated offsets in azimuth, range, and cross-range directions, and east, north, and up directions for the Sentinel-1 point cloud.

	Δa [m]	Δr [m]	Δc_0 [m]
Single-epoch CR	16.41 ± 0.21	-1.09 ± 0.13	n/a
Multi-epoch CR	16.32 ± 0.03	-1.06 ± 0.03	-4.70 ± 1.81
DSM	14.48 ± 1.47	-0.96 ± 0.24	-2.63 ± 0.45

	Δe [m]	Δn [m]	Δu [m]
Single-epoch CR	-1.43 ± 0.14	-16.58 ± 0.22	0
Multi-epoch CR	2.23 ± 1.45	-17.20 ± 0.34	-2.80 ± 1.41
DSM	0.79 ± 0.84	-15.03 ± 1.55	-1.57 ± 0.27

The azimuth offsets could be due to higher order bi-static effects, between the mid-scene bi-static correction and the required one due to the slant range offset from mid-scene, see Schubert et al. (2015). Recent research on the geolocation accuracy of Sentinel-1 data reports a subswath-dependent azimuth offset up to 4 m in the IW mode (Schubert et al., 2017). Given the 20 m azimuth resolution of Sentinel-1, the error is within the size of a resolution cell.

The 3D offsets estimated using the multi-epoch and DSM-assisted methods are roughly comparable, although for range and azimuth direction the multi-epoch CR method is

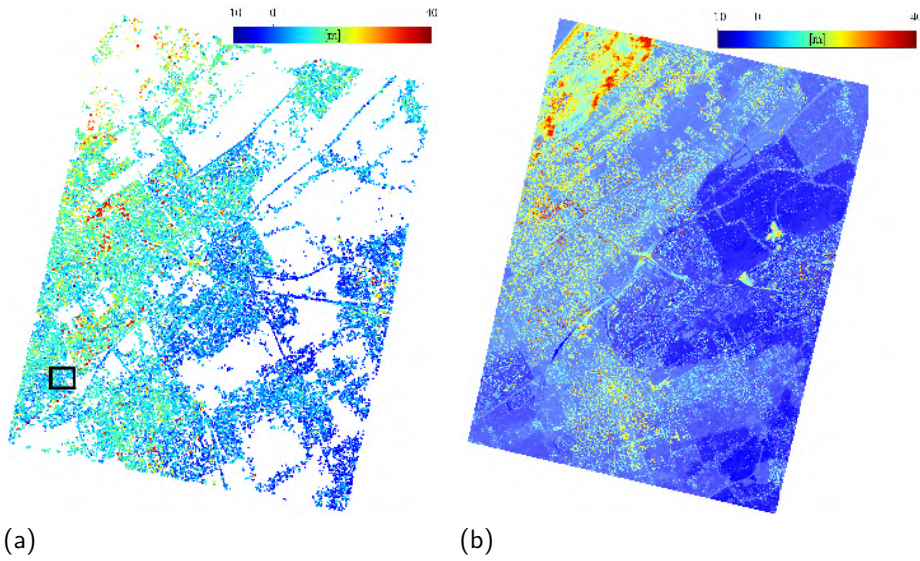


Figure 4.17: (a) Geo-coded PSI point cloud for our test area generated from Sentinel-1 in RD coordinates. The x - and y - axes correspond to RD east and north. The estimated height is colour-coded in the NAP datum. The results in the Moerwijk area of The Hague, marked by the rectangular box, were compared to the LiDAR point cloud in Fig. 4.19 and Fig. 4.20. (b) AHN-2 point cloud in the test site with color-coded heights.

better, whereas for cross-range the DSM method is better, in terms of the variances. This is to be expected due to the coarse azimuth resolution of Sentinel-1, as the number of DSM points matched to a PS is drastically reduced.

The corrected positions were validated with GNSS measurements. The RMSE in the east, north, and up directions is given in Tab. 4.7. The 3D geolocation accuracy achieved using the multi-epoch method is approximately 3.6 m. This is better than the absolute location error accuracy specification of Sentinel-1 (7 m in 2D azimuth-range positioning) (Bourbigot et al., 2016). The geolocation accuracy obtained after a DSM-assisted correction is slightly worse but still better than the Sentinel-1 specifications. The corrected results assisted by single-epoch CR (about 5.4 m) are also close to the specification. There is still about 3 m of residual error in the north direction, which may relate to the azimuth errors reported by (Schubert et al., 2017). Fig. 4.18 visualizes the offsets with flipping the plane in the 3D coordinate system into a 2D plane. The plots show the effectiveness of the corrections.

The PS point cloud before and after the corrections is further compared with the reference LiDAR data. A zoom-in region is a group of buildings in the Hague, indicated by the rectangle in Fig. 4.17. Fig. 4.19 provides a top-view of the DSM data with the non-corrected and corrected PS point cloud. Clearly, the applied corrections have compensated for the 2D shift. The height shift was corrected with the single-epoch CR and the DSM-assisted method as the cross-section along the BB' line shows in Fig. 4.20.

Table 4.7: RMSE of CRs in the radar coordinates (azimuth, range and cross-range), and local coordinates (east, north, and up) for the Sentinel-1 point cloud. The geocoded position from PSI before and after applying the corrections are compared with the apex location measured with GNSS on the CRs. The post-correction methods includes a single-epoch CR, a multi-epoch CR, and DSM.

	a [m]	r [m]	c [m]	e [m]	n [m]	u [m]
Before Corrections	16.92	1.58	3.70	1.86	17.93	2.22
Single-epoch CR	3.80	0.74	3.70	3.47	3.63	2.22
Multi-epoch CR	3.80	0.67	1.62	0.72	3.46	0.97
DSM	4.26	0.74	1.45	1.13	4.29	0.88

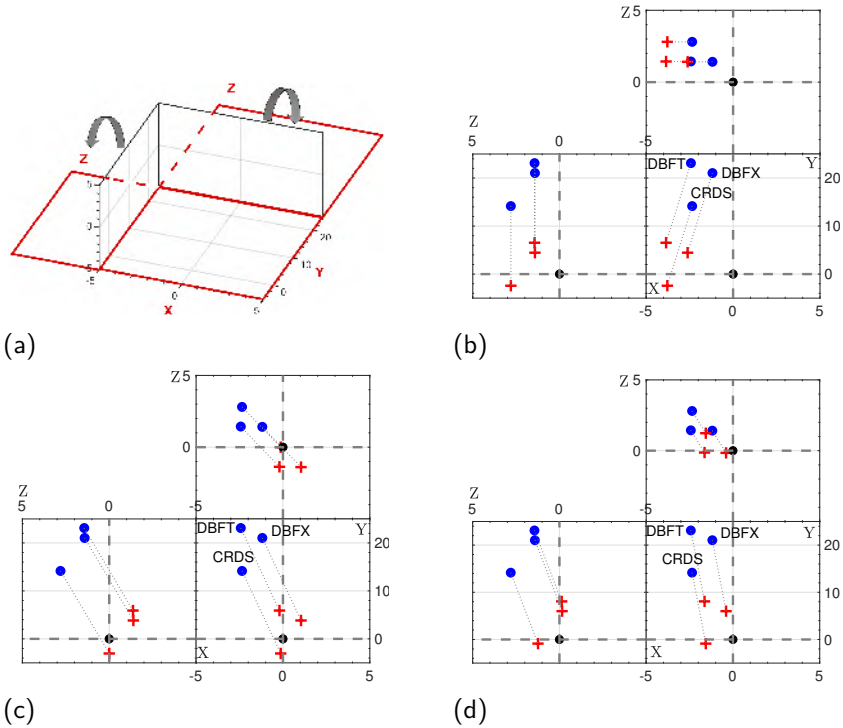


Figure 4.18: Position offsets relative to GNSS measurement in CRDS, DBFX, and DBFT before and after applying the corrections are visualized. (a) The diagram of 3D coordinate system into 2D plane graph. The corrected results with (b) a single-epoch CR, (c) a multi-epoch CR, and (d) an airborne DSM model. Blue points indicate the offsets relative to measured GNSS position before corrections, and red plus signs indicate the offsets after corrections.

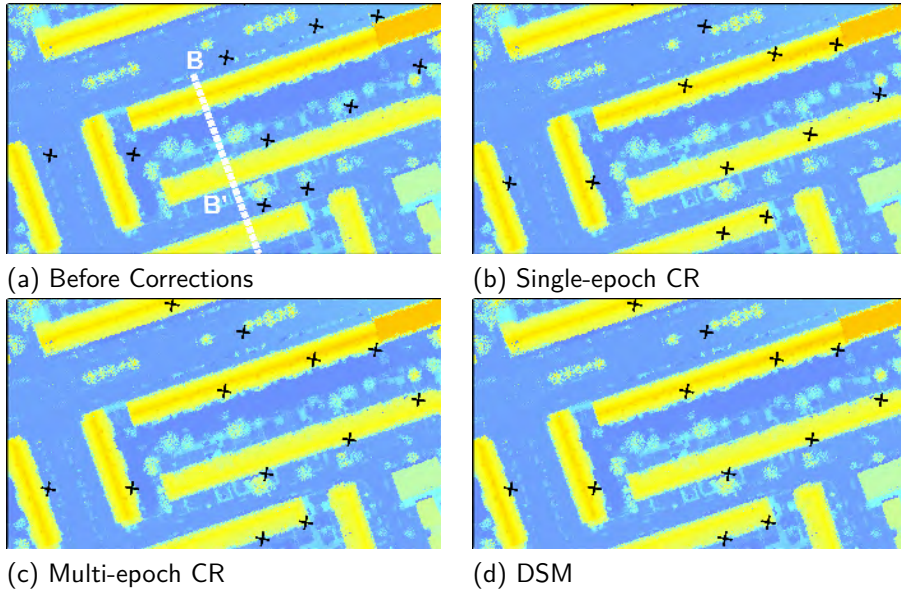


Figure 4.19: 2D horizontal accuracy analysis of Sentinel-1 PS point cloud of buildings in Moerwijk, the Hague. PS point cloud (a) before corrections, and corrected with (b) single-epoch CR, (c) multi-epoch CR, and (d) a airborne DSM model (DSM), overlaid on the LiDAR data. The 1D vertical analysis is along the line of BB', see Fig. 4.20.

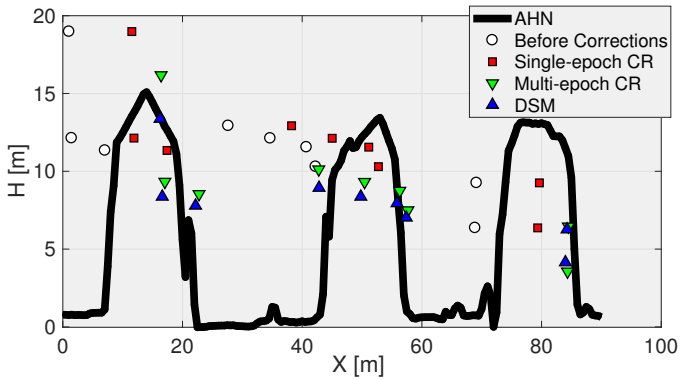


Figure 4.20: 1D vertical accuracy analysis of Sentinel-1 PS point cloud in Moerwijk, the Hague. PS point cloud before corrections, point clouds corrected with single epoch CR, multi-epoch CR, and a airborne DSM model, overlaid on the LiDAR data.

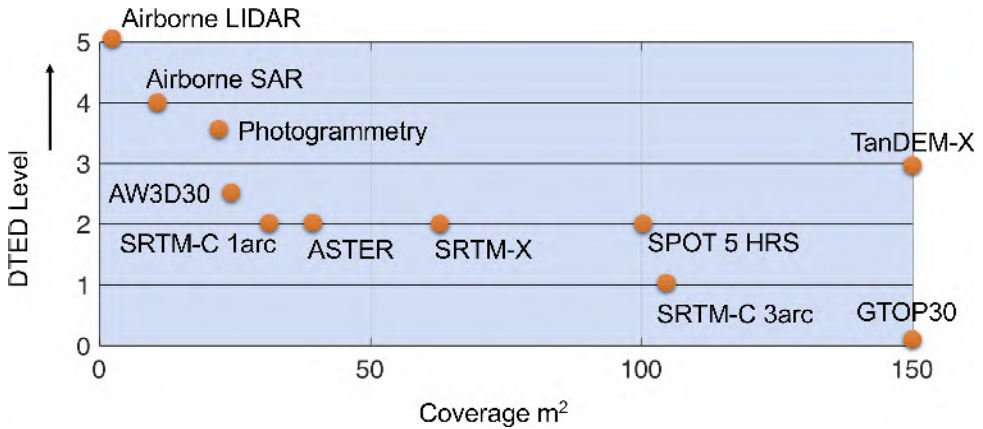


Figure 4.21: The coverage and DTED Level of available digital elevation models, adapted from (Hajnsek et al., 2009).

4.6.3. DSM product evaluation

Even the accuracy of DSM-assisted correction is less than the CR-assisted correction. A DSM-assisted correction is a very appealing option, as it does not require the installation and maintenance of CR. However, the drawbacks of this approach is that it requires a non-trivial processing step to reliably match PS with points or features on the DSM. The accuracy of the estimated corrections will obviously depend on the quality of the DSM.

A standard product specification for digital elevation model named as digital terrain elevation data (DTED) is released by National Geospatial-Intelligence Agency (NGA) with the definitions of absolute positioning accuracy and spatial resolution for each level, specifically DTED-1 and DTED-2 (Heady et al., 2009; Zink et al., 2006). The DTED was defined for globe scale elevation data, and the higher level data is referring to as high-resolution terrain information (HRTI). The DTED-3/4 is also called HRTI-3/4. Therefore, we analyze the positioning precision with the varying DTED levels, see Tab. 4.8. Fig. 4.21 shows current available digital elevation models.

Table 4.8: Digital Terrain Elevation Model (DTED) and High-Resolution Terrain Information (HRTI) specifications.

Specification	Spatial Resolution	Absolute vertical Accuracy (90%)	Absolute Horizontal Accuracy (90%)
DTED-1	90 m (3 arcsec)	50 m	30 m
DTED-2	30 m (1 arcsec)	23 m	18 m
DTED-3/HRTI-3	12 m (0.4 arcsec)	10 m	10 m
DTED-4/HRTI-4	6 m (0.2 arcsec)	5 m	5 m

The quality of the Lidar DSM data used in this study (AHN-2) is significantly better than DTED-4 specification. In order to evaluate the DSM quality dependence of the DSM method, we degraded the AHN-2 to match the different DTED specifications by filtering

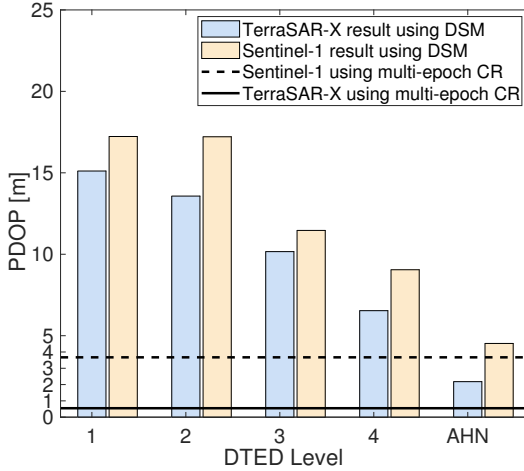


Figure 4.22: Positioning precision as a function of the DTED level. The vertical axis shows the 3D positioning dilution of precision (PDOP) with respect to GNSS measurements of the apex location of CRs.

the data spatially to the desired resolution and adding zero-mean Gaussian distributed noise.

Fig. 4.22 shows the positioning precision as a function of the DTED level. The vertical axis shows the 3D positioning dilution of precision (PDOP) as

$$\text{PDOP} = \sqrt{\text{RMSE}_e^2 + \text{RMSE}_n^2 + \text{RMSE}_u^2}, \quad (4.31)$$

where RMSE is the root mean square error with respect to GNSS measurements of the apex location of CRs.

For a DSM at DTED1 level, the PDOP values are close to the values before corrections, implying that this DSM product does not improve the geolocation of PS point clouds. For DTED2, the PDOP values improve, but not significantly. A significant improvement was observed moving to DTED3 levels. This is due to the fact that the spatial resolution of DTED3 is closer to that of Sentinel-1. The precisions achieved using DTED4 are yet better, and the LiDAR-based AHN data yield the best results. This is due to the dense spatial sampling and precise absolute positioning of AHN data for depicting the height variability within the imaging scene.

The result of the DSM-assisted geolocation approach depends on the precision and the spatial resolution of the available DSM and also the used algorithm, see examples using different algorithms with DSM to evaluate the height shift between PSI point cloud and DSM in Chang and Hanssen (2014); Yang et al. (2016).

4.7. Comparison of correction methods

The practical pros and cons of the discussed methods for precise point positioning are summarized in Tab. 4.9. We define σ_{CR} as the precision of the calculated offsets of the single epoch CR approach, T_0 as the estimated time required for the installation of a

Table 4.9: The characteristics of the positioning correction methods. Advantages and disadvantages.

Methods	Single-epoch CR	Multi-epoch CR	DSM	Geophysical
Solution space	Line (2D)	Point (3D)	Point (3D)	Line (2D)
Advantages	Temporary deployment; ad hoc; No monumentation needed; Fast (10 ¹); easy; cheap	3D correction Highest 3D precision	3D corrections No area access necessary	No area access necessary
Disadvantages	2D bias correction only; No elevation correction; Requires area access;	Monumentation needed; Permanent deployment; Requires area access; Regular inspection and maintenance needed; Expensive; Re-sources	Requires high quality DSM; Requires significant height variability; Requires high quality point matching method	2D bias correction only; No elevation correction; Requires model input for atmosphere, tides, tectonics, instrument;
Effort	1 CR placement; 1 GNSS real time kinematic;	1 CR monumentation: T_0 [†] ; 1 GNSS real time kinematic; Regular check-up required	Algorithmic	Computation
Precision	σ_{CR} [†]	σ_{CR}/\sqrt{n} [†]	dm	dm

[†] σ_{CR} : precision of the calculated offsets in the Single-epoch CR approach. T_0 : estimated time required for the installment of a single CR monumentation. n : the number of epochs.

single CR monumentation, and n as the number of epochs. Note that T_0 depends on local conditions, typically ranging from 0.5 to 3 days.

Both the single-epoch calibration as well as the geophysical correction lack the absolute cross-range correction, which yields only limited improvement in positioning accuracy. Of these two, the former requires physical access to the area, while the latter needs various physical parameters to be available.

The best accuracy and precision is achieved using one CR over multiple epochs. The maintenance cost scales with the number of epochs, which is dependent on the baseline distribution of the SAR data stack: a greater number of epochs is needed if the orbital tube is smaller.

The DSM-assisted approach is less accurate than the multi-epoch method, but it is a reasonable alternative if a high-precision DSM is available, with the main advantage of not requiring area access.

4.8. Conclusions

The geolocalization of PSI point clouds significantly improves their overall practical value. As this requires a mapping from 2D radar coordinates to 3D geographic coordinates, GCP's such as corner reflectors can assist in this mapping. The optimal way of deploying

a corner reflector is by deploying it in a time series of SAR images, such that its phase can be analyzed as a persistent scatter. That way, the highest precision, and accuracy in the position of a PSI point cloud is obtained. Yet, this comes at a cost in terms of efforts and resources. Alternatively, when a high-precision, high resolution digital surface model is available, DTED4-level or better, exhibiting sufficient elevation variability, this could be used as a virtual set of GCP, almost comparable geolocate precision.

Deployment of a corner reflector for just one single SAR acquisition, or using additional geophysical information does not provide absolute 3D geographic coordinates, and can only be used to limit the degrees of freedom in azimuth-range plane.

5

Understanding persistent scatterers with ray-tracing

Estimating the precise geographic coordinates of point scatterers has been discussed in chapter 4. However, due to the complicated interactions between the transmitted signal and target objects on the ground, the position of the geometric phase center may not be the true physical source of the signal. This chapter is aimed at a better understanding of the relationship between precise geolocation of the scatterer and its physical source using geometrical optics and develops a new approach that links persistent scatterers to urban building models.

In Section 5.1, we give a background of this chapter, followed by a review on the principles of the ray-tracing based SAR simulator in Section 5.2. The simulation uses 3D city models with varying degrees of geometric details (level of detail, or LOD). The influence of the LOD on the simulation scatterers are discussed in Section 5.3. A new methodology of linking the scatterers to the built model using ray-tracing is proposed in Section 5.4. This method was applied to the point clouds detected from a stack of TerraSAR-X images, see Section 5.6. The effect of multiple scattering on the interpretation of the estimates is demonstrated in Section 5.7. Conclusions of this chapter are provided in Section 5.8.

5.1. Introduction

Persistent scatterer interferometry (PSI) (Ferretti et al., 2001) is a geodetic technique to measure surface displacements using multi-epoch synthetic aperture radar (SAR) images. PSI estimates the displacement parameters from phase observations from selected coherent points, known as persistent scatterers (PS), with millimeter-level precision. Using advanced high-resolution SAR satellite systems, such as TerraSAR-X and COSMO-SkyMed, this technology can be used to monitor individual structures (Perissin et al.,

Parts of this chapter have been published in *IEEE Transactions on Geoscience and Remote Sensing* ((Yang et al., 2019a).)

2012; Zhu and Shahzad, 2014; Montazeri et al., 2016; Chang et al., 2017; Qin et al., 2017).

However, PS differ from traditional well-defined geodetic benchmarks. It is not that clear whether the observed signal stems from one dominant reflector, like a corner reflector, or from the effective summation of several reflectors within the resolution cell. Moreover, even if the PS is one dominant reflector, its precise localization remains a challenging task. Obviously, the capability to link PS to (locations on) particular objects would enhance PSI analyses, for example by reducing the uncertainty in the interpretation of the observed displacements in relation to specific driving mechanisms.

The relevance of establishing a one-to-one link between PS and specific objects is most obvious when there are different driving mechanisms involved. For example, points may represent deep and/or shallow deformation, e.g., due to gas production and groundwater level changes, respectively. Consequently, nearby PS may show different deformation signal. In other cases different parts of a building or infrastructure may deform differently, which may be a precursor of a partial or full collapse of the structure. In these complex scenarios, linking PS to the objects in the built environment would not only help identifying the local deformation in the object, but also facilitate the interpretation of the deformation signal.

Using the precise geolocalization of each PS seems to be the most straightforward approach to link the scatterer to an object. In fact, the geolocalization accuracy of PS for high-res (meter-resolution) SAR data is shown to be centimeters in azimuth and range (Eineder et al., 2011), and several dm up to 1.8 m for cross-range (Gernhardt et al., 2015). This positioning uncertainty can be described with a variance-covariance matrix and visualized with an error ellipsoid (Dheenathayalan et al., 2016, 2018). This way, the relatively poor cross-range precision of radar scatterers could be improved by intersecting the scaled error ellipsoid with 3D models (Dheenathayalan et al., 2016, 2018). Alternatively, an improvement of positioning precision could be obtained by using SAR data from different viewing geometries (Gisinger et al., 2015; Zhu et al., 2016), albeit only for a selected number of targets, such as lamp posts.

Yet, these methods all consider only the *geometry* of the problem, and are not based on physical scattering mechanisms. Consequently, the estimated positions may be geometrically optimal, but physically unrealistic. For example, for a perfect corner reflector, it is known that the effective scattering center is at the apex of the reflector, even though the pure geometric position estimate may turn out to be at a different position. As a result, understanding the *physical* scattering mechanisms may help in the realistic physical positioning of scatterers.

Physical understanding of scattering mechanisms can be supported by SAR simulation methods. However, this requires, at the least, a 3D geometrical representation of the scene (i.e. a 3D city model) (Schunert and Soergel, 2016). If this 3D representation is realistic with sufficient detail, the observed SAR scene should be very similar to the simulated one. Subsequently, if there is sufficient similarity, we will know which scattering mechanism produced the observed scatterers, and understand what caused the observed displacements.

A list of current SAR simulators includes, but is not limited to, SARAS (Franceschetti et al., 1992, 1998), Pol-SARAS (Martino et al., 2018), CAS (Huang et al., 1997), Xpatch 4 (Andersh et al., 2000), GRECOSAR (Margarit et al., 2006), CohRaS (Hammer and Schulz,

2009), SARViz (Balz and Stilla, 2009), and RaySAR (Auer et al., 2010). SARAS and CAS are oriented to ocean applications and do not consider multiple scattering for complex targets (Franceschetti et al., 1992, 1998; Huang et al., 1997). Pol-SARAS is the polarimetric version of SARAS, and it allows the simulation of natural scenes (Martino et al., 2018). Xpatch 4 is an object-oriented version of Xpatch, which provides 0-D radar cross section, 1D range profile, 2D SAR image, and 3D scattering center signatures, based on the shooting and bouncing of rays, supported by parallel computation (Andersh et al., 2000). Xpatch has been widely used in studies of the vehicle, typically an airplane or a ground vehicle (Hazlett et al., 1995; Castelloe and Munson, 1997; Bhalla et al., 2005). GRECOSAR can generate polarimetric SAR (POLSAR) and polarimetric inverse SAR (POLISAR) images of complex targets, and is used extensively for vessel classification studies (Margarit et al., 2006). CohRaS is a SAR simulator based on ray tracing, mainly for small scenes with high resolution, and only supports geometries made up of convex polygons (Hammer and Schulz, 2009). SARViz is a SAR image simulation system which only simulates single and double bounce reflections and does not include coherent addition of multiple echos (Balz and Stilla, 2009). Finally, RaySAR is based on ray-tracing, oriented towards the simulation of salient features in SAR images (Auer, 2011; Auer et al., 2011; Auer and Gernhardt, 2017). Despite the natural limitations resulting from the ray-tracing approach, it has some key advantages that motivated its use for the research presented in this study: (i) it can handle an arbitrary number of bounces, (ii) it keeps track of individual scatterers, (iii) it provides their 3D location and bounce level; and (iv) it is computationally inexpensive, which allows the simulation of relatively large and complex urban scenes.

Here we investigate the potential for predicting the occurrence and location of SAR scatterers (i.e. potential PS) based on physical scattering mechanisms, using generic 3D city models. In particular, we analyze the influence of the *level of detail* (LOD) of these city models on this prediction. The LOD is a generic metric describing the degree of adherence of the dataset to its real-world counterpart (Biljecki et al., 2014). The chapter focuses on the urban environment, where we are limited by the short supply of high resolution 3D city models. We use the ray-tracing SAR simulator RaySAR (Auer et al., 2010) to predict the radar scattering by illuminating the 3D scene with a SAR sensor. The *rays* can follow multiple reflections within the object scene, yielding a collection of point-like multiple-bounce scatterers that represent potential PS candidates. Methodology of linking the predicted points to the measured PS from a stack of SAR images is developed. Predicted points helps the understanding of the physical scattering mechanism of PS.

5.2. The RaySAR simulator

Ray tracing is a rendering method used to create an image by following the path of a ray through a 3D model and simulating the reflections on the surfaces it encounters. Ray tracing is based on geometrical optics, which is valid for surfaces that are large and smooth relative to the wavelength. RaySAR is one of the several SAR data simulators based on ray tracing. It is built on the open source persistence of vision ray-tracer (POV-Ray) (Glassner, 1989), using the PoV-Ray basic algorithms for ray tracing, intersections tests between rays and objects, the estimation of intensities, and shadow calculations (Auer et al., 2010).

RaySAR generates a set of scattering centers positioned in 3D SAR coordinates, i.e., azimuth, range, and cross-range. RaySAR subsequently projects and interpolates these scatterers on the 2D range-azimuth grid, adding the different contributions coherently in order to generate a simulated SAR image. In this research, however, we are mostly interested in the intermediate set of individual scatterers.

The set of scattering centers is provided by RaySAR as a list of signal vectors V :

$$V = [a_i \ r_i \ c_i \ I \ b \ f \ X_i \ Y_i \ Z_i] \quad (5.1)$$

where

- $[a_i \ r_i \ c_i]$ gives the position of the scattering phase center in azimuth, range, and cross-range,
- I is a relative intensity normalized between 0 to 1,
- b specifies the number of bounces (trace level),
- f is a boolean indicating specular reflection [0 or 1],
- $[X_i \ Y_i \ Z_i]$ are the coordinates of intersection points in the model.

The signal vectors V are referred to as contributing signal. These signal vectors are the basis for the simulated image generation and point scatterer identification.

Fig. 5.1 sketches the localization of the phase-center of a radar echo by RaySAR for a double bounce signal. Starting from the virtual sensor plane, a primary ray for each pixel is followed along its path until intersection with the modeled scene is found. At the intersection point, a reflected ray is spawned in the specular direction, and traced until the next intersection with the model, and so on. The azimuth, cross-range and range coordinates of the double-bounce signal are given by

$$\begin{aligned} a_i &= \frac{a_1 + a_2}{2} \\ c_i &= \frac{c_1 + c_2}{2} \\ r_i &= \frac{r_1 + r_2 + r_3}{2}. \end{aligned} \quad (5.2)$$

The trace level is the number of bounces of the signal. The maximum tracing level of RaySAR is five bounces.

The intensities of signal are calculated by a diffuse or specular radiometry model. For direct backscattering, the diffuse signal I_d is derived by (Glassner, 1989)

$$I_d = F_d \cdot I_c \cdot (\vec{N} \cdot \vec{L}), \quad (5.3)$$

where F_d is the diffuse coefficient [0 - 1], I_c is the incoming normalized radar signal [0 - 1], \vec{N} is the surface normal vector, and \vec{L} is the normalized vector from the object to the virtual sensor. The specular backscattering signal I_s is derived by (Glassner, 1989)

$$I_s = F_s \cdot (\vec{N} \cdot \vec{H})^{\frac{1}{F_r}}, \quad (5.4)$$

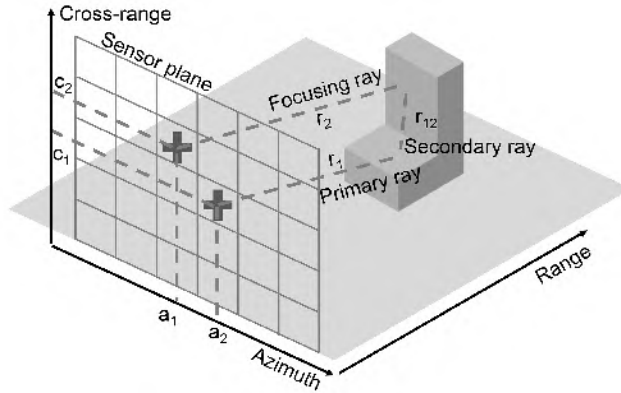


Figure 5.1: Sketch of how RaySAR localizes a double bounce signal and projects it in the sensor plane.

where F_s is the specular coefficient [0 - 1], F_r is the roughness factors [0 - 1], and \vec{H} is a bisection vector defined by \vec{N} , and \vec{L} . The discussion on the salient signal mainly focuses on the specular signal. The parameters F_d , F_r , and F_r are discussed in detail in Section 5.2.2

The contributing signal is the basis of simulated image generation and point scatterer detection. RaySAR offers a SAR reflective map in two steps. The first step is to obtain the contributing signal. Then a reflective map is derived by imposing and summarizing the contributing signal vectors within the corresponding pixel grids. The signal detected by POV-Ray depends on (i) the imaging geometry with respect to the illuminated object, (ii) the combination of diffuse and specular coefficients, and (iii) weight factors scaling the intensity of multiple reflections. The following section presents the point scatterer detection with RaySAR.

5.2.1. Point scatterer simulation with RaySAR

Potential PS candidates (simulated Point Scatterers) are selected from the contributing signal. These are points with specular multiple scattering characteristics ($I > 0$, $b > 1$, and $f = 1$). The selection criteria are based on the premise that many PS are physically associated with multiple specular reflections of the radar signal on relatively large surfaces. In the case of single bounce case, the location in the object geometry is directly provided by the intersection points in the model $[X_i Y_i Z_i]$. Due to the multiple bounces, the link of the signal to the object geometry is partly lost. In the case of a double-bounce signal, the corresponding location of the signal is on the adjacent lines between building façade and ground. Thus, calculation of the location of a multiple-bounce signal in the object geometry involves a coordinate transformation, from the imaging geometry to the world coordinate system. Fig. 5.2 describes a double bounce signal in two coordinate systems, sensor coordinate space and local geographic coordinate space.

The transformation includes two rotations and one shift. The look angle of the satellite and the aspect angle with respect to the north direction contribute to the two rotations. Supposing a signal with $\vec{r}_i = [a_i r_i c_i]$, \vec{v}_n is the nadir direction, the rotation vector

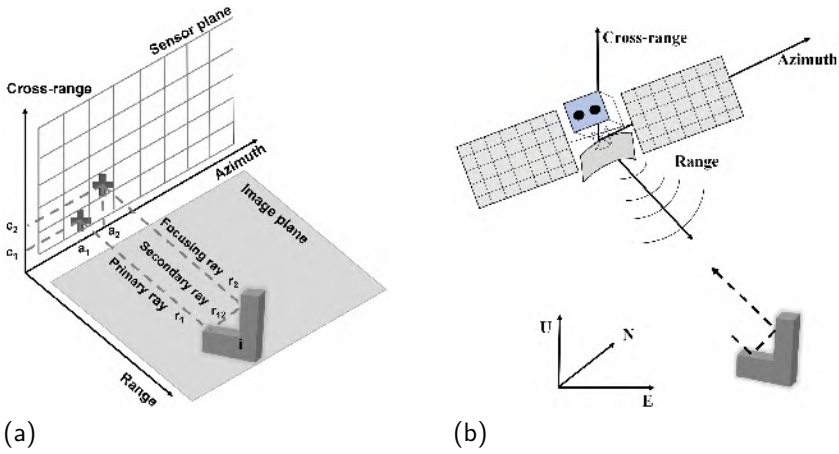


Figure 5.2: Two coordinate systems for a double signal, (a) simulated sensor coordinate space, including Azimuth, Range, and Cross-range directions; (b) world coordinate space, including north, east, and up directions.

5

is

$$T = \begin{bmatrix} \arccos(\vec{r}_i \cdot \vec{v}_n) - \frac{\pi}{2} \\ 0 \\ -\arctan\left(\frac{a_i}{r_i}\right) \end{bmatrix}. \quad (5.5)$$

The shifting is from the sensor position to the position in the world system. Therefore, we built the link of point scatterers to the object model.

5.2.2. Definition of a 3D scene for RaySAR

The input to RaySAR is a 3D scene model including the virtual signal transceiver and the 3D object model with the surface defined based on scattering characteristics. The contributing signal is generated according to the defined 3D scene model. The construction of the 3D scene model is introduced by three parts, (i) a virtual SAR system, (ii) 3D building models, and (iii) surface parameters.

Virtual SAR system

The virtual SAR system is described by the observation geometry and the system resolution. The geometry is defined using an orthographic projection and a parallel ray approximation. This parallel ray approximation makes the observation geometry azimuth invariant, as it should. However, it also makes the geometry elevation (hence range) invariant, which is not entirely correct. We will, nevertheless, assume that this approximation is good enough for a small scene. Thus, the observation geometry is defined by an incidence angle and an azimuth angle with respect to the scene, which have to be specified in RaySAR as the position of the sensor with respect to the center of the scene.

3D scene model

A 3D building model is the digital representation of an object in 3D space using a group of points connected by various geometric entities including lines, surfaces, etc. The acquisition of 3D models can be constructed directly with a text editor or software which

Table 5.1: Surface parameters for describing the scattering properties of the scattering surfaces in the 3D model.

Parameters		Impact on Radar Scattering
Weight	F_w	Weights the specularly reflected signal on a surface (loss of signal strength) of multiple reflections and works with a specular coefficient.
Specular	F_s	Resembles specular reflection and provides a spreading of the highlights occurring near the object horizons.
Roughness	F_r	Defines the width of a cone where a specular highlight occurs from 1 (very rough) to 0 (very smooth).

can assist in visual controlled modeling (e.g., CAD). Importing available 3D models into the POV-Ray format is another option considering there are a lot of city models available.

The 3D object model has to provide sufficient geometric detail for SAR simulation. The amount of detail and spatial resolution of a 3D city model are specified as LOD, denoting the abstraction level of a model as opposed to the real world object (Biljecki et al., 2014). The LODs have been described by CityGML (Open Geospatial Consortium, 2012), a prominent standard for the storage and exchange of 3D city models. LOD1 is a model in which buildings are represented as blocks, usually obtained by extruding their footprint to a uniform height. LOD2 is a more detailed model including roof shapes (Open Geospatial Consortium, 2012; Biljecki et al., 2016). As with many other applications of 3D city models (Biljecki et al., 2018), it is to be expected that the LOD and quality of the used 3D model will have an influence on the performance of the simulation of radar signal, a topic which we investigate in Section 5.3.

Surface parameters

The scattering properties of the scattering surfaces in the 3D model are specified by the parameters described in Tab. 5.1. The first parameter, F_w , controls multiple scattering by setting the fraction of the ray intensity that is specularly reflected. Thus, setting $F_w = 0$ will completely suppress multiple scattering.

The second parameter, F_s , controls the relative intensity of the first reflection, counting from the illumination source. The roughness parameter, F_r , controls the angular width of the first reflection. Values of low roughness and medium roughness surfaces are given in Tab. 5.2 based on a constant relative permittivity of $5.7 + j \cdot 1.3$ for man-made objects (Auer et al., 2010).

Fig. 5.3 shows four images simulated with varying (F_w, F_s, F_r) values according to Tab. 5.2. The parameter F_r works with specular coefficient F_s , see Figs. 5.3a and 5.3b. With increasing roughness, the number of features seen in the simulated images increases. Figs. 5.3c and 5.3d illustrate the results of a combination of three parameters. With the weight factor F_w , the strength of multi-scattering is clearly described. The intensity of a multi-reflected signal is weighted with F_w . In this case, we use the medium roughness $F_w = 0.5$, $F_s = 0.5$, $F_r = 3.3 \cdot 10^{-3}$. Compared to low roughness parameter

Table 5.2: Reference values of surface parameters for describing the scattering properties based on a constant relative permittivity of $5.7 + j \cdot 1.3$ for man-made objects.

Parameters		Value range	Value for low roughness	Value for medium roughness
Weight	F_w	0–1	0.7	0.5
Specular	F_s	0–1	0.7	0.5
Roughness	F_r	0–1	$8.5 \cdot 10^{-4}$	$3.3 \cdot 10^{-3}$

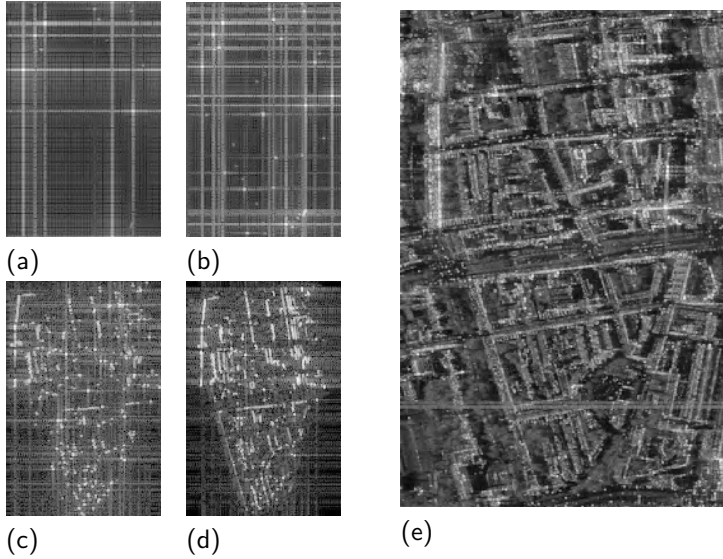


Figure 5.3: Surface parameters influence on SAR image simulation, (a) image with $F_w = 0$, $F_s = 0.7$, $F_r = 8.5 \cdot 10^{-4}$, (b) image with $F_w = 0$, $F_s = 0.5$, $F_r = 3.3 \cdot 10^{-3}$, (c) image with $F_w = 0.7$, $F_s = 0.7$, $F_r = 8.5 \cdot 10^{-4}$, (d) image with $F_w = 0.5$, $F_s = 0.5$, $F_r = 3.3 \cdot 10^{-3}$, (e) Mean intensity map of 49 TerraSAR-X images.

setting, medium roughness parameters are closer to reality using the X-band data, see Fig. 5.3e. It is important to emphasize that the phase-center location of the simulated scatterers does not depend of the surface parameters. Below, we focus solely on the phase-center location of multiple-bounce simulated PS.

5.3. Influence of Level-of-Detail models on simulation

The amount of detail and the spatial resolution of a 3D city model are specified by the LOD, denoting the abstraction level of a model as opposed to the real world object (Biljecki et al., 2014). For the simulation, objects are represented in different levels of detail, enabling an analysis of the objects in different resolutions. It is expected that the LOD and the quality of the used 3D model will influence how realistic the simulation of the radar signal will be. In this section, we use different LOD models of the same objects to simulate the signal and discuss their influence on the simulation.

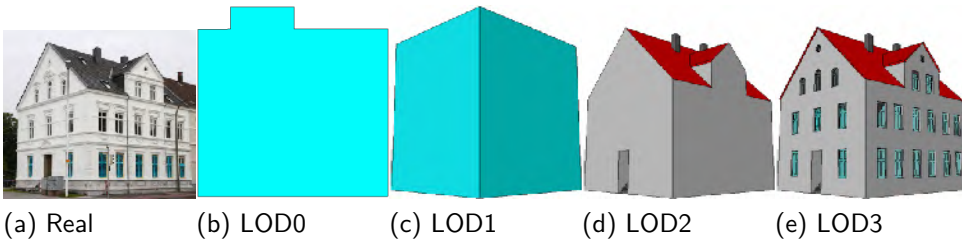


Figure 5.4: Representation of a building with LOD0, LOD1, LOD2, and LOD3 (Open Geospatial Consortium, 2012).

5.3.1. The definition of LOD

The LOD has been described by CityGML 2.0 (Open Geospatial Consortium, 2012), a prominent standard for the storage and exchange of 3D city models. Five LOD levels are defined in the standard. A higher LOD denotes a higher geometric and semantic complexity. Fig. 5.4 shows an object represented by four models with increasing LOD.

LOD0 is a model in which buildings are represented by their horizontal footprint (ground plane). LOD1 is a model in which buildings are represented as blocks (usually obtained by extruding their footprint to a uniform height). LOD2 is a more detailed model including roof shapes. LOD3 is an architectural model with detailed small structures including doors and windows. Models with LOD4 complete an LOD3 model with interior structures (Open Geospatial Consortium, 2012; Biljecki et al., 2016), and are consequently not relevant for SAR radio waves.

5.3.2. Simulation with varying LOD models

According to the definition of LOD, LOD0 only describes the footprint of the object, and LOD4 does not provide any additional exterior information compared to LOD3. Thus, LOD0 and LOD4 will not be employed for signal simulation. A building represented with LOD1, LOD2 and LOD3 models is used for simulation, see Fig. 5.5. The length, width, and height of the building in this figure are 12 m, 6 m, and 9 m, respectively. This building is used to discuss the influence of the LOD model on the simulation result. We suppose the sensor is viewing the object as in Fig. 5.5, with a flight trajectory which is 45 degrees from the orientation of the building.

The simulation settings include 0.5 m of posting, a look angle of 35 degrees, 1 m resolution, and maximally 5 tracing levels. Reflective maps are generated based on the varying LOD models, see Fig. 5.6a. The signals between the ground and the building wall depict the shape of the building. The presence of a roof brings the resulting shape in LOD2 result closer to that of LOD3. The intensity is increased from the map of LOD1 to LOD3. In the reflectivity map of the LOD3 model, a strong signal was detected from the structures of the windows.

Differential maps and coherence maps are generated by comparison of each result to the result of the LOD3 model. As assumed, the differences between the results from the LOD1 and the LOD3 model are greater than the differences between the results based on the LOD2 and the LOD3 model. The coherence map also confirms this result.

The influence of the level of detail in the 3D models on the results of the simulation

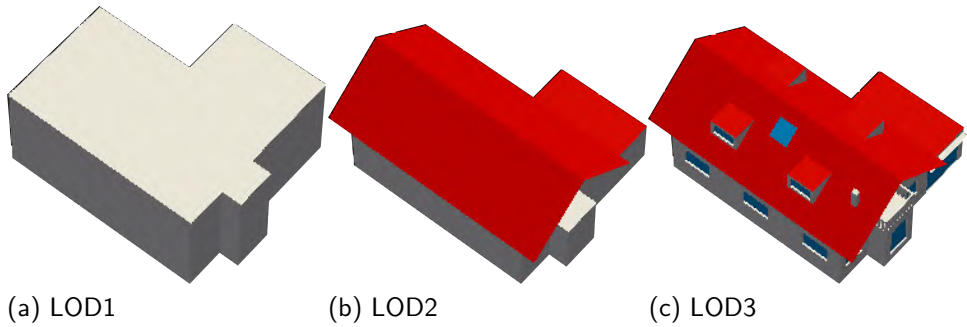


Figure 5.5: A building represented in LOD1, LOD2, and LOD3 model. These models were used for analyzing the influence of geometric details of a 3D model on simulation results.

is evaluated with the total power and total coherence. As highly coherent strong scattering points increase the power, the incremental power indicates more effective points. The strongest difference came from the trihedral signal in the corner of the window frame. The total coherence with respect to LOD3 denotes the similarity between LOD1 and LOD3 is very low (about 0.2).

Fig. 5.7 shows the total power of the detected signal from the LOD models. Increasing the LOD of the model from LOD1 to LOD2 results in 3495 more contributing signals, which is a 15-fold increase of the total power. Increasing the LOD from LOD2 to LOD3 only yields an increase of 743 more contributing signals, but giving a total power around 4 times stronger. As shown in Fig. 5.6, the growth of power is due to multiple scattering from detailed structures such as windows. From LOD1 to LOD2, the total coherence goes from 0.29 to 0.56. The result of LOD2 is about 60% similar to the result of LOD3, but has a big difference in the signal strength.

Obviously, buildings in LOD3 models are closer to reality, which provides the best choice for simulation. Even though it only gives a marginal improvement in the number of contributing signals comparing to the result of LOD2, but it provides the stronger point signal. However, it is much more difficult to obtain suitable LOD3 models for a particular area of interest.

Here we produce simulations with varying resolutions by applying a filter. Fig 5.8 shows a set of reflectivity maps based on the LOD3 model with six settings, 1×1 m, 3×3 m, 5×5 m, 10×10 m, 4×20 m, and 20×20 m. The small structures in the LOD3 model, such as the window frame, yield strong signals. These signals are obvious even in low-resolution images. From this point of view, LOD3 gives the best result.

Additional to the geometrical detail of the model, many other factors need to be taken into consideration, such as the size of the object relative to the resolution of the sensor, the viewing geometry of the sensor, and the material of the target. In a city view, LOD2 is probably the choice of compromise, based on the combination of performance, availability, and cost. This implies that the requirements on the geometrical level of detail should be assessed specifically for each particular application.

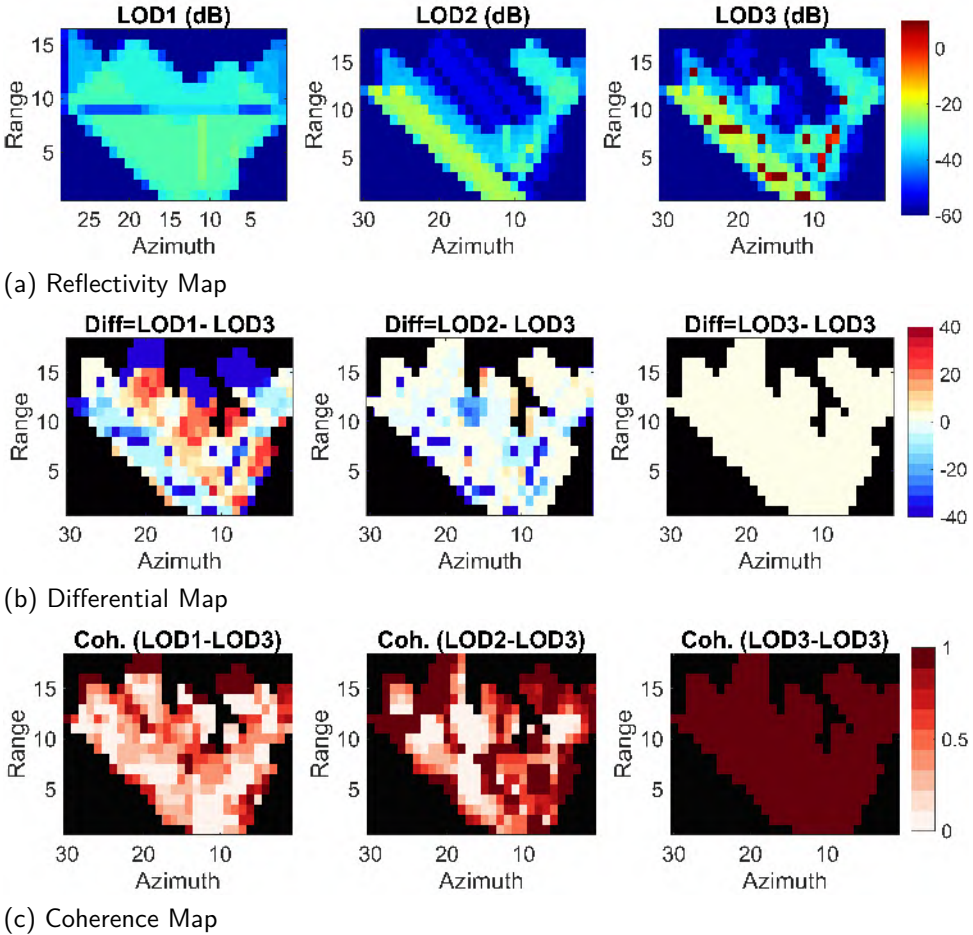


Figure 5.6: (a) Reflectivity maps generated based on the LOD1, LOD2, and LOD3 models of the same building. (b) Differential maps of reflectivity and (c) coherence maps are generated by comparison of each result to the result based on the LOD3 model. The differential maps and coherence maps are calculated with a mask indicating no echo signal area in LOD3 result.

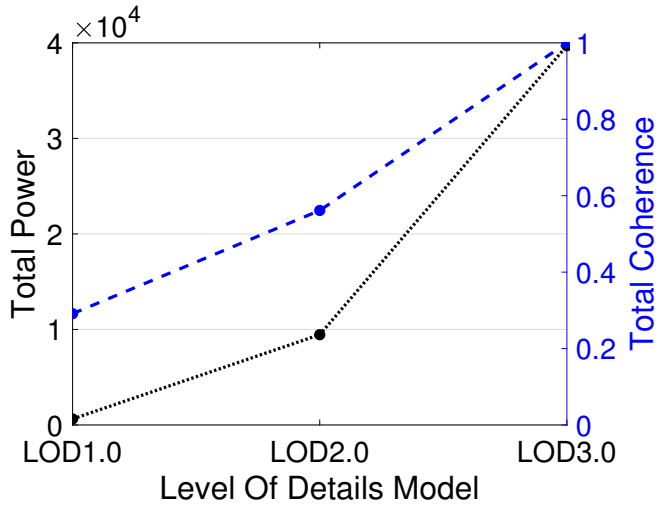


Figure 5.7: The number of contributing signals detected from LOD models of the same building.

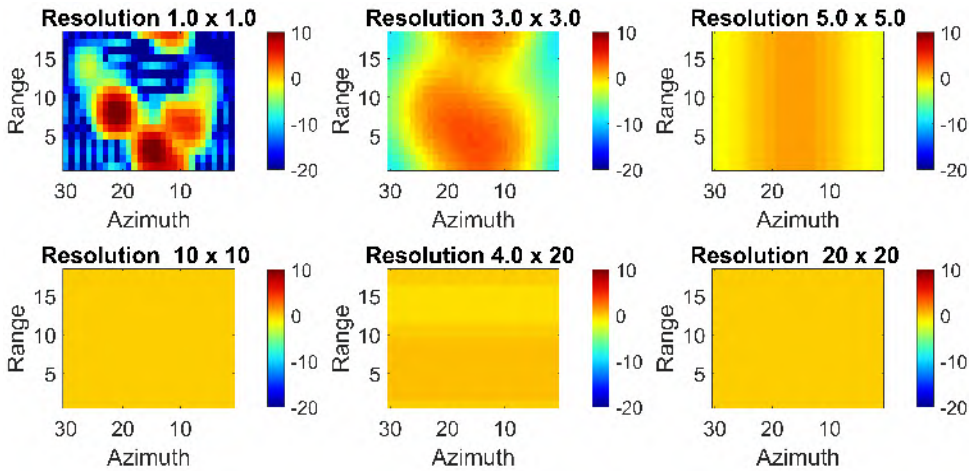


Figure 5.8: Reflectivity map based on an LOD3 model with varying resolutions. The resolution of the virtual sensor is increasing from 1 m to 20 m.

5.4. Linking persistent scatterers to an urban model

5.4.1. Methodology

One of the main steps in the work presented is matching of the simulated point scatterers (SPS) with the PS identified in the InSAR time series. The matching is done by evaluating the weighted Euclidean distances between the positions of the simulated point-scatterers and the positions of the PS. The weighting reflects the 3D position error ellipsoids, as defined by the positioning Variance-Covariance (VC) matrices, of the PS (Dheenathayalan et al., 2016).

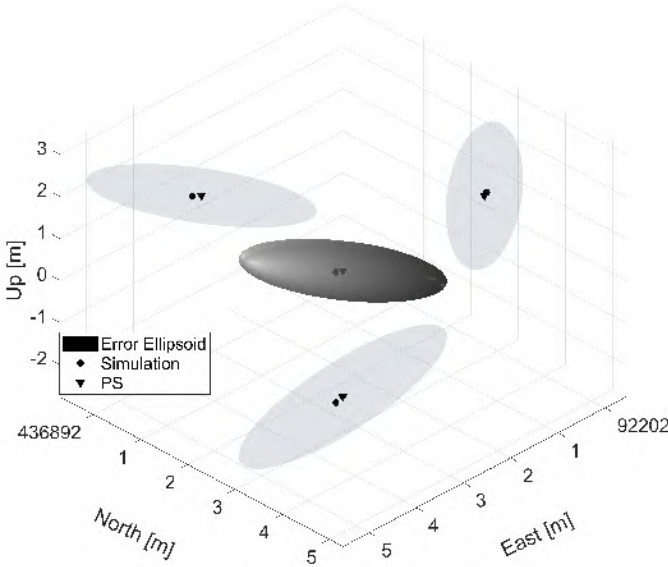


Figure 5.9: An example of finding the corresponding simulation point of a PS based on the 3D error ellipsoid. The estimated position of the PS is indicated by a black triangle. A cigar-shaped error ellipsoid with a ratio of axis lengths 1/2/35 (with $\sigma_r = 0.019$ m) illustrates the PS position uncertainty. The corresponding SPS is located inside of the error ellipsoid and indicated by a black dot. The ellipsoid and PS are projected in east-north, north-up, and up-east planes to illustrate their intersection with the SPS.

For each PS, the positioning uncertainty in the local reference frame (east, north, and up/height) \mathbf{Q}_{enh} is given by

$$\mathbf{Q}_{enh} = \mathbf{R}_{3 \times 3} \cdot \mathbf{Q}_{rac} \cdot \mathbf{R}_{3 \times 3}^T = \begin{bmatrix} \sigma_e^2 & \sigma_{en}^2 & \sigma_{eh}^2 \\ \sigma_{en}^2 & \sigma_n^2 & \sigma_{nh}^2 \\ \sigma_{eh}^2 & \sigma_{nh}^2 & \sigma_h^2 \end{bmatrix}, \quad (5.6)$$

where \mathbf{R} is the rotation matrix from radar geometry to local reference frame, \mathbf{Q}_{rac} the positioning VC matrix in 3D radar geometry with diagonal component variances ($\sigma_r^2, \sigma_a^2, \sigma_c^2$) in range, azimuth and cross range, the diagonal ($\sigma_e^2, \sigma_n^2, \sigma_h^2$) and non-diagonal ($\sigma_{en}^2, \sigma_{eh}^2, \sigma_{nh}^2$) are the variances and covariances in east, north and up coordinates. For each PS, from the eigenvalues of \mathbf{Q}_{enh} , a 3D error ellipsoid is drawn with the estimated position as its center. The semi-axis lengths of the ellipsoid are described by the eigenvalues of \mathbf{Q}_{enh} ,

which are $\sigma_r^2, \sigma_a^2, \sigma_c^2$. The shape of ellipsoid is derived from the ratio of their axis lengths, given by $(1/\gamma_1 / \gamma_2)$, where $\gamma_1 = \sigma_a \cdot \sigma_r^{-1}$, and $\gamma_2 = \sigma_c \cdot \sigma_r^{-1}$. The orientation of the ellipsoid is dependent on the local incidence angle of the radar beam at the PS.

Fig. 5.9 illustrates the matching of an SPS with a PS based on the 3D error ellipsoid. The position uncertainty of a PS is illustrated by the 3D error ellipsoid with 0.01 level of significance. The PS is matched to the corresponding SPS, which has to be inside the error ellipsoid.

As part of the matching process, it is necessary to remove potential systematic positioning errors. The systematic errors may be the result of an oversimplified geometry (e.g., the already mentioned range invariance), or errors in the knowledge of the acquisition SAR geometry.

A fine coregistration is performed using the iterative closest point (ICP) algorithm (Svirko et al., 2002; Chetverikov et al., 2005), which minimizes the sum of the weighted Euclidean distance between SPS and PS by least squares estimation (LSE) in an iterative way. Each iteration of the 3D error ellipsoid based ICP includes two steps: matching pairs of SPS and PS based on the 3D error ellipsoid; and finding the transformation that minimizes the weighted mean squared distance between pairs of points. The transformation results are applied to the point cloud of PS, thereby changing the correspondence.

5.4.2. Simulation assessment

Table 5.3: Confusion matrix \mathbf{M} for evaluating the matching between simulated point scatterer (SPS) and persistent scatterers (PS).

Total		SPS	
		Match	Non-Match
PS	Match	True positive rate (TPR) = $\frac{\sum TP}{\sum PS}$	False positive rate (FPR) = $\frac{\sum FP}{\sum SPS}$
	Non-Match	False negative rate (FNR) = $\frac{\sum FN}{\sum PS}$	

A quantitative evaluation of the matching between the detected PS and the simulated point scatterer (SPS) is given by the confusion matrix \mathbf{M} described in Tab. 5.3. Three performance ratios are considered:

- **True positive rate (TPR):** the ratio of the detected PS that match the SPS, with regard to the total number of PS.
- **False negative rate (FNR):** the ratio of the detected PS that have no match with an SPS, with regard to the total number of PS, also known as miss rate. For FNR, we have $FNR = 1 - TPR$.
- **False positive rate (FPR):** the ratio of the SPS that have not been matched, with regard to the total number of SPS.

Hereby, the metric **TPR** describes the matching ratio between simulation points and detected PS, and is the primary evaluation indicator of simulation scatterers. **FPR** is also

an important indicator for describing the ratio of redundant simulation points.

Note that the detected PS or SPS selection criteria will have an impact on the performance metrics. For example, a low amplitude dispersion threshold may lead to selecting less actual point-scatterers and lead to a higher FPR. Since the final goal of our research is to improve our capability to analyze deformation signal, we focus on the group of PS that are deemed reliable. PS are chosen with the an amplitude dispersion threshold set to 0.45 and further checked based on network phase consistency (van Leijen, 2014). Here, SPS are scatterers predicted by the simulator based on the geometry. Therefore, the final number of PS is less than the SPS from the simulator, because we eliminated many points during the PSI processing, which consequently increases the FPR.

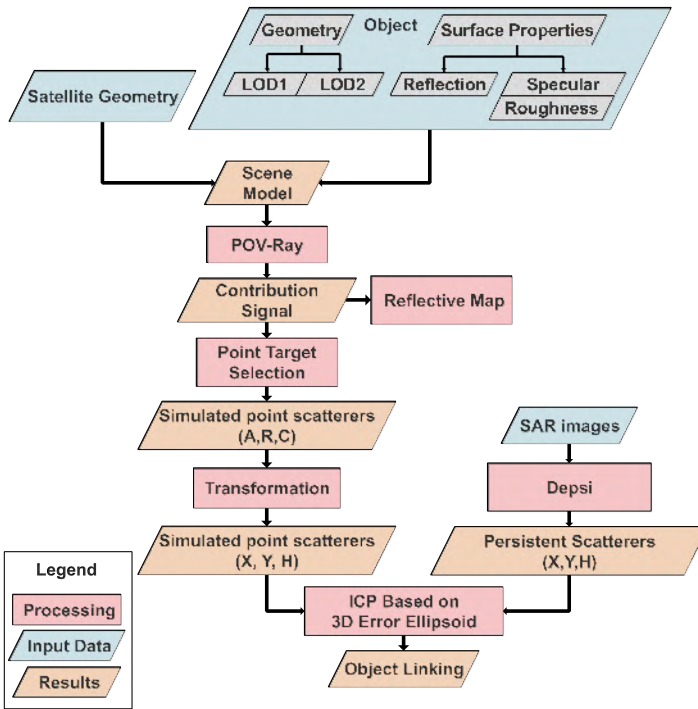


Figure 5.10: Schematic of the methodology for linking the PS to geo-objects using ray-tracing on 3D models.

5.4.3. Work-flow

The flowchart in Fig 5.10 outlines the work-flow of this method, which consists basically of three parts: generation of simulation points, detection of PS in real SAR images, and the matching of the two point cloud sets. The generation of simulation points consists of scene modeling, signal detection with Pov-Ray, and selection of PSPs. The SAR data-stack is processed with the Delft implementation of persistent scatterer interferometry (DePSI) (van Leijen, 2014), which is based on the Delft framework of geodetic esti-

mation, testing, and quality control. DePSI detects PS with consistent reflection properties over time as input for time series deformation and height estimation. Then, matching of two point cloud sets is carried by ICP based on the 3D error ellipsoid.

RaySAR is not demanding in terms of computational resources. It is built on POV-ray, an open source tool which traces rays in reverse direction. In this study, the calculation of 48 million contributing signal vectors took about 10 minutes on a 4-core workstation with 16 GB of RAM.

5.5. Experiments

5.5.1. Test site and data

The test area is located southeast of Rotterdam Central Station, the Netherlands. The size of the area of interest (AoI) is around $1 \times 0.5 \text{ km}^2$. We collected a data stack from TerraSAR-X.

Fig. 5.11a shows an overview of the test site, and its orientation with respect to the trajectory of TerraSAR-X. 49 TerraSAR-X strip-mode images are obtained from 19-Jan-2014 to 25-Feb-2017. Tab 5.4 gives the basic parameters of TerraSAR-X. Fig. 5.3e is the mean intensity map of 49 TerraSAR-X images over the AOI.

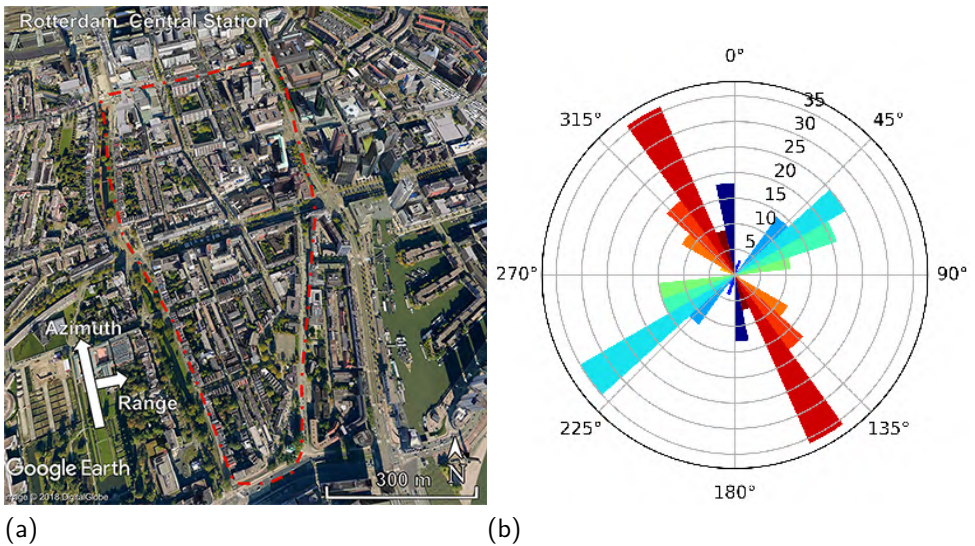


Figure 5.11: (a) Google Earth overview image of the test site, azimuth and range direction indicate the view of TerraSAR-X data, (b) Street orientation histogram of the area of interest. Each bar represents the compass bearing of the streets and its length indicates the frequency of streets with those bearings. There are two main directions at 336° and 60° .

Fig. 5.11b shows a polar histogram describing the orientation of the streets within the AOI calculated based on OpenStreetMap (Boeing, 2016). The direction of each bar represents the compass bearings of the streets and its length indicates the relative frequency of streets with those bearings. From Fig. 5.11b, two main orthogonal directions can be identified, one at about 336° (red bars), and another at about 60° (cyan).

Table 5.4: Basic parameters of TerraSAR-X data stack

Satellite/Parameter	TerraSAR-X
Track	T025
Band [cm]	X (3.1)
Start Date	2014.01.19
End Date	2017.02.14
Num. of images	49
Mode	Stripmap
Pass direction	Ascending
Polarization	HH
PRF [Hz]	3790
RSR [MHz]	109.8
Incidence angle [°]	39.3
Heading [°]	349.8
Slant range spacing[m]	1.36
Azimuth spacing [m]	1.86
Range Bandwidth [MHz]	100
Azimuth Bandwidth [Hz]	2765

In this research, the building model is reconstructed with 3Dfier (Labetski, 2017) by combining the large-scale topographic dataset of the Netherlands, BGT (*'Basisregistratie Grootchalige Topografie'* in Dutch) dataset and the laser altimetry, AHN3 (*'Actueel Hoogtebestand Nederland'* in Dutch) datasets.

Two 3D city models with different levels of detail (LOD) were employed to simulate scatterers using RaySAR. Fig. 5.12 displays the 3D models at LOD1 and LOD2 of the AoI. In the LOD1 model, buildings are represented as boxes with flat roof structures (Fig. 5.12b), opposed to buildings in LOD2 (Fig. 5.12c), which have differentiated roof structures with varying heights, providing a more realistic representation of the reality.

From the enlarged partial picture of the LOD1 model (Fig. 5.12b) and the LOD2 model (Fig. 5.12c), it is clear that buildings in LOD2 include many different parts with varying roof shapes and heights. Datasets with LOD1 and LOD2 are the most common instance in practice because it is possible to obtain them automatically, e.g., from LiDAR data by automatic building reconstruction (Biljecki et al., 2016).

5.5.2. PSI results

The topographic results of the PSI estimation with TerraSAR-X data are illustrated in Fig. 5.13a, 2290 points are selected as PS in the AoI. The results are projected in the Dutch National Reference system RD (*'Rijksdriehoeksstelsel'* in Dutch) and vertical system of the Amsterdam Ordnance Datum NAP (*'Normaal Amsterdams Peil'* in Dutch) reference system. The axes of Fig. 5.13a show X (RD) and Y (RD) in meters, in east and orth direction, respectively. The estimated heights are indicated by colors, showing some higher buildings in the northwest and northeast corner of the AoI, which can be found

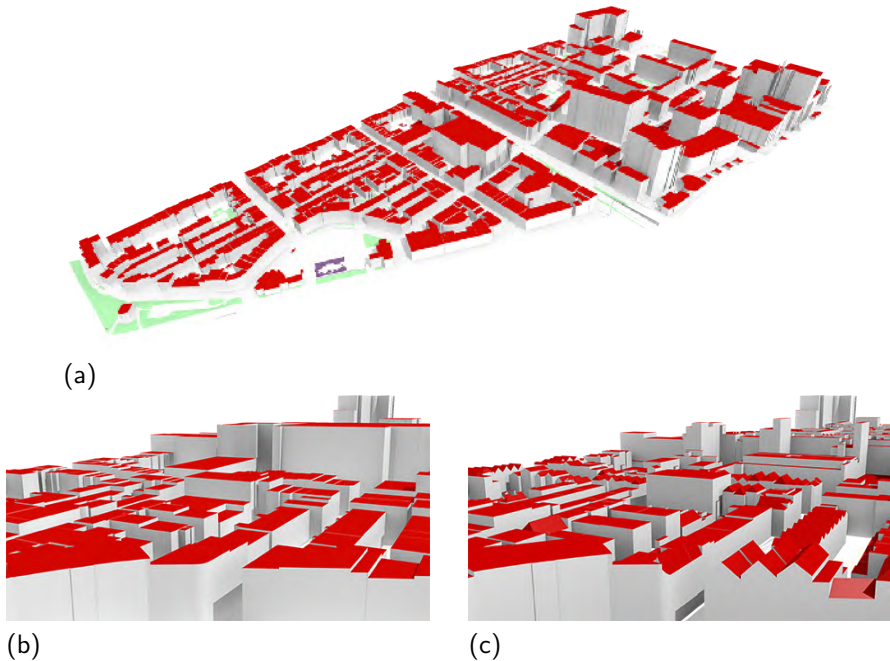


Figure 5.12: (a) Overview of the used 3D city model; (b) a closer look on the LOD1 variant of the dataset; and (c) its more detailed (LOD2) counterpart including roof shapes.

in Fig. 5.11a. The topographic map from AHN (Actueel Hoogtebestand Nederland) DSM data in AOI is plotted in Fig. 5.13b as a comparison. The topographic result of TerraSAR-X data agrees well with the topographic map of AHN.

5.6. Linking results: TerraSAR-X

In this section, we present the simulation point scatterers (SPS) based on LOD1 and LOD2 models, the linking results of the detected PS and the SPS, and validation of matching results.

5.6.1. Simulated point scatterer

POV-Ray/RaySAR detects all contributing signals within the AoI. The total number of received signals from the LOD1 and LOD2 models is about 50 million. We detect potential point scatterers, and consider these as signals that exhibit the characteristics of PS ($I > 0$, $b > 1$, and $f = 1$) from the contributing signal.

We identify 2770 potential point scatterers from the model at LOD1, as described in Section 5.2.1. Fig. 5.14a shows the distribution of simulated points in the LOD1 model. The colors indicate the height of simulation points. In comparison to the real radar results in Fig. 5.13a, the height values of the SPS are mainly below 15 m. The simulation points include 742 double bounces, 890 triple bounces, 590 fourfold bounces, and 548 five-fold bounces, see the pie chart in the upper-right of Fig. 5.14a. Most signals corre-

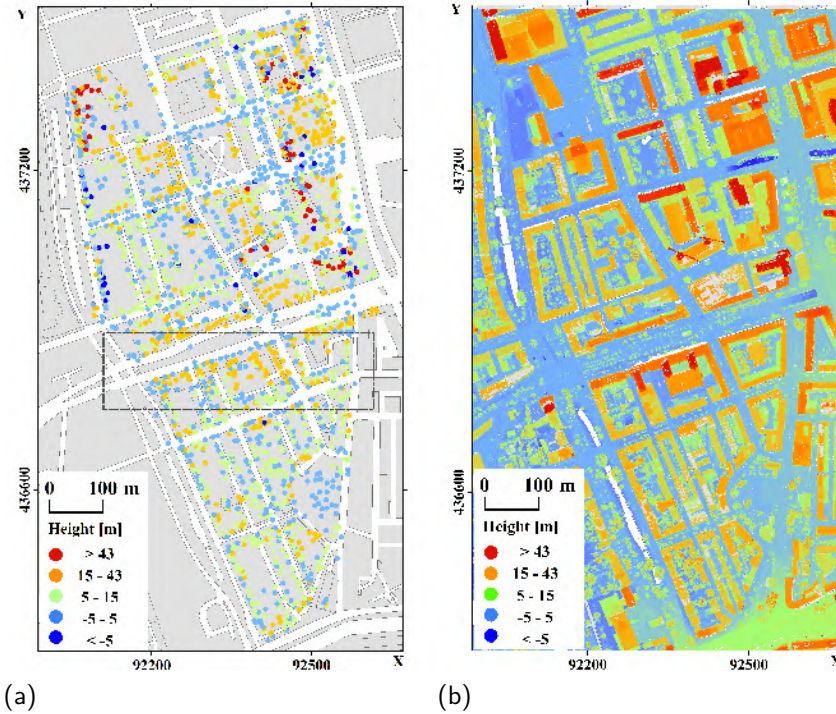


Figure 5.13: PS identified in (a) TerraSAR-X data stack overlaid on the TOP10NL map. TOP10NL is the digital topographic base file of the Land Registry, the most detailed product within the Basic Registration Topography (BRT). The colors indicate the estimated PS heights (blue-low; red-high). (b) Topographic map from AHN data.

spond to triple-bounce scatterers, followed by double-bounce ones.

Using the LOD2 model results in 4390 potential point scatterers, as illustrated in Fig. 5.14b. Compared to the real PS data, more points with greater heights are detected. The spatial distribution of the height values of SPS from the LOD2 model is similar to the measured PS, see Fig. 5.13a. PS with greater heights are clustered in the northeast corner of the test site, which is also predicted by the simulation. The height of simulation points in the northwest is lower than PS in Fig. 5.13a, because the buildings in the northwest corner are missed in the LOD2 model (equal to LOD1). The Google Earth image in Fig. 5.11a also indicates the new buildings in the northwest corner. Simulated points from the LOD2 model include 799 double bounce, 2267 triple bounce, 632 four-fold bounce and 692 five-fold bounce, see the pie chart in the upper-right of Fig. 5.14b. More than half of the points are triple bounces.

Fig. 5.15 gives the height profile of PS and SPS of LOD1 and LOD2, in the box indicated in Fig. 5.13a along the x -axis. The height profile of PS and SPS from LOD2 is similar, while the SPS from LOD1 missed points with greater height.

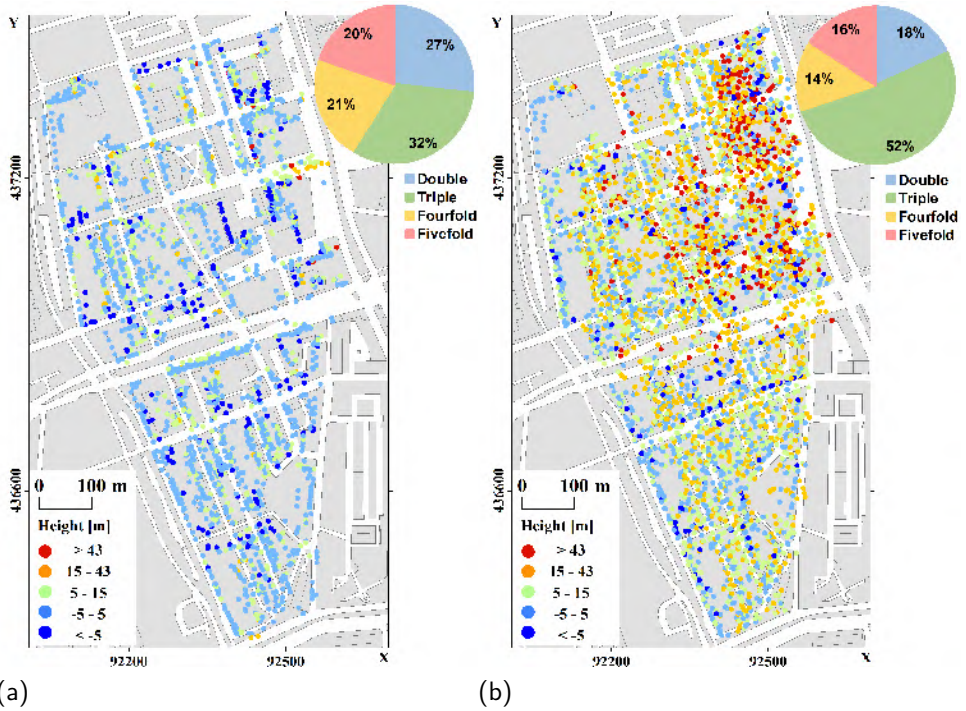


Figure 5.14: (a) Point scatterers simulated based on model of LOD1 with color represents height, (b) Point scatterers simulated based on model of LOD2 with color represents height. The background image is TOP10NL map.

5.6.2. Linking of PS and SPS

Following Section 5.4, PS (Fig. 5.13a) were matched to the point-scatterers predicted using the LOD1 (Fig. 5.14a) and LOD2 (Fig. 5.14b) models. Figs. 5.16a and 5.16b show the spatial distribution of PS and the corresponding SPS. The dark circles indicate the location of PS that have been matched to SPS. The dots represent the corresponding SPS, color-coded by bounce level (see legend on Figure).

Tab. 5.5 gives the confusion matrix between SPS based on LOD1 and LOD2 models and PS. Scatterers from the model of LOD1 predicted 10% PS correctly (correspondingly, around 90% PS were missed). 92% of the simulation points have not been matched by a PS. By using the LOD2 model, the amount of PS matched with simulated scatterers increased to 37%. Naturally, the number of predicted point-targets that did not match to PS also increased. However, it is noteworthy, that, in relative terms, the number of scatterers matched to PS grew much stronger than the overall amount of predicted scatterers. Moreover, the percentage of simulation points that have no match to a PS is decreased to 80%.

Fig. 5.17 provides a quantitative overview of the number of point-scatterers predicted for the LOD1 and LOD2 models, segregated by the bounce level. In each of the bars, it is also indicated which fraction of the SPS was matched to a PS. Not surprisingly, the

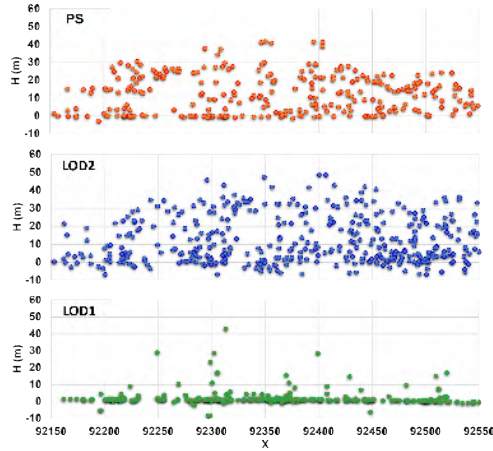


Figure 5.15: Height profile of (a) persistent scatterers (PS) measured from TerraSAR-X data and simulated point scatterer (SPS) from (b) LOD1 and (c) LOD2, in the box indicated in Fig. 5.13a along the x-axis.

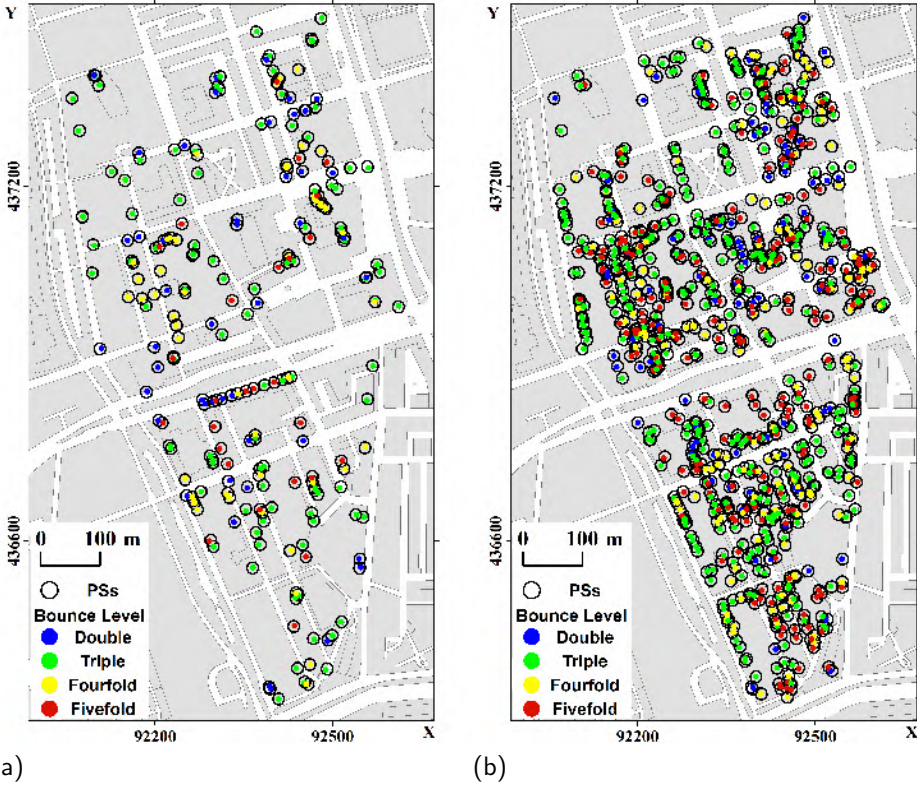


Figure 5.16: Correspondence between simulated point scatterers, shown as solid circles color-coded by bounce level, and matched PS, shown as empty circles. The left panel (a) and the right panel (b) correspond to simulations using the LOD1 and LOD2 models, respectively.

Table 5.5: Confusion matrix between measured persistent scatterers (PS) and simulated point scatterer (SPS) based on the LOD1 model and LOD2 model. Three metrics, true positive rate (TPR), false positive rate (FPR), and false negative rate (FNR), were used for evaluation.

	SPS-LOD1 (2770)		SPS-LOD2 (4390)	
	Match (223)	Non-Match (2547)	Match (842)	Non-Match (3548)
PS (2290)	TPR	FPR	TPR	FPR
	10%	92%	37%	80%
	FNR		FNR	
	90%		63%	

increase of the level of detail leads to a very strong growth (close to a factor 3) of the predicted triple-bounce scatterers. The fraction of predicted triple-bounce scatterers matched to actual PS increased from 11% to 16%.

5

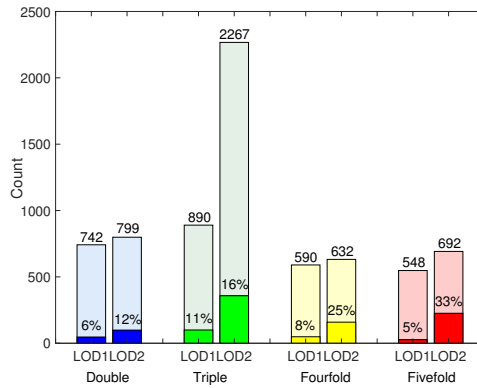


Figure 5.17: Histograms of simulation points from LOD1 model and LOD2 model in double, triple, fourfold and fivefold bounce. The X-axis is LOD1 and LOD2. The Y-axis is the count number from 0 to 2500. There were 742 and 799 double-bounce signals from the LOD1 and LOD2 models. Among these signal, 6% and 12% points were linked to the PS. Likewise, for triple-bounce signal, and fourfold-bounce signal and fivefold-bounce signal.

For the other bounce-levels considered, the increase of predicted scatterers was quite modest. However, the fraction of these scatterers that was matched to PS increased by a factor of two for double-bounce scatterers, a factor of three for fourfold bounce scatterers, and by more than a factor of six for fivefold-bounce scatterers.

The total number of matched scatterers increased from 223 in the LOD1 case and to 842 with the LOD2 model. Triple-bounce scatterers, 100 and 358, respectively, remained dominant. Finally, 226 of the LOD2 model scatterers, or about one-fourth of the total, corresponded to fivefold-bounce signal.

The number of predicted point-scatterers for the LOD1 (2770) and LOD2 (4390) models were larger than the number of detected PS. This can be explained by considering that PS selection is done based on the amplitude stability of individual resolution cells

in the interferometric data stack. Typically, the amplitude will be stable if a single point-like scatterer is a dominant factor in the radar echo for that resolution cell. Thus even if we know for sure that we have a stable point-like target within our resolution cell, as this does not exclude contributions from other scattering mechanisms, it does not imply that it will result in a PS. Moreover, as stated in section 5.4.2, the selection criterion also contributes to the fact that the number of simulation points was larger than the number of PS.

5.6.3. Target matching validation

A potential pitfall in the matching process is that if the local density of either PS or SPS is high, the amount of random matches increases as well (false positives). However, the amount of random matches should be insensitive to their exact position. Hence, while some pairs would be disassociated, roughly the same number is expected to appear.

Following this reasoning, we added random disturbances with Gaussian distribution to the coordinates of the simulated points and performed the PS matching, following the procedure discussed in Section 5.4. In order to consider the worst case, the random disturbances are aligned along the dominant orientation of the buildings. The x , y , and z coordinates of the simulated points with random disturbances are given by

$$\begin{aligned}\tilde{x}_{\text{sim}} &= x_{\text{sim}} + \Delta x \\ \tilde{y}_{\text{sim}} &= y_{\text{sim}} + \Delta y \\ \tilde{z}_{\text{sim}} &= z_{\text{sim}} + \Delta z,\end{aligned}\tag{5.7}$$

where x_{sim} , y_{sim} , and z_{sim} are the original coordinates of the simulated point scatterers, $\Delta x = n_1 \cdot \sin(t)$, $\Delta y = n_1 \cdot \cos(t)$, and $\Delta z = n_2$. The angle $t = 336^\circ$ is the main orientation angle of the streets and buildings as presented in Fig. 5.11b. n_1 and n_2 are zero-mean Gaussian-distributed random disturbances with a standard derivation of σ meter.

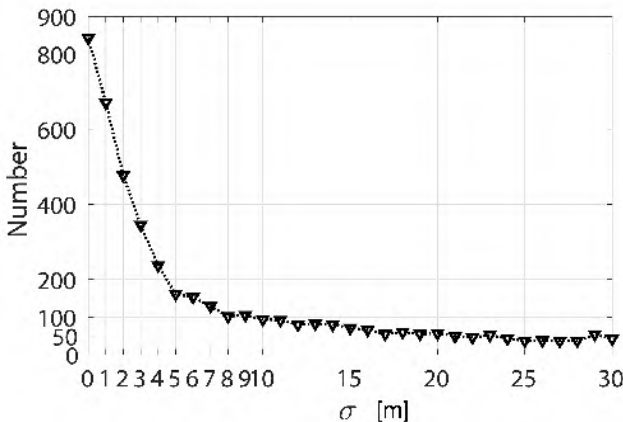


Figure 5.18: Number of matched PS as a function of the standard deviation of the disturbance added to the position of the simulated scatterers. The rapid decrease of matched pairs supports the assumption that the vast majority of matches is correct.

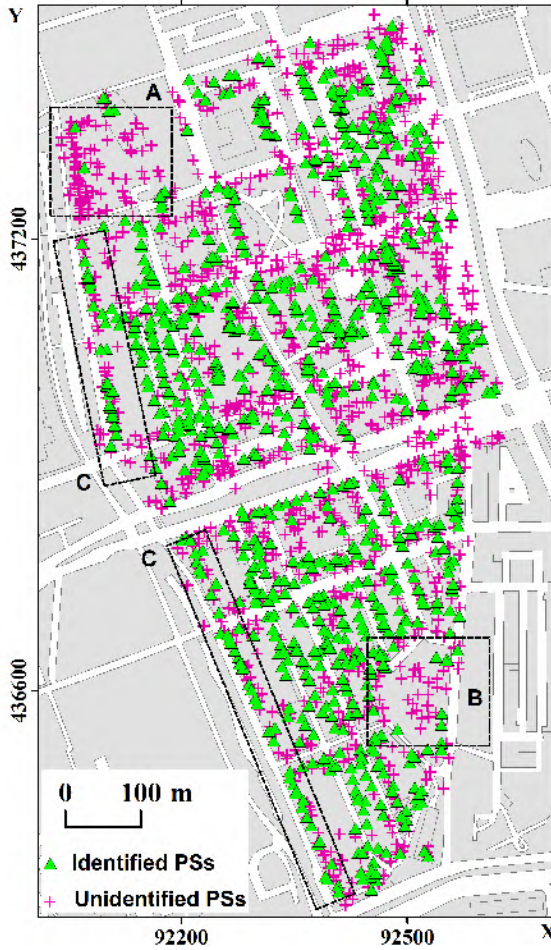


Figure 5.19: All PS detected in the area of interest, with identified PS represented by green triangles and unidentified PS indicated by magenta plus-signs. The A-labeled area corresponds to a new building absent in the LOD2 model. The B-labeled area corresponds to a green-area free of buildings, which is not included in the 3D model (no simulation points). The C-labeled areas are the examples of predicted PS at the linear structures of buildings and identified as triple bounce.

Fig. 5.18 shows the number of matched PS as a function of σ . The number of matched pairs decreases rapidly as the position disturbance σ increases. Introducing a position error with $\sigma = 4$ m, which is close to the spatial resolution of TerraSAR-X in stripmap mode, reduces the amount of matches by a factor of 4, while a further increase in the positioning error has only a limited effect on decreasing the amount of matches. As less than 10% of the number of matches remains if the positioning error is increased to an unrealistically high value, this analysis suggests that the vast majority of matched pairs are physically correct.

Fig. 5.19 shows all PS detected in the area of interest, with identified PS represented by green triangles and unidentified PS indicated by magenta plus-signs. The area labeled A, where most PS were missed by the simulation, correspond to a new building not present in the LOD2 model. Moreover, the building model did not include the public facilities, like the flower boxes in the area labeled B. Most predicted PS are located at linear structures of buildings and identified as triple bounce, such as the points in the area labeled C. Those scatterers originated from the roof and ghost corners e.g., the corner of the wall and the ground, which is in agreement with previous research (Auer and Gernhardt, 2017).

Simulation points have precise locations and precise location in the model. The object snap of PS can be achieved by the correlation of PS and SPS. Fig. 5.20 displays an overview of matched simulation points in the LOD2 model.



Figure 5.20: Rendering of matched scatterers overlaid on LOD2 city model.

5.7. Displacement signal for multiple bounce signals

A large number of point scatterers is detected from an urban scene, which originates from the buildings, structures, ground, and the interaction of these objects. The PSI technique estimates displacements from the phases of the point scatterers. Understanding the deformation mechanism behind the estimated displacements requires locating the point scatterers in the illuminated scene which has been discussed in the previous sections.

We have seen that multiple reflected signal are frequently observed in an urban scene since a majority of point scatterer correspond to multiple bounces. However, the influ-

ence of multiple bounces on the observed deformation signal has not been discussed yet. If the displacements are discussed without the consideration of the scattering characteristics of point scatterers, we might give a wrong interpretation of the deformation phenomenon.

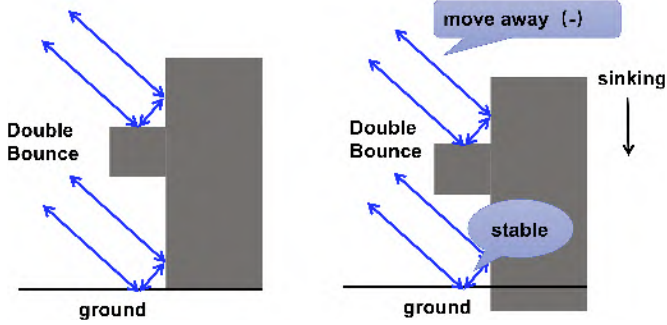


Figure 5.21: Two double bounce signals in a building, showing different displacement signal when the building is going down. The double bounce between the building wall and the ground in front of the building shows no variation on LOS measurement, while the double bounce at part of the building gives a subsiding signal.

Fig. 5.21 describes two double-bounce signals in a building. The measurement is the projection of the true deformation onto the line of sight (LOS). Suppose the building went down about 1 mm, the LOS measurement of a single bounce point will show a variation of $\cos\theta$, where θ is local incidence angle. The LOS measurement of the double bounce between the ground and the building wall will remain unchanged, while the double bounce formed at the building reveals the displacements of $\cos\theta$.

We show the same number of bounces might result in different displacement signal of a building in Fig. 5.21. A multiple-scattered signal (> 3) might make the situation more complicated. Fig. 5.22 shows a fourfold bounce signal between the ground and a building. When the building is going down, the propagation path of the signal will be shorter. That is, an uplift displacement is observed from the point scatterer.

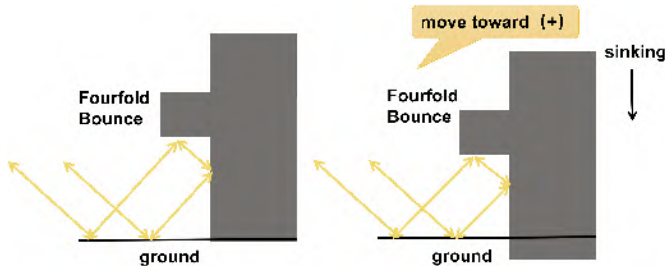


Figure 5.22: A fourfold bounce signal between the building and the ground. The fourfold bounce signal gives a downward displacement, which would be erroneously interpreted as an upward displacement.

Due to a long propagation path, the phase center of a multiple bounce signal is often geolocated below the ground, which is referred to as a ghost point. Multi-reflected points

cause an inverted reflection signal below ground, called the "mirror" effect, which could be seen at high-rise structures in many SAR images. Fig. 5.23 describes the mirror effect, and the ghost points will show opposite displacements when the object is sinking.

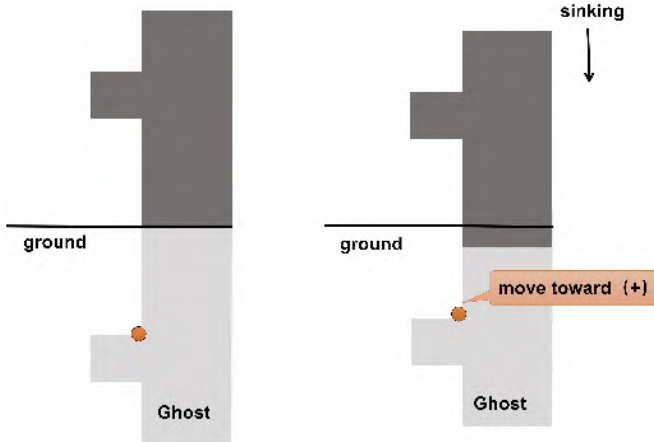


Figure 5.23: The multiple bounce signal results in an inverted reflection signal, i.e., the mirror effect. When the building is sinking, the ghost point shows the opposite displacement.

5.7.1. Setting up of a simulated displacement event

We designed a virtual displacement event on a building and simulated the detected point scatterers on that building, to further illustrate the relation between observed displacements on multi-reflected signals and the real displacements. Fig. 5.24 exhibits the simulated scene, including a building model at LOD3 and a boundaryless ground. Supposing the flight trajectory is 45 degrees from the orientation of the building, the incidence angle is 35 degrees. The virtual displacement event assumes that a building went down 1.221 mm to the ground. The corresponding displacement projection along the LOS direction is 1 mm. Two observations were made before and after the virtual event. The point scatterers are detected to analyze the displacements measured along the range direction.

5.7.2. Simulated displacements interpretation

The intensity maps of the target building are shown in Fig. 5.25. The intensity map is generated with a pixel size of 0.5 m and a resolution of 1 m in both azimuth and slant range direction. The signal between the wall of the building and ground formed the clear line of the building in the intensity map. The roof structure is closer to the sensor than the building wall and shows the layover in the intensity map. The strongly scattered signals in yellow are caused by the layover of the windows. The intensity map before and after the event are almost the same. The slight displacement is not reflected in the intensity map.

The potential point scatterers are detected with the feature of PS ($I > 0$, and $f = 1$). The displacements on the point scatterers are calculated by subtracting the range mea-

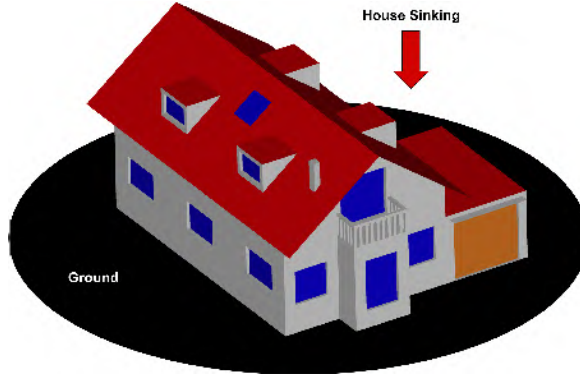


Figure 5.24: A building model at LOD3 is the observed target, and the simulated event is this building settled 1.221 mm into the ground, equivalent to 1 mm along LOS direction.

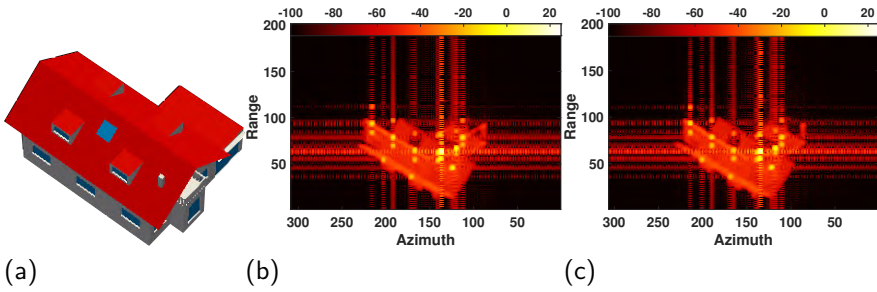


Figure 5.25: (a) Target building model at LOD3, (b) simulated intensity map before the sinking event, (c) simulated intensity map after the sinking event.

surement after the event from the range measurement before the event. If the target object moves away from the sensor, the length of the path increases, the sign of displacement is negative. On the contrary, the sign of the displacement is positive, if the target building moves towards the sensor. Fig. 5.26a gives the detected point scatterers on the building. We have detected 23 point scatterers on the building. Fig. 5.26b describes the bounce level of the 23 points. Fig. 5.26c shows the displacements of the 23 points.

The observed displacements of points, the location of points, and the bounce times are jointly analyzed.

- Triple bounce points 1 to 9 originate from the corners of the windows. The displacements of these points are -1 mm.
- Triple bounce points 10 to 16 form from the corner of the building and ground. No displacement is observed from these points.
- Fivefold bounces points 17 to 23, these points are ghost points, below the ground. The observed displacements of these points are $+1$ mm.

The points 1 – 9 located in the corners of the windows show the displacements as the actual magnitude of displacement. Their phase centers are subsiding with the house.

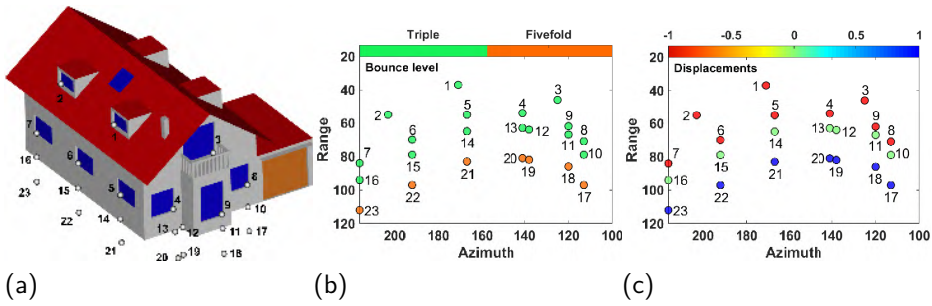


Figure 5.26: (a) Point scatterers located on the building model, points 17-23 are below the ground. (b) The bounce level of point scatterers, green dot indicate triple bounce, orange indicates fivefold bounce. (c) The LOS displacements of point scatterers are color code from -1 to 1 mm.

Conversely, the triple bounce points between the building and ground remain unchanged in terms of range measurement, see points 10 – 16. There is no change in the phase centers of those points. Due to the long propagation paths, the fivefold bounce points 17 – 23 are geolocated below the ground. These fivefold signals were formed between the ground and the upper corner of the window. The observed displacement is opposed to the actual magnitude of displacement due to the mirror effect.

The second simulation is performed by rotating the house by 45 degrees. The double and fourfold bounce signals were generated in this viewing geometry. Fig. 5.27 shows the locations, the bounce levels, and the displacements of these detected points.

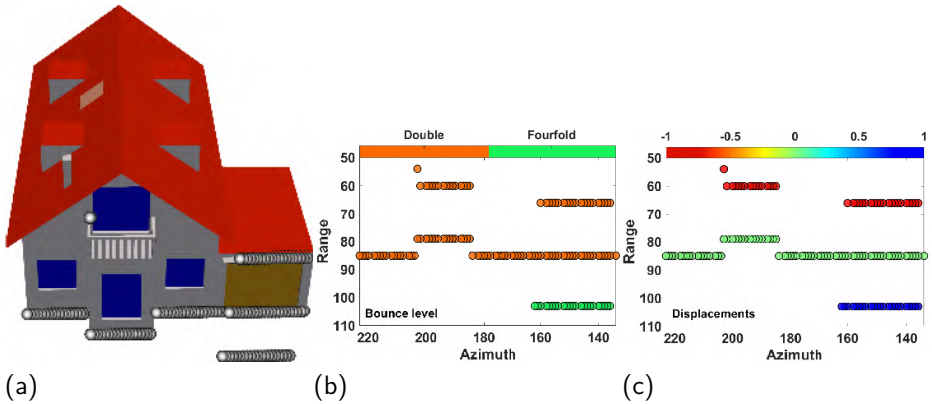


Figure 5.27: (a) Point scatterers located on the building model, points 17-23 are below the ground. (b) The bounce level of point scatterers, green dot indicate triple bounce, orange indicates fivefold bounce. (c) The LOS displacements of point scatterers are color code from -1 to 1 mm.

Stable double bounce points originate from the ground and the wall. The subsiding double bounce points are located in the house and change with the house. Conversely, the fourfold bounce points were showing uplift deformation. The fourfold bounce points were located below the ground, which were formed by the interaction between the ground and the eaves of the house.

In the simulation, we showed that point targets with different scattering numbers were detected in a single building. These point targets show different or even opposite displacements, compared to the displacements given by our design. Even points with the same scattering number may have different displacements. It all depends on where the scattered signal is formed. The precise position of a point target and the formation process of its scattering signal are the prior information used to interpret displacement events.

5.8. Conclusions

PS Interferometry can yield deformation with millimeter-order precision. As discussed in the introduction, two key issues in PS Interferometry are the precise geolocation of the scatterers in 3D space, which has been discussed in Chapter 4, and the association of the scatterers to specific physical features. In this chapter, we have investigated the use of ray-tracing tools to address the second issue by illuminating 3D city models with different levels of detail (LOD1 and LOD2 according to the CityGML standard). As expected, the results obtained depend strongly on the level of detail of the 3D model given as input to the ray-tracing tool.

For our area of study in Rotterdam, we were able to associate 37% of the PS identified in a stack of TerraSAR-X data with simulated scatterers using a LOD2 city model. Using LOD1 models not only reduced the fraction of identified PS to about 10%, but also put most of them on the ground. We did not have models for real cities with a higher level of detail. Nevertheless, from the observation of high-resolution SAR data, it is generally understood that many point-like scatterers result from features, such as windows, that are not captured in LOD2. It is expected that using higher LOD models will further increase the fraction of identified scatterers.

The choice of LOD in the model depends on the application case; however, the superiority of LOD2 is obvious. Models at LOD2 add lots of information to LOD1, as we see in the results, prediction on the LOD2 model is closer to the reality. Moreover, LOD2 models are easier produced than LOD3 models. Therefore, it should be expected that LOD2 city models may become commonplace shortly. The positive results of this study underpin the usefulness of integrating this information in PS processing.

Associating PS to physical features is a necessary step if we want to fully exploit the InSAR signal of individual scatterers, for example, to detect deformation of specific sections of a building. Here we have shown that this association can be made. Each simulated PS can be traced back to one or multiple reflections on specific locations of the 3D model. Moreover, we show that deformation sources translate to individual PS displacement signals using a simulated displacement event. In our case of a five-fold bounce scatterer, sinking displacement produces a signal with an opposite sign to a triple-bounce scatterer. This implies that the bounce levels or the scattering paths, are important attributes to understand the displacements of PS.

6

Conclusions and recommendations

6.1. Conclusions

The main objective of this study is to develop and demonstrate a methodology to link each InSAR scatterer to a real world object. In short, linking radar scatterers to geo-objects requires the precise positioning of all InSAR scatterer, which should be the summation of (i) the relative positioning of each InSAR scatterers within the datum defined by the radar image coordinates, (ii) the positioning of the entire set of scatterers in a 3D earth-centered, earth-fixed reference frame, conditioned by (iii) the criterion of a physically realistic position.

The effective phase center of each scatterer is estimated in radar coordinates by the *sub-pixel based PSI approach*. With the assistance of a corner reflector—or a digital surface model—we correct system-related biases and unaccounted geophysical effects to achieve precise geolocation of all scatterers. The scatterers are then at their geometrically optimal position, but this is not sufficient for the unambiguous association to geo-objects, since the physical scattering of the radar waves can follow multiple paths, especially in a complex environment. One way to resolve this is to reconstruct the physical scattering mechanism using geometric optics with 3D ray-tracing models.

The three steps for linking radar scatterers to geo-objects should be regarded as necessary but not always possible. Especially the last part, determining a physical position, relies heavily on the availability of 3D models of the geo-objects.

The conclusions of this study are related to the three specific sub-questions as listed in Chapter 1.

1. How does the sub-pixel position of a dominant scatterer within the resolution cell affect the PSI estimates, in terms of geolocation and displacement?

We find (chapter 3) that the sub-pixel position influences the 3D point positioning and the deformation estimates at various degrees, depending on the baseline variation

and the imaging parameters of the data stack. The improvement by performing a sub-pixel correction is most significant in the geolocation of the scatterer, typically at the meter-level. In particular this concerns the improvement in the planar (horizontal) precision, as this can be up to the pixel cell size of the SAR data. Thus, the corrected coordinate differences are more significant in the results of Sentinel-1 data which have a relatively coarser resolution than the TerraSAR-X data. In the experiment, validation with a limited number of reflectors showed that the improvement of the TerraSAR-X result is 2.8 m in the east direction and 0.81 m in the north direction, and the Sentinel-1, it is about 4 m in the north direction and 2.4 m in the east direction.

The sub-pixel correction in the height estimation is dependent on the reference phase contribution within the resolution cell and its improvement is more relevant in the case of longer baselines. Validation with CRs showed that the improvement in height by performing a sub-pixel correction is about 1 m for TerraSAR-X and 0.5 m for Sentinel-1. In practice, sub-pixel correction is recommended for elevation estimation for long baselines. The geometry from a longer baseline gives a more precise cross-range estimate, and it introduces more significant sub-pixel errors. On the other hand, a shorter baseline gives more uncertainty in the cross-range estimation but a smaller sub-pixel error. This implies that when focusing on the influence on elevation, i.e. cross-range, only, sub-pixel correction would not be needed for short baselines. However, since the improvement in the planar coordinates is significant as discussed above, it is a negligible additional computational effort to apply the sub-pixel correction for the elevation as well.

The impact of the sub-pixel correction on estimated displacement velocities is about a few tenths of a millimeter per year. While this variation is very small, the impact of this effect should be evaluated considering the goal of the measurement. In cases where decisions depend on threshold values being exceeded, such as determining whether a change of an artificial construction is significant or not, or detecting anomalies due to local deformations, a small bias in the deformation velocity could result in a missed detection.

We also found that, working at the sub-pixel level, the number of coherent PS increases due to a lower phase noise. In our experiments over an urban area, 4% more points were detected in the Sentinel-1 results.

Finally, the decision whether or not to apply the sub-pixel correction requires an evaluation of computational resources (workload) and the expected or required improvements. The main computational effort for sub-pixel correction concerns the oversampling of each individual scatterer. Therefore, the required processing time scales with the amount and the density of PS, and the oversampling factor. As an example, the calculation of 50.000 points—a typical number over an urban area over an area of 100 km² for Sentinel-1—with an oversampling factor of 128 took about 9.5 minutes on a 4-cores workstation with 16 GB of RAM. This time is relatively small compared to the total data processing time (several days), and the advantage in estimation is clear.

2. How can we precisely and reliably geolocate InSAR scatterers by correcting for the positioning bias, which practical approaches are feasible, and when is it valuable to install physical ground control points in the area of interest?

Affected by the system-related biases and unaccounted geophysical effects, the position of InSAR scatterers deviates from the true position, with errors ranging from centimeters to several meters. Correction of those errors is necessary for precise point positioning. We find (chapter 4) that this can be achieved either by (i) a sequence of geophysical corrections, (ii) the deployment of ground control points such as corner reflectors or transponders in several configurations, or (iii) by using suitable digital surface models.

We evaluated the advantages and disadvantages of four approaches: (i) an advanced (geo)physical corrections method, (ii) a CR to be deployed while its phase-center position's precisely measured for a single acquisition, i.e. "single-epoch CR approach", (iii) a CR to be deployed while its phase-center position is precisely measured for a stack of acquisitions, i.e. "multi-epoch CR approach", and (iv) a correction by using a high-precision lidar-based DSM. The performance of these approaches was analyzed using TerraSAR-X and Sentinel-1 data, and reference GNSS measurements.

The first two approaches, the single-epoch CR and the geophysical approach, are incapable of correcting a positioning bias in the cross-range direction. Both approaches have about the same precision. Obviously, the geophysical method does not require physical access to the area of interest, and only involves computational cost, whereas placing a CR implies physical access, additional (GNSS) surveying, and logistic cost, even though the CR only needs to be positioned during one single acquisition (< 15 minutes).

The optimal way of deploying a corner reflector is by maintaining it in a time series of SAR images, such that its phase can be analyzed as a persistent scatter, i.e. the multi-epoch CR approach. This way, also the positional bias in the cross-range direction can be retrieved from the interferometric data, leading to bias correction in an earth-centered, earth-fixed geodetic frame. Apart from the continued maintenance of the CR, this method requires a single GNSS survey to estimate the position of the phase center of the CR. Using this approach, the highest reliability, precision, and accuracy in the geolocation of a PSI point cloud is obtained, typically with a PDOP better than 1 m for TerraSAR-X and 4 m for Sentinel-1.

The fourth approach, the DSM-assisted approach, is less accurate than the multi-epoch CR method, but it is a reasonable alternative if a high-precision DSM is available and/or when physical access to the area of interest is difficult. The quality of the LiDAR DSM data used in this study (AHN-2) is significantly better than DTED-4 specification, leading to a final position precision better than 5 m for Sentinel-1 and 3 m for TerraSAR-X. The precisions achieved using DTED4 are about 10 m for Sentinel-1 and 8 m for TerraSAR-X. The result of the DSM-assisted geolocation approach depends on the quality of the available DSM and also the used point cloud matching algorithm.

We demonstrated that all four approaches can improve the precision of geolocation to some extent. Deployment of a corner reflector for a single SAR acquisition, or using additional geophysical information does not yield 3D geographic coordinates, and can only be used to limit the degrees of freedom in an azimuth-range plane. It should be noted that this can be a valuable improvement in itself. The multi-epoch deployment of a GCP yields the best positioning results in terms of precision, accuracy, and reliability. Yet, this comes at the expense of producing, installing, surveying, and maintaining a CR, as well as physical area access. Alternatively, when a high-precision, high-resolution digital surface model is available, DTED4-level or better, this can be used as a virtual set

of GCPs, with almost comparable geolocation precision.

3. Is the position of the geometric phase center the true physical source of the signal, and—if not—what effect does this have on the interpretation of the estimates?

The geometrically estimated position may be a location that is not physically possible. Therefore, we investigated (chapter 5) the relationship between precise geolocation of the scatterer and its physical source, and assessed how this affects the interpretation of estimated displacements of the scatterers, using geometrical optics with 3D models.

We used ray-tracing to link point scatterers to specific physical features based on 3D city models with different levels of detail: LOD1 and LOD2. In urban environments, multiple scattering signals are indeed ubiquitous and require additional consideration. Our experiments over Rotterdam show that 37% of the PS detected in a stack of TerraSAR-X data can be matched with point-scatterers identified by ray-tracing using an LOD2 model. For the less-detailed LOD1 model only 10% of the detected PS matched with the ray tracing prediction. In the LOD1 case, most matched scatterers are at street-level, while LOD2 allows the identification of many scatterers on the buildings. Over half of the identified scatterers correspond to easily identifiable double or triple bounce-scatterers. This implies that, for TerraSAR-X stripmap data over an urban area, the majority of the detected PS appears to be positioned at their correct physical location. On the other hand, a significant fraction corresponds to higher bounce levels, with approximately 25% being five-fold scatterers. This implies that, while the physically predicted position and the geometrically estimated position seem to match, this position could still be a 'virtual' point, and interpretation of the displacement signal of such a point should be performed with the utmost care.

This analysis shows that the level of detail of the 3D model has a strong influence on the prediction of useful point scatterers using ray tracing. Obviously, LOD1 models are more abundantly available than models with higher levels of detail. In fact, we did not have access to appropriate models for real cities with a higher level of detail (LOD3). Nevertheless, from the observation of high-resolution SAR data, it is generally understood that many point-like scatterers result from features, such as windows, that are not captured in LOD2. It is expected that using higher LOD models might further increase the fraction of identified scatterers.

The experiments using geometrical optics help us to understand the propagation path of scattered signals. But this is limited by the quality and availability of the required 3D models. The mismatch between the geometric center and the real signal source is mainly caused by multiple scattering. Thereby, the association should be made with the information about the target or well-defined association rules, e.g. by exploiting 'ghost' multi-bounce reflections. Moreover, we show that the bounce levels or the scattering paths of the scatterers are an extremely important attribute to understand the displacements on PS. For example, for four or five-fold scattering, a downward displacement may produce a decrease in the geometric path length, which would be erroneously interpreted as an upward displacement.

6.2. Main contributions

The six main contributions of this research are summarized as follows.

1. The influence of sub-pixel correction on the positioning accuracy and displacement quality is demonstrated theoretically, see Sec. 3.2, and experimentally with a stack of TerraSAR-X, Radarsat-2, and Sentinel-1 acquisitions, see Sec. 3.5 and 3.6.
2. Several methods to correct the positioning bias are evaluated and compared for practical applicability, see Sec. 4.7. This includes methods using ground control points (corner reflectors or transponders), advanced geophysical corrections, and methods using high-resolution digital surface models. A method using a single corner reflector, deployed only during a single acquisition (single-epoch), see Sec. 4.3.1, is compared to a method using a single reflector deployed during the full extend of a time series (multi-epoch), see Sec. 4.3.2, and a high-precision LiDAR DSM, see Sec. 4.4. The performance of these methods is evaluated with TerraSAR-X and Sentinel-1 data, see Sec. 4.6. For the DSM-assisted approach, we evaluated the influence of the quality of the DSM, expressed in the DTED level, see Sec. 4.6.3.
3. We proposed a positioning covariance matrix-based method for point cloud matching between persistent scatterers, and lidar point cloud or simulated scatterers, see Sec. 5.4.
4. We demonstrated that it is possible to establish a physical link between 3D models and scatterers using ray-tracing, see Sec. 5.6.
5. The influence of the *level of detail* (LOD) of the city models on point scatterers prediction is demonstrated in Sec. 5.3.
6. We showed that deformation signals may translate differently to individual PS displacement signals due to multiple scattering, see Sec. 5.7.

List of Publications

Journal articles:

1. **Yang, M.**, Dheenathayalan, P., López-Dekker, P, Van Leijen E, Liao, M., and Hanssen, R.F. (2020). On the Influence of Sub-pixel Position Correction for PS Positioning accuracy and Time Series Quality, *ISPRS Journal of Photogrammetry and Remote Sensing*, 165, 98-107.
2. **Yang, M.**, López-Dekker, P, Dheenathayalan, P, Liao, M., and Hanssen, R.F. (2019). Artificial Reflectors and Surface Models in Precise Point Positioning of InSAR Point Cloud, *ISPRS Journal of Photogrammetry and Remote Sensing*, 158, 113-122.
3. **Yang, M.**, López-Dekker, P, Dheenathayalan, P, Biljecki, F, Liao, M., Hanssen, R.F. (2019). Linking Persistent Scatterers to the Built Environment Using Ray Tracing on Urban Models. *IEEE Transactions on Geoscience and Remote Sensing*, 57(8): 5764-5776.

4. **Yang, M.**, Yang, T., Zhang, L., Lin, J., Qin, X., Liao, M. (2018) Spatio-Temporal Characterization of a Reclamation Settlement in the Shanghai Coastal Area with Time Series Analyses of X-, C-, and L-Band SAR Datasets. *Remote Sensing*, 10(2).
5. **Yang, M.**, Liao M., Qin, X. Zhang, L. (2017). Analysis of Capabilities of C-and L-band SAR Data to Detect Newly-reclaimed Area. *Geomatics & Information Science of Wuhan University*, 42(6), 797-802. (In Chinese)
6. **Yang, M.**, Liao, M., Shi, X., Zhang, L. (2017). Land Subsidence Monitoring by Joint Estimation of Multi-platform Time Series InSAR Observations. *Geomatics & Information Science of Wuhan University*, 42(9):1300-1305. (In Chinese)
7. **Yang, M.**, Jiang, Y., Liao, M., Wang, H. (2013). The analysis of the subsidence patterns in Lingang New City (Shanghai) using high-resolution SAR images. *Shanghai Land and Resources*, 34(4):12-16. (In Chinese)
8. Wang R., Yang T., **Yang, M.**, Liao, M. (2019) A safety analysis of elevated highways in Shanghai linked to dynamic load using long-term time-series of InSAR stacks. *Remote Sensing Letters*, 10(12): 1133-1142.
9. Li, M., Zhang, L., Shi, X., Liao, M., **Yang, M.** (2019). Monitoring active motion of the Guobu landslide near the Laxiwa Hydropower Station in China by time-series point-like targets offset tracking. *Remote Sensing of Environment*, 221:80-93.
10. Qin, X., Zhang, L., **Yang, M.**, Luo, H., Liao, M., & Ding, X. (2018). Mapping surface deformation and thermal dilation of arch bridges by structure-driven multi-temporal DInSAR analysis. *Remote Sensing of Environment*, 216:71-90.
11. Qin, X., Zhang, L., Ding, X., Liao, M., **Yang, M.** (2018). Mapping and Characterizing Thermal Dilation of Civil Infrastructures with Multi-Temporal X-Band Synthetic Aperture Radar Interferometry. *Remote Sensing*, 10(6).
12. Qin, X., Liao, M., **Yang, M.**, et al. (2017) Monitoring structure health of urban bridges with advanced multi-temporal InSAR analysis. *Annals of Gis: Geographic Information Sciences*, 23(4), 293-302.
13. Qin, X., **Yang, M.**, Zhang, L., Yang, T., & Liao, M. (2017). Health Diagnosis of Major Transportation Infrastructures in Shanghai Metropolis Using High-Resolution Persistent Scatterer Interferometry. *Sensors*, 17(12).
14. Qin, X., Liao, M., Zhang, L., **Yang, M.** (2017). Structural Health and Stability Assessment of High-Speed Railways via Thermal Dilation Mapping With Time-Series InSAR Analysis. *IEEE Journal of Selected Topics in Applied Earth Observation and Remote Sensing*, 10(6): 2999-3010.
15. Wang, R., **Yang, M.**, Liao, M., Li, X., Zhang, L. (2019) Attribution Analysis on Deformation Feature of the Shanghai Elevated Highway by Persistent Scatterer SAR Interferometry. *Geomatics & Information Science of Wuhan University*, 43(12):2050-2057. (In Chinese)

16. Qin, X., **Yang, M.**, Liao, M., Wang, H., Yang, T. (2017). Exploring Temporal-Spatial Characteristics of Shanghai Road Networks Settlement with Multi-temporal PSInSAR Technique. *Geomatics & Information Science of Wuhan University*,42(2):170-177. (In Chinese)
17. Qin, X., **Yang, M.**, Wang, H., Yang, T., Lin, J., Liao, M. (2016). Application of High-resolution PS-InSAR in Deformation Characteristics Probe of Urban Rail Transit. *Acta Geodaetica et Cartographica Sinica*, 45 (6):713-721. (In Chinese)
18. Jiang, Y., **Yang, M.**, Liao, M., Wang, H. (2013). Deformation monitoring of the Shanghai Maglev system based on the time-series analysis of InSAR data. *Shanghai Land and Resources*, 34(4):17-20. (In Chinese)

Conference proceedings

1. **Yang, M.**, Wang, R., Liao, M., López-Dekker, P, Hanssen, R.F (2018). PSI Target Characterization For Monitoring Shanghai Metro Tunnels. In ICA Symposium on Early Warning and Crises Management in the Big Data Era, Shenzhen, China, December 2018.
2. **Yang, M.**, Dheenathayalan, P, Biljecki F, Hanssen, R.F (2017). On the Predictability of PS occurrence and location based on 3D Ray-tracing models. In the 10th International Workshop on "Advances in the Science and Applications of SAR Interferometry and Sentinel-1 InSAR", 'Fringe 2017', Helsinki, Finland, June 2017.
3. **Yang, M.**, Dheenathayalan, P, Chang, L., Wang, J., Lindenbergh, R.C., Liao, M., Hanssen, R.F (2016) High-precision 3D geolocation of persistent scatterers with one single-EPOCH GCP and LIDAR DSM data. In L. Ouwehand (Ed.), Proceedings of Living Planet Symposium 2016 (Vol. SP-740, pp. 398-398), Prague, Czech Republic, May 2016.
4. **Yang, M.**, Liao M., Zhang L. (2014). Unbiased subsidence rate estimation based on Multi-Platform Time Series Interferometric SAR Observations, in Advanced Imaging SAR seminar (ADSAR), Beijing, China, September, 2014.
5. **Yang, M.**, Liao M., Zhang L. (2014). Joint Analysis of Land Subsidence with Multi-Platform Time Series InSAR Data Stacks, Dragon 3 Mid-Term Results, Chengdu, China, June, 2014.
6. Wang, R., Liao, M., **Yang, M.** (2019) Featuring the Deformation along metro lines in Shanghai with six years TerraSAR-X Dataset. In TerraSAR-X / TanDEM-X Science Team Meeting, Oberpfaffenhofen, Germany, October, 2019.
7. Qin, X., Liao M., Shi, X., **Yang, M.** (2016). Stability assessment of high-speed railway using advanced InSAR technique. In IEEE International Geoscience and Remote Sensing Symposium (IGARSS), Beijing, 2016.
8. Shi, X., Liao, M., Zhang, L., **Yang, M.**, Balz, T. (2015) Improved small-baseline subset analysis of high resolution SAR images for linear infrastructure deformation mapping. In Fringe Workshop on " Advances in the Science and Applications of SAR Interferometry and Sentinel-1 InSAR", Frascati, Italy, March, 2015.

6.3. Recommendations

The results of this study lead to recommendations for operational practice in geodetic surveys using InSAR. Moreover, the study touched upon several issues which require further investigation.

First, it is recommended that point scatterers in the built environment are to be precisely positioned, using the methodologies described. This enables accurate city scanning, and pinpointing where constructions may be at risk. Moreover, in urban environments, displacement signals expressed by radar scatterers from various objects describe different deformation phenomena. To better understand the deformation mechanism, and to avoid misinterpretation, it is of paramount importance that point scatterers are accurately positioned.

For new InSAR studies in the built environment, it is advised to use a high precision DSM to enable this precise InSAR point cloud positioning. While a multi-epoch deployment of a ground control point, i.e. a corner reflector, yields optimal positioning results in terms of precision and accuracy, it requires physical access to the area, extra cost, and effort. Given the performance of the DSM-based approach and increasingly available national-level high-precision lidar-based DSM, we recommend correcting the InSAR point cloud based on high-precision DSM as a routine process.

We recommend considering—if possible even integrating—the ‘bounce numbers’ when interpreting radar scatterers. In the urban scenario, multipath scattering is ubiquitous. Multiple-reflection scatterers do not only provide displacement observations, but also object information such as the target size. The bounce number should not be ignored when exploring multi-path signals. Multi-path scattering may lead to a physically non-realistic phase center position and the observed displacements can be considered as a function of bounce number. But, calculating the bounce number of each scatterer needs further investigation. Polarized SAR data can only distinguish odd and even bounce scattering. In this study, we used ray-tracing with 3D models for predicting the scatterers, and the bounce number can be directly calculated. While this is not always possible as it requires accurate 3D city models, a generic approach for bounce number calculation is needed.

It is desirable to further utilize the amplitude information in time series SAR data for characterizing radar scatterers. Amplitude observations are a function of the physical shape, surface parameters and dielectric properties of the illuminated geo-object, and even the environmental conditions around the illuminated area. The time series of amplitude is an observation of how these parameters of the target change over time. Therefore, how to make full and optimal use of the amplitude data to interpret the scatterers should be further investigated.

Finally, incorporating semantic information of a LiDAR point cloud or a 3D model with radar scatterers is very promising. Semantic information in LiDAR point clouds or 3D models provides scene information, but how to explore this information for optimized interpretation of InSAR scatterers needs to be further investigated.

Appendix A

Sub-pixel phase in range and reference phase

The sub-pixel phase in range $\phi_{i,\eta}$ is equivalent to the reference phase variation with the incidence angle θ_i^m (van Leijen, 2014). The reference phase $\phi_{i,\text{ref}}$ under the far-field approximation is defined as (Hanssen, 2001)

$$\phi_{i,\text{ref}} = \frac{4\pi}{\lambda} B \sin(\theta_i^m - \alpha), \quad (\text{A.1})$$

and therefore the variation of the reference phase as function of the incidence angle is

$$\partial\phi_{i,\text{ref}} = \frac{4\pi}{\lambda} B \cos(\theta_i^m - \alpha) \partial\theta = \frac{4\pi}{\lambda} B_{\perp} \partial\theta. \quad (\text{A.2})$$

The incidence angle can be approximated by (Fig. 2.4)

$$\theta^m = \arccos\left(\frac{H_{\text{sat}}}{r_i}\right), \quad (\text{A.3})$$

where H_{sat} is the height of the satellite and r_i is the range to the antenna. Thus, the incidence angle varies with slant range as

$$\partial\theta = \frac{\cos\theta_i^m}{r_i^m \sin\theta_i^m} \partial r, \quad (\text{A.4})$$

and thus the variation of the reference phase, Eq.(A.2), can then be written as

$$\partial\phi_{i,\text{ref}} = \frac{4\pi}{\lambda} B_{\perp} \frac{\cos\theta_i^m}{r_i^m \sin\theta_i^m} \partial r. \quad (\text{A.5})$$

Since, the sub-pixel phase in range is, Eq.(3.8),

$$\phi_{i,\eta} = \frac{4\pi}{\lambda} \cdot \frac{B_{\perp}}{r_i^m} \cdot \cos\theta_i^m \cdot \eta_i, \quad (\text{A.6})$$

and the relation between η_i and the slant range is (Fig. 3.4)

$$\eta_i = \frac{\partial r}{\sin\theta_i^m}, \quad (\text{A.7})$$

we conclude that the variation of the reference phase $\partial\phi_{i,\text{ref}}$ as a function of the incidence angle equals the sub-pixel phase in range $\phi_{i,\eta}$.

Bibliography

- Adam, N., Eineder, M., Yague-Martinez, N., and Bamler, R. (2008). High resolution interferometric stacking with TerraSAR-X. In *IEEE International Geoscience and Remote Sensing Symposium, 2008. IGARSS 2008.*, volume 2, pages II–117. IEEE.
- Adam, N., Kampes, B. M., and Eineder, M. (2004). The development of a scientific persistent scatterer system: Modifications for mixed ERS/ENVISAT time series. In *ENVISAT & ERS Symposium, Salzburg, Austria, 6–10 September, 2004*, page 9.
- Alberga, V. (2004). Volume decorrelation effects in polarimetric SAR interferometry. *IEEE Trans. Geosci. Remote Sens.*, 42(11):2467–2478.
- Andersh, D., Moore, J., Kosanovich, S., Kapp, D., Bhalla, R., Kipp, R., Courtney, T., Nolan, A., German, F., Cook, J., and Hughes, J. (2000). Xpatch 4: the next generation in high frequency electromagnetic modeling and simulation software. In *Record of the IEEE 2000 International Radar Conference [Cat. No. 00CH37037]*, pages 844–849.
- Auer, S. (2011). *3D synthetic aperture radar simulation for interpreting complex urban reflection scenarios*. PhD thesis, Technische Universität München.
- Auer, S. and Gernhardt, S. (2017). Linear signatures in urban SAR images—partly misinterpreted? *IEEE Geosci. Remote Sens. Lett.*, 11(10):1762–1766.
- Auer, S., Gernhardt, S., and Bamler, R. (2011). Ghost persistent scatterers related to multiple signal reflections. *IEEE Geosci. Remote Sens. Lett.*, 8(5):919–923.
- Auer, S., Hinz, S., and Bamler, R. (2010). Ray-tracing simulation techniques for understanding high-resolution SAR images. *IEEE Trans. Geosci. Remote Sens.*, 48(3):1445–1456.
- Balss, U., Gisinger, C., and Eineder, M. (2018). Measurements on the absolute 2-d and 3-d localization accuracy of TerraSAR-X. *Remote Sens.*, 10(4).
- Balz, T. and Stilla, U. (2009). Hybrid gpu-based single-and double-bounce SAR simulation. *IEEE Trans. Geosci. Remote Sens.*, 47(10):3519–3529.
- Bamler, R., Adam, N., Davidson, G. W., and Just, D. (1998). Noise-induced slope distortion in 2-d phase unwrapping by linear estimators with application to SAR interferometry. *IEEE Trans. Geosci. Remote Sens.*, 36(3):913–921.
- Bamler, R. and Eineder, M. (2005). Accuracy of differential shift estimation by correlation and split-bandwidth interferometry for wideband and delta-k SAR systems. *IEEE Geosci. Remote Sens. Lett.*, 2(2):151–155.

- Bamler, R. and Schättler, B. (1993). SAR data acquisition and image formation. In *Geocoding: ERS-1 SAR Data and Systems*, Wichmann-Verlag, pages 53–102. Wichmann-Verlag.
- BBC News (2019). Brumadinho dam collapse: Little hope of finding missing in Brazil.
- Bennett, J. R. and Cumming, I. G. (1979). A digital processor for the production of Seasat Synthetic Aperture Radar imagery. Technical Report ESA SP-154, ESA.
- Berardino, P., Fornaro, G., Lanari, R., and Sansosti, E. (2002). A new algorithm for surface deformation monitoring based on small baseline differential SAR interferograms. *IEEE Trans. Geosci. Remote Sens.*, 40(11):2375–2383.
- Bevis, M., Businger, S., Herring, T. A., Rocken, C., Anthes, R. A., and Ware, R. H. (1992). GPS meteorology: Remote sensing of atmospheric water vapor using the Global Positioning System. *J. Geophys. Res.*, 97:15,787–15,801.
- Bhalla, R., Lin, L., and Andersh, D. (2005). A fast algorithm for 3D SAR simulation of target and terrain using xpatch. In *IEEE International Radar Conference, 2005.*, pages 377–382.
- Biljecki, F., Heuvelink, G. B. M., Ledoux, H., and Stoter, J. (2018). The effect of acquisition error and level of detail on the accuracy of spatial analyses. *Cartography Geogr. Info. Sci.*, 45(2):156–176.
- Biljecki, F., Ledoux, H., and Stoter, J. (2016). An improved LOD specification for 3D building models. *Comput. Environ. Urban Syst.*, 59:25–37.
- Biljecki, F., Ledoux, H., Stoter, J., and Zhao, J. (2014). Formalisation of the level of detail in 3D city modelling. *Comput. Environ. Urban Syst.*, 48:1–15.
- Boeing, G. (2016). Osmnx: New methods for acquiring, constructing, analyzing, and visualizing complex street networks. *Comput. Environ. Urban Syst.*, 65:126–139.
- Bourbigot, M., Johnson, H., and Piantanida, R. (2016). *Sentinel-1 Product Definition*. MDA Document Number: SEN-RS-52-7440, MacDonald, Dettwiler and Associates Ltd.: Richmond, BC, Canada, ESA CDRL number: pdl1-1, pdl2-1 edition.
- Castelloe, M. W. and Munson, D. C. (1997). 3-d SAR imaging via high-resolution spectral estimation methods: experiments with xpatch. In *Proceedings of International Conference on Image Processing*, volume 1, pages 853–856.
- Casu, F., Buckley, S. M., Manzo, M., Pepe, A., and Lanari, R. (2005). Large scale InSAR deformation time series: Phoenix and Houston case studies. In *IEEE International Geoscience and Remote Sensing Symposium, 2005. IGARSS 2005.*, pages 5240–5243.
- Chang, L., Dollevoet, R. P. B. J., and Hanssen, R. F. (2017). Nationwide railway monitoring using satellite SAR interferometry. *IEEE J. Sel. Topics Appl. Earth Observ. Remote Sens.*, 10(2):596–604.

- Chang, L. and Hanssen, R. F. (2014). Detection of cavity migration and sinkhole risk using radar interferometric time series. *Remote Sens. Environ.*, 147(9):56–64.
- Chang, L. and Hanssen, R. F. (2016). A probabilistic approach for InSAR time-series post-processing. *IEEE Trans. Geosci. Remote Sens.*, 54(1):421–430.
- Chaussard, E., Wdowinski, S., Cabral-Cano, E., and Amelung, F. (2014). Land subsidence in central Mexico detected by alos InSAR time-series. *Remote Sens. Environ.*, 140:94–106.
- Chen, F., Lin, H., Li, Z., Quan, C., and Zhou, J. (2012). Interaction between permafrost and infrastructure along the qinghai–tibet railway detected via jointly analysis of c- and l-band small baseline SAR interferometry. *Remote Sens. Environ.*, 123:532–540.
- Chetverikov, D., Stepanov, D., and Krsek, P. (2005). Robust euclidean alignment of 3D point sets: the trimmed iterative closest point algorithm. *Image Vision Comput.*, 23(3):299 – 309.
- Cong, X., Balss, U., Eineder, M., and Fritz, T. (2012). Imaging geodesy - centimeter-level ranging accuracy with TerraSAR-X: An update. *IEEE Geosci. Remote Sens. Lett.*, 9(5):948–952.
- Costantini, M. (1996). A phase unwrapping method based on network programming. In *'FRINGE 96' workshop on ERS SAR Interferometry, Zürich, Switzerland, 30 Sep–2 October 1996*.
- Costantini, M., Falco, S., Malvarosa, F., and Minati, F. (2008). A new method for identification and analysis of persistent scatterers in series of SAR images. In *IEEE International Geoscience and Remote Sensing Symposium, 2008. IGARSS 2008.*, volume 2, pages II–449–II–452.
- Crosetto, M., Crippa, B., and Biescas, E. (2005). Early detection and in-depth analysis of deformation phenomena by radar interferometry. *Eng. Geol.*, 79(1):81 – 91. Application of Geodetic Techniques in Engineering Geology.
- Crosetto, M., Monserrat, O., Cuevas-González, M., Devanthéry, N., and Crippa, B. (2016). Persistent scatterer interferometry: A review. *ISPRS J. Photogramm. Remote Sens.*, 115:78–89.
- Cumming, I. and Wong, F. (2005a). *Digital Processing Of Synthetic Aperture Radar Data: Algorithms And Implementation*. Artech House Publishers, New York. ISBN 1580530583.
- Cumming, I. G. and Wong, H. C. (2005b). *Digital processing of synthetic radar data : algorithms and implementation*. Artech House Publishers, New York.
- Curlander, J. C. and McDonough, R. N. (1991). *Synthetic aperture radar: systems and signal processing*. John Wiley & Sons, Inc, New York.

- Devanathéry, N., Crosetto, M., Monserrat, O., Cuevas-González, M., and Crippa, B. (2014). An approach to persistent scatterer interferometry. *Remote Sens.*, 6(7):6662–6679.
- Dheenathayalan, P. (2019). *Optimizing the exploitation of persistent scatterers in satellite radar interferometry*. PhD thesis, Delft University of Technology.
- Dheenathayalan, P., Caro Cuenca, M., Hogeboom, P., and Hanssen, R. F. (2017). Small reflectors for ground motion monitoring with InSAR. *IEEE Trans. Geosci. Remote Sens.*, 55(12):6703–6712.
- Dheenathayalan, P., Small, D., and Hanssen, R. F. (2018). 3D positioning and target association for medium resolution SAR sensors. *IEEE Trans. Geosci. Remote Sens.*, page in press.
- Dheenathayalan, P., Small, D., Schubert, A., and Hanssen, R. F. (2016). High-precision positioning of radar scatterers. *J. Geod.*, 90(5):403–422.
- Ding, X., Liu, G., Li, Z., Li, Z., and Chen, Y. Q. (2004). Ground subsidence monitoring in hong kong with satellite SAR interferometry. *Photogramm. Eng. Remote Sens.*, 70(10):1151–1156.
- Duque, S., Parizzi, A., Zan, F. D., and Eineder, M. (2016). Precise and automatic 3D absolute geolocation of targets using only two long-aperture SAR acquisitions. In *IEEE International Geoscience and Remote Sensing Symposium, 2016. IGARSS 2016.*, pages 7415–7418.
- Dutch News (2016). Shored-up homes are a common sight in earthquake-hit groningen.
- Eineder, M., Minet, C., Steigenberger, P., Cong, X., and Fritz, T. (2011). Imaging geodesy - toward centimeter-level ranging accuracy with TerraSAR-X. *IEEE Trans. Geosci. Remote Sens.*, 49(2):661–671.
- Ferretti, A., Fumagalli, A., Novali, F., Prati, C., Rocca, F., and Rucci, A. (2011). A new algorithm for processing interferometric data-stacks: SqueeSAR. *IEEE Trans. Geosci. Remote Sens.*, 49(9):3460–3470.
- Ferretti, A., Prati, C., and Rocca, F. (2001). Permanent scatterers in SAR interferometry. *IEEE Trans. Geosci. Remote Sens.*, 39(1):8–20.
- Ferretti, A., Savio, G., Barzaghi, R., Borghi, A., Musazzi, S., Novali, F., Prati, C., and Rocca, F. (2007). Submillimeter accuracy of InSAR time series: Experimental validation. *IEEE Trans. Geosci. Remote Sens.*, 45(5):1142–1153.
- Fornaro, G., Verde, S., Reale, D., and Pauciuillo, A. (2015). CAESAR: An approach based on covariance matrix decomposition to improve multibaseline–multitemporal interferometric SAR processing. *IEEE Trans. Geosci. Remote Sens.*, 53(4):2050–2065.
- Franceschetti, G., Migliaccio, M., and Riccio, D. (1998). On ocean SAR raw signal simulation. *IEEE Trans. Geosci. Remote Sens.*, 36(1):84–100.

- Franceschetti, G., Migliaccio, M., Riccio, D., and Schirinzi, G. (1992). SARAS: a synthetic aperture radar (SAR) raw signal simulator. *IEEE Trans. Geosci. Remote Sens.*, 30(1):110–123.
- Fruneau, B. and Sarti, F. (2000). Detection of ground subsidence in the city of paris using radar interferometry: isolation of deformation from atmospheric artifacts using correlation. *Geophys. Res. Lett.*, 27(24):3981–3984.
- Garthwaite, M. C. (2017). On the design of radar corner reflectors for deformation monitoring in multi-frequency InSAR. *Remote Sens.*, 9(7):648.
- Garthwaite, M. C., Nancarrow, S., Hislop, A., Dawson, J., Lawrie, S., and Thankappan, M. (2015). *The Design of Radar Corner Reflectors for the Australian Geophysical Observing System: A Single Design Suitable for InSAR Deformation Monitoring and SAR Calibration at Multiple Microwave Frequency Bands*. Geoscience Australia.
- Gernhardt, S., Auer, S., and Eder, K. (2015). Persistent scatterers at building facades—evaluation of appearance and localization accuracy. *ISPRS J. Photogramm. Remote Sens.*, 100:92–105.
- Gernhardt, S., Cong, X., Eineder, M., Hinz, S., and Bamler, R. (2012). Geometrical fusion of multitrack ps point clouds. *IEEE Geosci. Remote Sens. Lett.*, 9(1):38–42.
- Geudtner, D., Prats, P., Yaguemartinez, N., De Zan, F., Breit, H., Larsen, Y., Monti-Guarnieri, A., Barat, I., Navas-Traver, I., and Torres, R. (2017). Sentinel-1 constellation SAR interferometry performance verification. In *ESA Fringe 2017*, pages 1457–1460.
- Ghiglia, D. C. and Pritt, M. D. (1998). *Two-dimensional phase unwrapping: theory, algorithms, and software*. John Wiley & Sons, Inc, New York.
- Gisinger, C., Balss, U., Pail, R., Zhu, X. X., Montazeri, S., Gernhardt, S., and Eineder, M. (2015). Precise three-dimensional stereo localization of corner reflectors and persistent scatterers with TerraSAR-X. *IEEE Trans. Geosci. Remote Sens.*, 53(4):1782–1802.
- Gisinger, C., Willberg, M., Balss, U., Klügel, T., Mähler, S., Pail, R., and Eineder, M. (2017). Differential geodetic stereo SAR with TerraSAR-X by exploiting small multi-directional radar reflectors. *J. Geod.*, 91(1):53–67.
- Glassner, A. S. (1989). *An introduction to ray tracing*. Elsevier.
- Goel, K. and Adam, N. (2014). A distributed scatterer interferometry approach for precision monitoring of known surface deformation phenomena. *IEEE Trans. Geosci. Remote Sens.*, 52(9):5454–5468.
- Goldstein, R. M., Zebker, H. A., and Werner, C. L. (1988). Satellite radar interferometry: Two-dimensional phase unwrapping. *Radio Sci.*, 23(4):713–720.
- Gonzalez, R. C. and Woods, R. E. (2007). *Digital Image Processing (3rd Edition)*. Prentice-Hall, Inc. Division of Simon and Schuster One Lake Street Upper Saddle River, NJ, United States.

- Gray, A. L., Mattar, K. E., and Sofko, G. (2000). Influence of ionospheric electron density fluctuations on satellite radar interferometry. *Geophys. Res. Lett.*, 27(10):1451–1454.
- Guarnieri, A. M. and Tebaldini, S. (2008). On the exploitation of target statistics for sar interferometry applications. *IEEE Trans. Geosci. Remote Sens.*, 46(11):3436–3443.
- Hajnsek, I., Busche, T., and Moreira, A. (2009). Mission status and data availability: TanDEM-X. In *International Workshop on Applications of Polarimetry and Polarimetric Interferometry Pol-InSAR*.
- Hammer, H. and Schulz, K. (2009). Coherent simulation of SAR images. In *Proc SPIE Image Signal Process. Remote Sens. XV 7477*, pages 74771K–1–8.
- Hanssen, R. F. (2001). *Radar Interferometry: Data Interpretation and Error Analysis*. Kluwer Academic Publishers, Dordrecht.
- Hanssen, R. F. (2005). Satellite radar interferometry for deformation monitoring: a priori assessment of feasibility and accuracy. *Int. J. Appl. Earth Obs. Geoinf.*, 6(3-4):253–260.
- Hanssen, R. F. (2017). A radar retroreflector device and a method of preparing a radar retroreflector device. International Patent WO2018236215A1.
- Hanssen, R. F. and Bamler, R. (1999). Evaluation of interpolation kernels for SAR interferometry. *IEEE Trans. Geosci. Remote Sens.*, 37(1):318–321.
- Hanssen, R. F., Van Nattijne, A., Lindenbergh, R. C., Dheenathayalan, P., Yang, M., Chang, L., Van Leijen, F. J., López-Dekker, P., Der Maaden, J. V., Van Oosterom, P., et al. (2018). Scatterer identification and analysis using combined InSAR and laser data. *The EGU General Assembly*.
- Hazlett, M., Andersh, D. J., Lee, S. W., Ling, H., and Yu, C. L. (1995). Xpatch: a high-frequency electromagnetic scattering prediction code using shooting and bouncing rays. *Proceedings of SPIE - The International Society for Optical Engineering*, 2469:266–275.
- Heady, B., Kroenung, G., and Rodarmel, C. (2009). High resolution elevation data (hre) specification overview. In *ASPRS/MAPPS 2009 Conference, San Antonio, Texas*.
- Hetland, E., Musé, P., Simons, M., Lin, Y., Agram, P., and DiCaprio, C. (2012). Multiscale InSAR time series (mints) analysis of surface deformation. *J. Geophys. Res.-sol. Ea.*, 117(B2).
- Hooper, A. (2006). *Persistent Scatterer Radar Interferometry for Crustal Deformation Studies and Modeling of Volcanic Deformation*. PhD thesis, Stanford University.
- Hooper, A. (2008). A multitemporal InSAR method incorporating both persistent scatterer and small baseline approaches. *Geophys. Res. Lett.*, 35(16):96–106.
- Hooper, A., Zebker, H., Segall, P., and Kampes, B. (2004). A new method for measuring deformation on volcanoes and other natural terrains using InSAR persistent scatterers. *Geophys. Res. Lett.*, 31(23).

- Hu, F., Wu, J., Chang, L., and Hanssen, R. F. (2019). Incorporating temporary coherent scatterers in multi-temporal InSAR using adaptive temporal subsets. *IEEE Trans. Geosci. Remote Sens.*, 57(10):7658–7670.
- Hu, J., Li, Z., Ding, X., Zhu, J., and Sun, Q. (2013). Spatial-temporal surface deformation of los angeles over 2003-2007 from weighted least squares DInSAR. *Int. J. Appl. Earth Obs.*, 21:484–492.
- Huang, Y. H., Seguin, G., and Sultan, N. (1997). Multi-frequency and multi-polarization SAR system analysis with simulation software developed at CSA. In *IEEE International Geoscience and Remote Sensing Symposium, 1997. IGARSS 1997.*, volume 1, pages 536–538.
- Hunt, B. R. (1979). Matrix formulation of the reconstruction of phase values from phase differences. *J. Opt. Soc. Am. A-Opt. Image Sci. Vis.*, 69(3):393–399.
- Iglesias, R., Monells, D., Centolanza, G., Mallorquí, J. J., and López-Dekker, P. (2012). A new approach to dinsar pixel selection with spectral correlation along time between sublooks. In *EUSAR 2012; 9th European Conference on Synthetic Aperture Radar*, pages 665–668.
- Jiang, L., Lin, H., and Cheng, S. (2011a). Monitoring and assessing reclamation settlement in coastal areas with advanced InSAR techniques: Macao city (china) case study. *Int. J. Remote Sens.*, 32(13):3565–3588.
- Jiang, M., Li, Z., Ding, X., Zhu, J., and Feng, G. (2011b). Modeling minimum and maximum detectable deformation gradients of interferometric SAR measurements. *Int. J. Appl. Earth Obs.*, 13(5):766–777.
- Jolivet, R., Agram, P., Lin, N. Y., Simons, M., Doin, M., Peltzer, G., and Li, Z. (2014). Improving InSAR geodesy using global atmospheric models. *J. Geophys. Res.*, 119(3):2324–2341.
- Kampes, B. M. (2005). *Displacement Parameter Estimation using Permanent Scatterer Interferometry*. PhD thesis, Delft University of Technology, Delft, the Netherlands.
- Kampes, B. M. (2006). *Radar Interferometry: Persistent Scatterer Technique*. Springer, Dordrecht, The Netherlands.
- Kampes, B. M. and Adam, N. (2006). The STUN algorithm for persistent scatterer interferometry. In *Fourth International Workshop on ERS/Envisat SAR Interferometry, 'FRINGE05', Frascati, Italy, 28 Nov-2 Dec 2005*, page 14 pp.
- Ketelaar, G., Zeijlmaker, L., and Hanssen, R. F. (2006). Monitoring subsidence due to gas extraction using satellite radar interferometry in Groningen, the Netherlands. *Shell EP Journal of Technology*, 7004:35–38.
- Keys, R. (1981). Cubic convolution interpolation for digital image processing. *IEEE Trans. Acoust., Speech, Signal Process.*, 29(6):1153–1160.

- Labetski, A. (2017). *General 3dftier tutorial to generate LOD1 models*. TuDelft 3D Geoinformation.
- Lee, J.-S., Papathanassiou, K. P., Ainsworth, T. L., and adn Andreas Reigber, M. R. G. (1998). A new technique for noise filtering of SAR interferometric phase images. *IEEE Trans. Geosci. Remote Sens.*, 36(5):1456–1465.
- Li, M., Zhang, L., Shi, X., Liao, M., and Yang, M. (2019a). Monitoring active motion of the Guobu landslide near the Laxiwa Hydropower Station in China by time-series point-like targets offset tracking. *Remote Sens. Environ.*, 221:80 – 93.
- Li, Z., Cao, Y., Wei, J., Duan, M., Wu, L., Hou, J., and Jian-Jun, Z. (2019b). Time-series InSAR ground deformation monitoring: Atmospheric delay modeling and estimating. *Earth-Science Reviews*, 192.
- Liao, M. and Wang, T. (2014). *Time Series InSAR Technology and Application (in Chinese)*. China Science Press, Beijing, China.
- Liu, G., Luo, X., Chen, Q., Huang, D., and Ding, X. (2008). Detecting land subsidence in shanghai by ps-networking SAR interferometry. *SENSORS-BASEL*, 8(8):4725–4741.
- Lv, X., Yazici, B., Zeghal, M., Bennett, V., and Abdoun, T. (2014). Joint-scatterer processing for time-series InSAR. *IEEE Trans. Geosci. Remote Sens.*, 52(11):7205–7221.
- López-Quiroz, P., Doin, M.-P., Tupin, F., Briole, P., and Nicolas, J.-M. (2009). Time series analysis of mexico city subsidence constrained by radar interferometry. *J. Appl. Geophys.*, 69(1):1 – 15. Advances in SAR Interferometry from the 2007 Fringe Workshop.
- Ma, P., Lin, H., Lan, H., and Chen, F. (2015). Multi-dimensional SAR tomography for monitoring the deformation of newly built concrete buildings. *ISPRS J. Photogramm. Remote Sens.*, 106:118 – 128.
- Margarit, G., Mallorqui, J. J., Rius, J. M., and Sanz-Marcos, J. (2006). On the usage of GRECOSAR, an orbital polarimetric SAR simulator of complex targets, to vessel classification studies. *IEEE Trans. Geosci. Remote Sens.*, 44(12):3517–3526.
- Marinkovic, P., Ketelaar, G., and Hanssen, R. F. (2004). A controled Envisat/ERS permanent scatterer experiment, implications of corner reflector monitoring. In *CEOS SAR Workshop, Ulm Germany, 27–28 May 2004*.
- Marinkovic, P., Ketelaar, G., van Leijen, F., and Hanssen, R. F. (2008). InSAR quality control: Analysis of five years of corner reflector time series. In *in Proceedings of the 5th International Workshop on ERS/Envisat SAR Interferometry (FRINGE '07)*.
- Martino, G. D., Iodice, A., Poreh, D., and Riccio, D. (2018). Pol-SARAS: A fully polarimetric SAR raw signal simulator for extended soil surfaces. *IEEE Trans. Geosci. Remote Sens.*, 56(4):2233–2247.
- Meyer, F., Bamler, R., Jakowski, N., and Fritz, T. (2006). The potential of low-frequency SAR systems for mapping ionospheric tec distributions. *IEEE Trans. Geosci. Remote Sens.*, 3(4):560–564.

- Milillo, P., Giardina, G., Perissin, D., Milillo, G., Coletta, A., and Terranova, C. (2019). Pre-collapse space geodetic observations of critical infrastructure: The morandi bridge, genoa, italy. *Remote Sens.*, 11(12):1403.
- Miranda, N., Rosich, B., Meadows, P., Haria, K., Small, D., Schubert, A., Lavallo, M., Colard, F., Johnsen, H., Monti-Guarnieri, A., and D'Aria, D. (2013). The Envisat ASAR mission: A look back at 10 years of operation. In *Esa Living Planet Symposium*. ESA.
- Montazeri, S., Rodríguez González, F., and Zhu, X. X. (2018). Geocoding error correction for InSAR point clouds. *Remote Sens.*, 10(10).
- Montazeri, S., Zhu, X. X., Eineder, M., and Bamler, R. (2016). Three-dimensional deformation monitoring of urban infrastructure by tomographic SAR using multitrack TerraSAR-X data stacks. *IEEE Trans. Geosci. Remote Sens.*, 54(12):6868–6878.
- Montgomery, M. R. (2008). The urban transformation of the developing world. *Science*, 319(5864):761–764.
- Mora, O., Mallorqui, J. J., and Broquetas, A. (2003). Linear and nonlinear terrain deformation maps from a reduced set of interferometric SAR images. *IEEE Trans. Geosci. Remote Sens.*, 41(10):2243–2253.
- Mouélic, S. L., Raucoules, D., Carnec, C., King, C., and Adragna, F. (2002). A ground uplift in the city of Paris (France) revealed by satellite radar interferometry. *Geophys. Res. Lett.*, 29:1853.
- Olmsted, C. (1993). Alaska SAR facility scientific SAR user's guide. *Alaska SAR Facility Technical Report ASF-SD-003*.
- Open Geospatial Consortium (2012). OGC City Geography Markup Language (CityGML) Encoding Standard 2.0.0. Technical report.
- Parker, J. A., Kenyon, R. V., and Troxel, D. E. (1983). Comparison of Interpolating Methods for Image Resampling. *IEEE Trans. Med. Imag.*, 2(1):31–39.
- Pepe, A., Euillades, L. D., Manunta, M., and Lanari, R. (2011). New advances of the extended minimum cost flow phase unwrapping algorithm for SBAS-DInSAR analysis at full spatial resolution. *IEEE Trans. Geosci. Remote Sens.*, 49(10):4062–4079.
- Pepe, A., Yang, Y., Manzo, M., and Lanari, R. (2015). Improved emcf-sbas processing chain based on advanced techniques for the noise-filtering and selection of small baseline multi-look DInSAR interferograms. *IEEE Trans. Geosci. Remote Sens.*, 53(8):4394–4417.
- Perissin, D. (2006). *SAR super-resolution and characterization of urban targets*. PhD thesis, Politecnico di Milano, Italy.
- Perissin, D. (2008). Validation of the submetric accuracy of vertical positioning of pss in c-band. *IEEE Trans. Geosci. Remote Sens.*, 5(3):502–506.

- Perissin, D. and Wang, T. (2012). Repeat-pass SAR interferometry with partially coherent targets. *IEEE Trans. Geosci. Remote Sens.*, 50(1):271–280.
- Perissin, D., Wang, Z., and Lin, H. (2012). Shanghai subway tunnels and highways monitoring through cosmo-skymed persistent scatterers. *ISPRS J. Photogramm. Remote Sens.*, 73:58 – 67. Innovative Applications of SAR Interferometry from modern Satellite Sensors.
- Qin, X., Liao, M., Zhang, L., and Yang, M. (2017). Structural health and stability assessment of high-speed railways via thermal dilation mapping with time-series InSAR analysis. *IEEE J. Sel. Topics Appl. Earth Observ. Remote Sens.*, 10(6):2999–3010.
- Qin, X., Zhang, L., Yang, M., Luo, H., Liao, M., and Ding, X. (2018). Mapping surface deformation and thermal dilation of arch bridges by structure-driven multi-temporal DInSAR analysis. *Remote Sens. Environ.*, 216:71 – 90.
- Quegan, S. (1990). Interpolation And Sampling In SAR Images. *IEEE Trans. Geosci. Remote Sens.*, 28(4):641–646.
- Raney, R. K., Runge, H., Bamler, R., Cumming, I. G., and Wong, F. H. (1994). Precision SAR processing using chirp scaling. *IEEE Trans. Geosci. Remote Sens.*, 32(4):786–799.
- Rocca, F. (2004). Diameters of the orbital tubes in long-term interferometric SAR surveys. *IEEE Geosci. Remote Sens. Lett.*, 1:224 – 227.
- Samiei-Esfahany, S., Martins, J. E., van Leijen, F., and Hanssen, R. F. (2016). Phase estimation for distributed scatterers in InSAR stacks using integer least squares estimation. *IEEE Trans. Geosci. Remote Sens.*, 54(10):5671–5687.
- Sarabandi, K. and Chiu, T.-C. (1996). Optimum corner reflectors for calibration of imaging radars. *IEEE Trans. Antennas Propag.*, 44(10):1348–1361.
- Schmidt, D. A. and Bürgmann, R. (2003). Time-dependent land uplift and subsidence in the santa clara valley, california, from a large interferometric synthetic aperture radar data set. *J. Geophys. Res-sol. Ea.*, 108(B9).
- Schreier, G., editor (1993). *SAR Geocoding: data and systems*. Wichmann Verlag, Karlsruhe.
- Schubert, A., Jehle, M., Small, D., and Meier, E. (2010). Influence of atmospheric path delay on the absolute geolocation accuracy of TerraSAR-X high-resolution products. *IEEE Trans. Geosci. Remote Sens.*, 48(2):751–758.
- Schubert, A., Miranda, N., Geudtner, D., and Small, D. (2017). Sentinel-1A/B combined product geolocation accuracy. *Remote Sens.*, 9(6):607.
- Schubert, A., Small, D., Miranda, N., Geudtner, D., and Meier, E. (2015). Sentinel-1A product geolocation accuracy: Commissioning phase results. *Remote Sens.*, 7(7):9431–9449.

- Schunert, A. and Soergel, U. (2016). Assignment of persistent scatterers to buildings. *IEEE Trans. Geosci. Remote Sens.*, 54(6):3116–3127.
- Schwäbisch, M. (1995). *Die SAR-Interferometrie zur Erzeugung digitaler Geländemodelle*. PhD thesis, Stuttgart University.
- Shi, X., Zhang, L., Balz, T., and Liao, M. (2015). Landslide deformation monitoring using point-like target offset tracking with multi-mode high-resolution terrasar-x data. *ISPRS J. Photogramm. Remote Sens.*, 105:128 – 140.
- Shimada, M., Isoguchi, O., Tadono, T., and Isono, K. (2009). PALSAR radiometric and geometric calibration. *IEEE Trans. Geosci. Remote Sens.*, 47(12):3915–3932.
- Small, D., Rosich, B., Meier, E., and Nüesch, D. (2004). Geometric calibration and validation of ASAR imagery. In *CEOS WGCV SAR Calibration & Validation Workshop*, page 8, Ulm Germany.
- Small, D., Schubert, A., Rosich, B., and Meier, E. (2007). Geometric and radiometric correction of esa SAR products. In *ESA ENVISAT Symposium*, page 6, Montreux, Switzerland. Citeseer.
- Sousa, J. J. and Bastos, L. (2013). Multi-temporal SAR interferometry reveals acceleration of bridge sinking before collapse. *Nat. Hazards Earth Syst. Sci.*, 13(3):659–667.
- Stein, S. (1981). Algorithms for ambiguity function processing. *IEEE Trans. Acoust., Speech, Signal Process.*, 29(3):588–599.
- Svirko, D., Krsek, P., Stepanov, D., and Chetverikov, D. (2002). The trimmed iterative closest point algorithm. In *Pattern Recognition, International Conference on (ICPR)*, volume 03, page 30545.
- The Japan Times (2016). Huge street sinkhole disrupts services, forces evacuations near fukuoka's hakata station.
- The New York Times (2018). Genoa bridge collapse: The road to tragedy.
- Touzi, R., Lopes, A., Bruniquel, J., and Vachon, P. W. (1999). Coherence estimation for SAR imagery. *IEEE Trans. Geosci. Remote Sens.*, 1(37):135–149.
- Ulaby, F., Moore, R., and Fung, A. (1986). Microwave remote sensing: Active and passive, vol. iii, volume scattering and emission theory. *Advanced Systems and Applications*, Artech House, Inc., Dedham, Massachusetts.
- Usai, S. and Hanssen, R. F. (1997). Long time scale InSAR by means of high coherence features. In *Third ERS Symposium—Space at the Service of our Environment, Florence, Italy, 17–21 March 1997*, pages 225–228.
- Van der Zon, N. (2013). Kwaliteitsdocument AHN2. Technical report, Rijkswaterstaat & Waterschappen. In Dutch.

- van Leijen, F. (2014). *Persistent Scatterer Interferometry based on Geodetic Estimation Theory*. Netherlands Geodetic Commission, The Netherlands.
- van Leijen, F. and Hanssen, R. F. (2004). Interferometric radar meteorology: resolving the acquisition ambiguity. In *CEOS SAR Workshop, Ulm Germany, 27–28 May 2004*, page 6.
- van Natijne, A. L., Lindenbergh, R. C., and Hanssen, R. F. (2018). Massive linking of PS-InSAR deformations to a national airborne laser point cloud. *ISPRS - International Archives of the Photogrammetry, Remote Sensing and Spatial Information Sciences*, XLII-2:1137–1144.
- van Zyl, J. J. (1990). Calibration of polarimetric radar images using only image parameters and trihedral corner reflector responses. *IEEE Trans. Geosci. Remote Sens.*, 28(3):337–348.
- Wang, C., Li, Q., Zhu, J., Gao, W., Shan, X., Song, J., and Ding, X. (2017). Formation of the 2015 shenzhen landslide as observed by sar shape-from-shading. *Sci. Rep.*, 7(1):43351.
- Werner, C., Wegmüller, U., Strozzi, T., and Wiesmann, A. (2003). Interferometric point target analysis for deformation mapping. In *IEEE International Geoscience and Remote Sensing Symposium, 2003. IGARSS 2003.*, volume 7, pages 4362–4364 vol.7.
- Woodhouse, I. H. (2005). *Introduction to microwave remote sensing*. CRC press.
- Wright, T., Fielding, E., and Parsons, B. (2001). Triggered slip: observations of the 17 August 1999 Izmit (Turkey) earthquake using radar interferometry. *Geophys. Res. Lett.*, 28(6):1079–1082.
- Wu, C., Barkan, B., Huneycutt, B., Leans, C., and Pang, S. (1981). An introductory to the interim digital SAR processor and the characteristics of the associated Seasat SAR imagery. *JPL Publications, 81-26*, page 123.
- Xia, Y., Kaufmann, H., and Guo, X. (2002). Differential SAR interferometry using corner reflectors. In *IEEE International Geoscience and Remote Sensing Symposium, 2002. IGARSS 2002.*, pages 1243–1246 vol.2.
- Yang, M., Dheenathayalan, P., Chang, L., Wang, J., Lindenbergh, R., and Hanssen, R. F. (2016). High-precision 3D geolocation of persistent scatterers with one single-Epoch GCP and LIDAR DSM data. *European Space Agency, (Special Publication) ESA SP*, SP-740.
- Yang, M., Dheenathayalan, P., López-Dekker, P., van Leijen, F., Liao, M., and Hanssen, R. F. (2020). On the influence of sub-pixel position correction for PS localization accuracy and time series quality. *ISPRS J. Photogramm. Remote Sens.*, 165:98–107.
- Yang, M., López-Dekker, P., Dheenathayalan, P., Biljecki, F., Liao, M., and Hanssen, R. F. (2019a). Linking persistent scatterers to the built environment using ray tracing on urban models. *IEEE Trans. Geosci. Remote Sens.*, 57(8):5764–5776.

- Yang, M., López-Dekker, P., Dheenathayalan, P., Liao, M., and Hanssen, R. F. (2019b). On the value of corner reflectors and surface models in InSAR precise point positioning. *ISPRS J. Photogramm. Remote Sens.*, 158:113–122.
- Zebker, H. A. and Goldstein, R. M. (1986). Topographic mapping from interferometric synthetic aperture radar observations. *J. Geophys. Res-sol. Ea.*, 91(B5):4993–4999.
- Zebker, H. A., Rosen, P. A., and Hensley, S. (1997). Atmospheric effects in interferometric synthetic aperture radar surface deformation and topographic maps. *J. Geophys. Res. Sol. Ea.*, 102(B4):7547–7563.
- Zebker, H. A. and Villasenor, J. (1992). Decorrelation in interferometric radar echoes. *IEEE Trans. Geosci. Remote Sens.*, 30(5):950–959.
- Zhang, H. and López-Dekker, P. (2019). Persistent scatterer densification through the application of capon- and apes-based sar reprocessing algorithms. *IEEE Trans. Geosci. Remote Sens.*, pages 1–13.
- Zhang, L., Balz, T., and Liao, M. (2012). Satellite SAR geocoding with refined rpc model. *ISPRS J. Photogramm. Remote Sens.*, 69:37 – 49.
- Zhang, Q., Zhao, C., Ding, X., Chen, Y.-Q., Wang, L., Huang, G., Yang, C.-S., Ding, X.-G., and Jing, M. (2009). Research on recent characteristics of spatio-temporal evolution and mechanism of xi'an land subsidence and ground fissure by using gps and InSAR techniques. *Chinese J. Geophys.-Chinese Ed.*, 52:1214–1222.
- Zhu, X. X., Montazeri, S., Gisinger, C., Hanssen, R. F., and Bamler, R. (2016). Geodetic SAR tomography. *IEEE Trans. Geosci. Remote Sens.*, 54(1):18–35.
- Zhu, X. X. and Shahzad, M. (2014). Facade reconstruction using multiview spaceborne TomoSAR point clouds. *IEEE Trans. Geosci. Remote Sens.*, 52(6):3541–3552.
- Zink, M., Fiedler, H., Hajnsek, I., Krieger, G., Moreira, A., and Werner, M. (2006). The tandem-x mission concept. In *IEEE International Geoscience and Remote Sensing Symposium, 2006. IGARSS 2006*, pages 1938–1941.

Acknowledgement

I still remember my curiosity and excitement when I took my first SAR course in 2010. Now, nearly ten years later, I am finally finishing my PhD journey and I still love it. Reflecting on the whole journey, I would regard it as a valuable experience. It was a journey consisting of both pains and gains that shaped me and will guide my future life as well. Many people contributed to the accomplishment of this dissertation in various ways, for which I am sincerely grateful.

First and foremost, I could not be happier to have Mingsheng Liao, Ramon Hanssen, and Paco López-Dekker, as my supervisors. In 2012, I got the qualification of postgraduate recommendation and joined the radar group lead by Prof. Liao. The book he wrote is the first book that I read about InSAR, and I felt so honored to join his group. In the following years, his help, support, encouragement, and guidance were always there for both academic and personal problems. For these seven years, he guided my research, while simultaneously giving me a great degree of freedom, thus enabling me to explore topics of interest and to fulfill my scientific curiosity. Prof. Liao also introduced me to multiple projects which deepened my understanding of research and enhanced my ability. Participating in these projects has been an invaluable experience and facilitates my future work.

My deepest gratitude goes to Prof. Hanssen. I first met Prof. Hanssen in the summer of 2014 when he gave lectures at the GNSS center of Wuhan University. That was the year in which TUD and WHU signed the double degree program. He proposed this interesting and challenging topic, interpretation of InSAR scatterers, as one of the collaboration projects. I was working on InSAR applications for monitoring civil infrastructures at that time, and was very interested in this topic. The one-hour video interview and discussion with him encouraged me to pursue further education at TU Delft. For all these years, I thank him for making it all possible, for his constant and kind support, for critical comments, for inspiring suggestions, for the meticulous editing of scientific writing, for teaching me how to present scientific results, and for continuously training me to be an independent researcher. His preciseness and enthusiasm for scientific research have been inspiring me, and I see in him what I want to be. I still remember how he trained me to present scientific results at the ESA Living planet workshop, and how he helped and encouraged me for preparing my presentation in the Fringe symposium. Ramon, thank you very much, I have learned a lot from you, it was the best decision for me to pursue my PhD with you.

I would like to express my heartfelt gratitude to Dr. López-Dekker. We met in the summer of 2016, and then he became my co-promotor. His first presentation at the open seminar of our faculty was impressive. He was not only showing the technique but made this technique very interesting as well. He can always make his scientific research

into something interesting, which is something I want to learn. For me, he is the first person that I am able to discuss with whenever I have ideas, or when I need inspiration. Also, his critical comments helped me to focus on my ideas and his suggestions inspired me to advance in difficult moments. I appreciated every comment and suggestion from him. Paco, I will always remember the story you told me, that the beauty of SAR images only could be understood by trained eyes. Thank you for sharing the stories about your PhD work and encouraging me for confidence.

I experienced a marvelous amount of enjoyment in carrying out this research in the radar group at TU Delft. I am grateful to Freek van Leijen for our discussions and instant technical support. I am happy to cooperate with Prabu Dheenathayalan: our collaboration has led to three publications. Being part of the radar group and being involved in the daily huddle and the weekly group meeting has been delightful, and is something to be missed. Many thanks to Sami Samiei-Esfahany, Gert Mulder, Ramses Molijn, Lorenzo Lannini, Floris Heuff, Işıl Ece Özer, and Reenu Toodesh. I appreciate Hans van der Marel for sharing the geodetic data, Roderik Lindenbergh for his knowledge of laser point clouds, and Filip Biljecki for sharing the city models and the technique of modeling. Discussion with Xiaojun Luo, Jinliang Li, and Yuanhao Li was always instructive. Special thanks to Ling Chang, who is my colleague in TU Delft, and also my teacher, close friend, travel companion, and even a comrade. She gave me suggestions along with my research at TU Delft. I used several code boxes in this research, such as Doris, DePSI, RaySAR, and StaMPS. I thank everyone who has put the time and effort into developing and maintain these tools.

Thanks a million to all my colleges from the radar group at Wuhan. I am very grateful to Prof. Lu Zhang of the radar group at Wuhan University for his unselfish assistance, for puzzle solving, and for being a tutor on the proposal and report writing. The discussions with Timo Balz are always thought-provoking. I appreciate the help from my old colleagues of radar group at the beginning of my study at Wuhan University. These are Xuguo Shi, Lianhuan Wei, Houjun Jiang, and Yanan Jiang. I enjoyed the technical discussions with Xuguo and he is also turned into my close friend through thick and thin. I would like to mention some of them for the pleasant work on our projects. They are Lianhuan Wei, Yanan Jiang, Xiaoqiong Qin, Ziyun Wang, Ru Wang, Hao Feng, Nan Wang. I have learned a lot from working with them on our projects. Thanks to Ru Wang and Hua Gao for helping me prepare for the defense. Meng Ao is the best office roommate for his tidiness and summer 'mosquitoes feeding'. I have also had the pleasure of being associated with Xin Tian, Shanshan Li, Xie Hu, Jinyan Xu, Xinwei Yang, Jie Dong, Li Zhang, Yuting Dong, Heng Luo, Yanghai Yu, Jiayin Luo.

I was involved in a wonderful project at the Chinese University of Hong Kong for several months at the end of my PhD journey. I thank Prof. Bo Huang for giving me a chance for this project, and for him timely support and constructive discussions. It is nice to work with Guoqiang Shi, Yu Liu, jinrong Hu, biao Liu at CUHK.

My Chinese colleagues at the Geoscience & Remote Sensing department of TU Delft are acknowledged for brainstorming during lunchtime and cross-technology communi-

cations. They are also food sharers and traveling companions. They are Kaixuan Zhou, Yueqian Shen, Jiapeng Yin, Jiangjun Ran, Jinhua Wang, Junchao Shi, Xiaojun Luo, Han Dun, and Yuanhao Li. I would also like to thank my friends in Delft for making my stay there so enjoyable. They are Sixue Wu, Jun Nie, Chunyan Zhu, Zhilin Zhang, Dan Cheng, Jing Guo, Guolei Tang, Weiling Zhen, Youwei Wang, and Ding Ding.

My thanks and appreciation go to Prof. Zhiwei Li, Changcheng Wang, and Bin Xu at Central South University. They led me to the field of SAR. Prof. Li gave my first lectures on InSAR in the third year of my undergraduate. I still have those slides. He supervised my graduation project; it started my way to InSAR technology. I remember the first SAR-related code was an assignment of Dr Wang's course for data reading and orbit fitting of ALOS PALSAR data. I thank Dr. Xu for helping my first research project and for encouraging me to continue my further education at Wuhan University.

I would also like to express my deepest appreciation to my committee: Jordi J. Mal-lorquí, Christian Barbier, Peter Hooeboom, Roland Klees, Chao Wang, Liming Jiang, Bisheng Yang, Wen Yang, and Liangpei Zhang for their thorough reading of this work and their comments.

Heartfelt thanks to my friends who witnessed my growth these years, but I cannot list them all here. Ting Yu, thank you for sharing the joys and sorrows of life with me since we were born. You visited every university I studied, from Changsha to Wuhan, to Delft. There is one person who walked this journey with me, through all the hills and valleys. Menghua, thank you for the stimulating discussions, the continuous patience, and the company during every arduous moment.

This thesis is dedicated to my family. Their eternal love and support allowed me to have a life just as my Chinese name means, "Dream bravely and make life as a beautiful poem (Mengshi)."

Mengshi YANG
HK, Dec, 2019

About the Author



Mengshi Yang was born in Xishuangbanna, Yunnan, China, on 13 October 1990. She majored in Geomatics at the School of Geosciences and Info-Physics, Central South University, Changsha, between 2008 and 2012. She obtained a Bachelor's degree in engineering in 2012. In the same year, she was admitted as an MPhil-PhD student at the State Key Laboratory of Information Engineering in Surveying, Mapping and Remote Sensing, Wuhan University. The three years of study was mainly focused on the time series InSAR technique, supervised by Prof. Mingsheng Liao. In September 2015, she started to work as a PhD candidate in the department of Geoscience and Remote Sensing at Delft University of Technology.

This is a double degree program of the joint research center between Delft University of Technology and Wuhan University. She focused on the interpretation of time-series of coherent scatterers, supervised by Prof. Ramon Hanssen and Dr. Paco López-Dekker.

ISBN 978-94-6384-128-3

